NUCLEAR ENGINEERING RESEARCH INITIATIVE (NERI) PROGRAM
FINAL TECHNICAL REPORT

DE-FG03-00SF22167
NERI PROPOSAL 2000-069

AN IN-CORE POWER DEPOSITION AND FUEL THERMAL ENVIRONMENTAL MONITOR FOR LONG-LIVED REACTOR CORES

Final Report

Principal Investigator: Don W. Miller, Professor, Nuclear Engineering
The Ohio State University

September 2004

Report Contributors:

Eric R. Kreidler
Professor of Materials Science
The Ohio State University

Andrew C. Kauffman
Research Associate
The Ohio State University

Hanying Liu
Postdoctoral Researcher
The Ohio State University

Daniel J. Mills
Graduate Research Associate
The Ohio State University

Garrett P. Wonders
Graduate Research Associate
The Ohio State University

Keith W. Maupin
Graduate Research Associate
The Ohio State University

Dongxu Li
Graduate Research Associate
The Ohio State University

Joseph W. Talnagi
Senior Research Associate
The Ohio State University

Mario Carelli
Chief Scientist
Westinghouse Electric Co.

Vefa Kucukboyaci
Senior Engineer
Westinghouse Electric Co.

Bojan Petrović
Senior Scientist
Westinghouse Electric Co.

H. Frank Ruddy
Consulting Scientist
Westinghouse Electric Co.

Table of Contents

List Of Figures

List Of Figures (continued)

List Of Figures (continued)

List Of Figures (continued)

List Of Tables

1.1 REVIEW OF PROGRAM OBJECTIVE

The primary objective of this program is to develop the Constant Temperature Power Sensor (CTPS) as in-core instrumentation that will provide a detailed map of local nuclear power deposition and coolant thermal-hydraulic conditions during the entire life of the core. In the case of the some DOE Generation IV reactor cores, this could include normal operation, post-accident operation and monitoring after the core is placed in permanent storage. The sensors used in this instrumentation must have a lifetime comparable to the core and be compatible with the neutronic and thermal conditions expected over the range of proposed Generation IV reactor designs. Further, the sensors must be robust and capable of operation even with extensive material degradation and, if required to achieve this objective, they must provide for *in situ* calibration and performance monitoring.

The Constant Temperature Power Sensor (CTPS) concept is based on the idea of maintaining the temperature of a small mass of actual reactor fuel or fuel analogue constant by adding heat through resistive dissipation of input electrical energy. A feedback control loop is used to provide the exact amount of input electrical energy needed to keep the fuel mass at a specified constant temperature, well above the coolant bulk temperature, regardless of the nuclear energy deposited in the mass. Energy addition to the fuel mass and fuel temperature feedback to the controller are both provided by a simple resistive heating element embedded in the fuel mass. The input electrical energy required to maintain a constant temperature provides a measure the actual nuclear energy deposition since they are inversely related.

1.2 REPORT ORGANIZATION

This document is the final report for the DOE-NERI project DE-FG03-00SF22167. The report is comprised of three sections; a summary of the major tasks, which includes an estimate of the completion percent, completion date and a cost

estimate by task, a description of the work completed, and a report of the experimental results described and thoroughly documented.

During the “no cost extension” time period we were finally able to fabricate a significant number of sensors, which include the original cylindrical design and the planar configuration with plated electrodes. We thought we could finally see the “light at the end the tunnel” on a difficult research program. Unfortunately, additional challenges arose, First, Professor Eric Kreidler, who was responsible for sensor fabrication, had a serious accident while skiing, which disabled him for most of six months. Fortunately the graduate student who had assisted Professor Kreidler was able to complete fabrication of several sensors and begin testing. Early in the testing process there was an unfortunate occurrence, which resulted in a sensor being lost in the high temperature test facility. This required suspension of testing for a month while the facility was dismantled and cleaned of sensor debris.

Following cleanup of the test facility the test program was resumed and unanticipated problems were encountered with the software based PID control system. This system had been thoroughly tested using sensor simulation comprised of different resistors. Those tests gave no indication of the problems encountered with real sensors, which included instability and excessive noise. Initially we thought the problems might be traced to the LABVIEW platform on which the PID control was based.

Following extensive troubleshooting we were unable to identify the root cause of the problems. Consequently we concluded that we would have to try the hardware proportional controller used with the first prototype CTPS. This proved to be more successful, although noise continued to be a problem.

To test the CTPS sensors, they were placed in the high temperature neutron flux oscillator facility at the Ohio State University reactor lab. This facility allowed the determination of sensor linearity and sensitivity as well as a deterministic measure of sensor bandwidth. Results proved that the sensors are linear and exhibit sensitivity

comparable to that predicted by the numerical model and superior to current technology, which uses fission chambers. Results also show the sensors have bandwidths of 4 Hz for the planar sensor and 6Hz for the cylindrical sensor, which compare favorably with the numerical modeling and may be sufficient to meet requirements for safety-related measurements. The problems previously mentioned with the software based PID control prevented the testing of the dynamic calibration capabilities of the sensor system. Thermal drift correction for which the dynamic calibration capabilities were designed was demonstrated as necessary for this detector system. Many rounds of testing gave consistent results that demonstrate the sensors operate as expected and that their static and dynamic responses are consistent with the numerical models.

2. DISCUSSION OF PROGRAM PROGRESS

2.1 EVALUATION OF THE EFFECTS OF THE CTPS ON THE REACTOR ENVIRONMENT

Work has been completed on this task. A detailed report on the results of this task is contained in Appendix A. It is an extensive study and best presented in a closed, complete form as an Appendix to the overall report. The sensor dimensions, bulk materials, and quantities and isotopic mixtures of fissionable materials were used with the current IRIS core configuration information to evaluate the perturbations on the neutron and temperature environment resulting from the presence of CTPS units.

Monte Carlo calculations were performed to identify effects of in-core power monitors (sensors) on the core neutronic environment. As a representative Generation IV reactor environment, we modeled an IRIS fuel assembly and placed the sensors in the instrumentation thimble for perturbation studies. Numerical test cases included cylindrical and planar sensor designs containing high- (97%) and low- (4.5%) enriched U and with small and large axial sizes (cylindrical design only). For these different cases, the assembly multiplication factor, pin power distributions and thermal and fast fluxes were computed. It was observed that the presence of the sensors did not perturb the assembly multiplication factor and the impact on the power and flux levels was mainly local. However, in the case of the highly enriched uranium sensor design, the power density increase in the sensors was considerable, *i.e.* more than an order of magnitude larger than in the fuel pins. This high power density will affect the performance of the sensors, as they will burn faster than the fuel pins and will require frequent replacements. Therefore, a study of the sensor depletion may be warranted. Moreover, with such a high power density, the thermal performance and integrity of the sensors may become an issue. In summary, the effect of the sensors on the core neutronic environment is acceptable, but the performance of the sensors themselves needs to be further evaluated.

2.2 COMPLETION OF THE HIGH-TEMPERATURE TEST FACILITY

We have completed and tested the high-temperature test facility for testing prototype sensor elements in The Ohio State University Research Reactor (OSURR) facility. This represents completion of an important program milestone and places us in a position to test CTPS sensor prototypes when they have been successfully fabricated.

The test facility will be used to evaluate the static and dynamic performance of prototype sensors in environmental and neutronic conditions similar to those expected in a high-temperature gas reactor. This facility was nominally designed to heat sensors up to 800 °C at a flow velocity of 5.8×10^{-3} m^3/s (350 L/min) in a closed cooling loop. A previous study showed that neutron noise analysis methods were unable to resolve the frequency response of the test sensors (1). Consequently, a local neutron flux oscillator, or modulator, has been included in the facility to provide a local sinusoidal flux variation over a frequency range of one to 100 Hz.

The facility features the following capabilities:

- heat test sensors to as high as 800º C for extended periods of time
- maintain a gas flow rate variable from 0 to greater than 5.8×10^{-3} m^3/s (350 L/min) in a closed cooling flow loop to simulate a range of convective conditions
- provide the maximum neutron flux level available from the OSURR
- sinusoidally modulate by a few percent the neutron flux at the sensor location over a frequency range of one to 100 Hz with negligible effect on reactor power and reactivity
- independently monitor the neutron flux, the gamma flux, and the temperature at selected locations
- minimize component activation and shield users from radiation

The Large Volume External Cavity (LVEC) dry-tube was chosen to house this test facility. It is a cylindrical 6061-T6 aluminum dry tube with a 0.241 m (9.5 inch)

inner diameter and 0.0127 m (0.5 inch) thick wall that is secured with a bracket next to the reactor when being used. The LVEC facility was selected because it has sufficient space to house both the neutron-flux oscillator and the high-temperature facility and is located in a high neutron flux. The tube is counterweighted with iron plates to provide near-neutral (slightly negative) buoyancy. The plates fill the bottom 0.914 m (three feet) of the tube, which makes the usable length of the tube about 5.2 m (17 feet) and positions the bottom of the usable space at the bottom of the core. To maximize the flux seen from the reactor core, an aluminum box that can be evacuated of water with air is positioned on the front of the LVEC at the midline height of the core. A gold wire flux analysis was performed at 1% reactor power to characterize the neutron flux in the LVEC, and this analysis estimated a full-reactor-power neutron flux at the test sensor position of 4.5×10^{11} nv with the box filled with air and a flux of 2.1×10^{11} nv with a water-filled box.

The design of the assembly was subject to a number of constraints. The high-temperature facility and flux oscillator were positioned near the bottom of the tube so that they are aligned with the peak flux at the center of the reactor core. This required that the support structure for the flow-loop pipes, wire conduit, high-temperature facility, neutron flux oscillator, and oscillator drive mechanism be an integral part of the design. This support structure was broken into sections to accommodate the limited space between the surface of the reactor pool and the ceiling. The drive mechanism for the oscillator was constrained from translational movement, and excessive shaking and loosening of components from vibrations emanating from the neutron flux oscillator and shaft was prevented.

The facility is designed to minimize activation of construction materials. To minimize personnel exposure to radiation, the parts of the facility that will become activated are designed so that they can be quickly removed if they need to be replaced. In addition, the facility is designed so that sensors can be introduced into and removed from the coolant loop without removing the entire assembly from the LVEC. Since many components of the facility have a lower melting point than the maximum temperature at

the sensor-testing position, high temperatures are confined to a small volume within the high-temperature facility.

Aluminum proved to be the best material for the facility for its combined advantages of low cost, low activation, good strength and machinability. The support structure is an aluminum skeleton, which has three 1.83 m (six feet) sections consisting of aluminum plates attached to threaded aluminum rod. The locking nuts holding the plates to the threaded rods have aluminum wire run through them and the rods to ensure that they cannot "back away" from the plates resulting from vibration. Components of the test facility are attached to this support structure. The bottom section houses the oscillator and the high-temperature facility. The middle section holds flow-loop pipes and wire conduit, and the top section holds pipes, conduit, neutron and gamma shielding, a helical copper cooling coil, and the oscillator motor. The support structure attaches to the top of the LVEC tube to secure all components in a fixed position. Sections are attached together with couplings on the threaded rods that are locked in place with nuts as they are lowered into the LVEC facility. Both wire conduit and flow-loop pipes are Schedule-40 aluminum pipes with threaded ends. Threaded couplings with locking nuts are used to connect the pipe sections.

A GE Reuter-Stokes NA-300 Local Power Range Monitor (LPRM) fission chamber is used to monitor the neutron flux in the region of the test sensors. This detector has been designed for DC measurement, but from previous experience at the OSURR, we expect a bandwidth of approximately10 Hz. It has been calibrated with the OSURR, and with a sensitive electrometer, such as the Keithley 617 used for our measurements, it offers 4-5 decades of response. A Photonics CRGE 10 xenon-filled, high-pressure ionization chamber is used to monitor the gamma flux. It has been calibrated with a Cobalt 60 source and is capable of giving a broad range of response with little sensitivity to neutrons. The fission chamber is positioned in a plane parallel to the edge of the reactor at the same distance as the prototype sensors, and the gamma chamber is positioned directly behind it. They are positioned as close as possible to the prototype sensors without being in the high-temperature region. This allows them to

monitor flux levels similar to those experienced by the CTPS without being unnecessarily exposed to high temperatures. Type-K thermocouples, which are suitable for radiation environments, monitor temperatures at a number of locations within and outside the high-temperature loop. Two Crossbow Technology CXL100HF3 tri-axial accelerometers installed in the LVEC measures vibration of the test facility induced by the oscillator. These sensors have an input range of $\pm$ 100 g and a frequency range of 0.3-10,000 Hz. The first is located in the bottom section, just above the oscillator. A second accelerometer is located at the top of the middle section in the event of the lower accelerometer being damaged by radiation exposure. It is over 2.75 m (nine feet) above the top of the core, so it is exposed to less radiation.

Radiation shielding for the test facility consists of two cylindrical plugs in the top section of the assembly with through holes for pipes. The first is a 0.305 m (1 foot) long section of polyethylene and the second is a 0.305 m long section of 80% lead, 1% boron, and 19% polyethylene. The shielding reduces neutron and gamma radiation streaming from the LVEC tube. At 1% operating power, the shielding reduces the gamma exposure rate at the reactor-pool wall near the LVEC by a factor of 8, and the neutron dose rate by a factor of 20. The LVEC and assembly are shown in Figure 1.

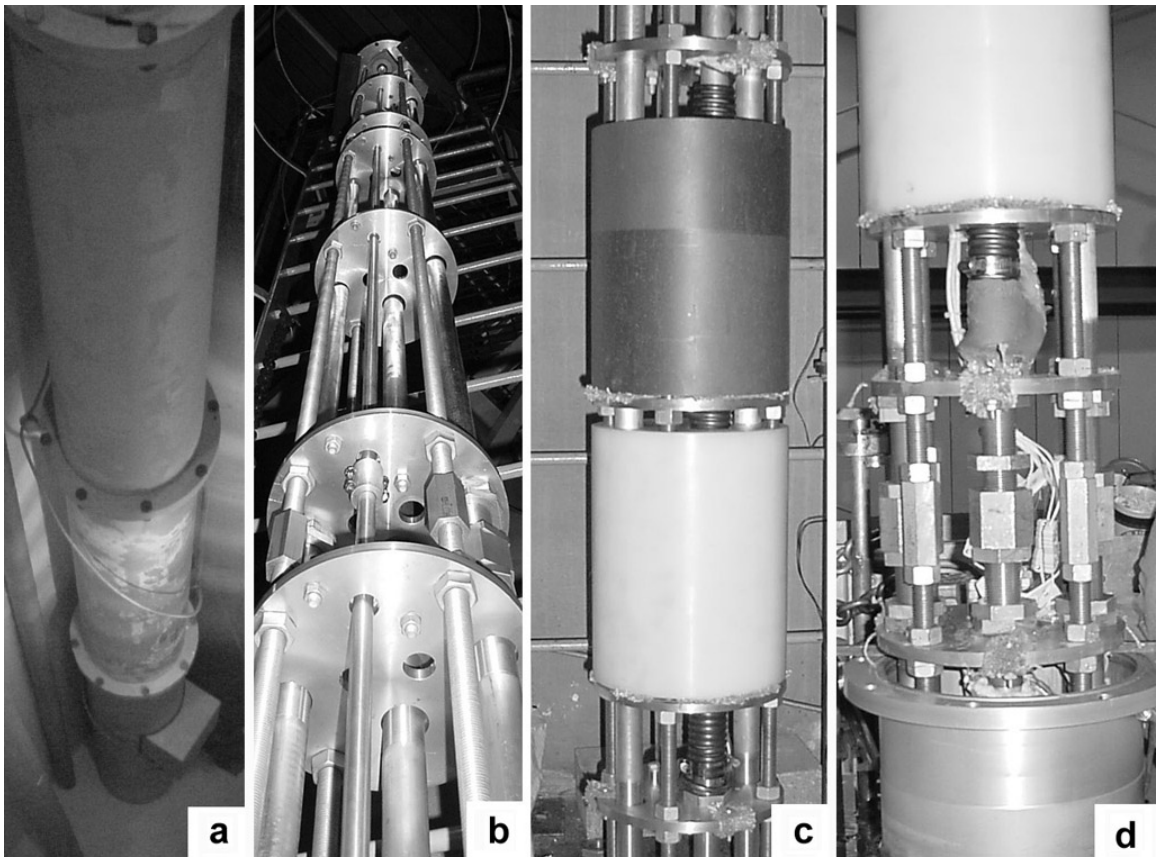

Figure 1: LVEC Tube (a) and experiment assemblies (b-d)

A 3 KW alumina and nichrome commercial heat gun element was chosen to heat the airflow based on its small size and ability to heat air to temperatures up to 800 ºC. A quartz tube houses the heating element, and both sit atop a machined graphite base, chosen for its good thermal characteristics and low activation. The quartz tube holds the heater in place, and the quartz tube is held in position by a coupling above it. Kaowool, a ceramic fiber blanket made primarily of alumina and silica, insulates the heater assembly, and a thin aluminum cylindrical shell encloses the furnace assembly. Immediately below the graphite, an aluminum elbow holds a perforated plate, designed to flatten the velocity profile of the air as it passes through the two square elbows. This ensures an even flow distribution across the entrance of the heating element, preventing premature burnout. A pressure feed-through that carries the lead wires for the heater is mounted to the back of the elbow. The lead wires are connected to a 0-240 VAC voltage supply that powers the

heater element. A tapered neck at the top of the quartz fits into a tapered aluminum slip coupling. This slip coupling consists of two pieces. The top piece can move up or down as the aluminum pipe above expands or contracts with heating or cooling, and the bottom piece of the slip coupling is secured to the outer aluminum cylinder to prevent it from moving and breaking the quartz tube. The coupling contains high-temperature fabric inside and outside that seals the flow loop but allows for pipe expansion. The furnace facility is suspended a small distance above the bottom plate of the assembly to allow for expansion of the facility below the slip coupling. It is secure when in place but can be removed quickly to minimize personnel exposure during maintenance. The complete furnace assembly can be seen in Figure 2.

Slip couplings similar to that above the furnace have also been installed in the middle and upper sections of the flow-loop hot leg to allow for thermal expansion. Reduction in the overall heatup rate of the facility is effected by using fiber blanket insulation wrapped around the hot leg of the flow loop in the lower two sections of the facility. A helical copper cooling coil surrounds a 0.76 m (2.5 feet) length of the hot leg where it penetrates the shielding in the top section (see Fig. 1c). Deionized water is pumped through this coil to remove heat from the furnace flow loop and prevent the shielding from being exposed to high temperatures. In addition, ceramic inserts were put between the hot leg locking nuts and the structure plates and between the oscillator-shaft bearing blocks and structure plates. These ceramic inserts reduce the rate at which the dry tube heats up as well as prevent conduction of heat to the oscillator shaft, which would increase the rate of degradation of the lubricant in the bearings.

The flow loop feed and return pipes connect to a blower outside of the test facility. This blower is capable of moving about 8.0×10^{-3} m^3/s (480 L/min) of air through the flow loop at STP conditions (20 °C and 1×10^5 Pa). A valved bypass controls the flow rate, allowing a range of Reynolds numbers up to 2.7×10^4 at STP conditions. The maximum temperature of 800 ºC can be reached by running the blower at 5.8×10^{-3} m^3/s (350 L/min) with the heater at its maximum voltage. A lower flow rate would allow higher temperatures, but according to the manufacturer would severely degrade the

lifespan of the element. To measure the flow rate, a flow element is located between the blower outlet and LVEC facility after a straight pipe section long enough to develop flow. Type-K thermocouples are positioned in the flow loop during furnace operation to measure temperature.

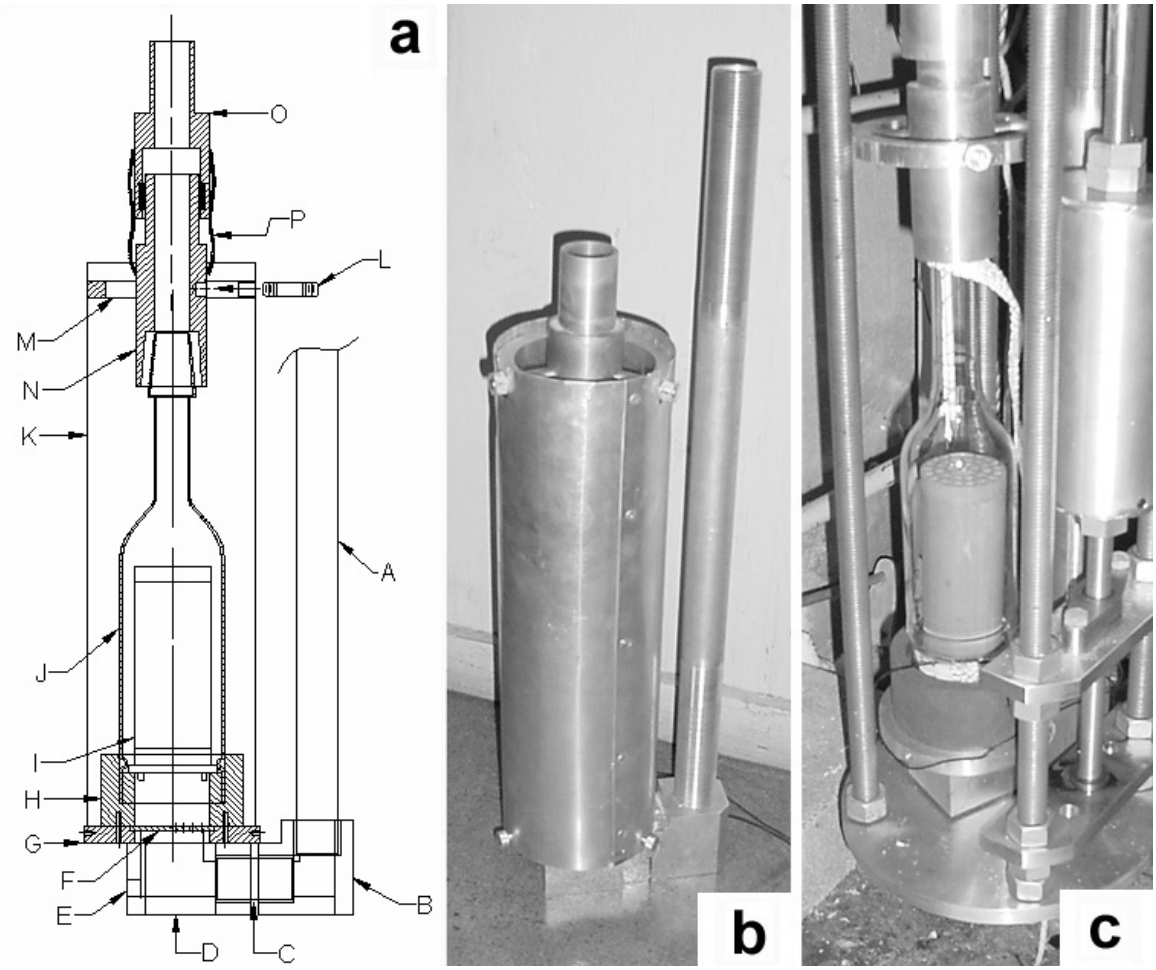

Figure 2: Furnace Assembly

The neutron flux oscillator is comprised of a cylindrical body of moderator that has an absorber on one side and spins along its axis, connected by a shaft to a motor. Graphite is used as the moderator since it retains physical integrity at high neutron fluence, and cadmium was chosen as the absorber since it can be easily shaped. Because

of the required rotational speed and wide speed range, a DC motor was selected over other motor types, and a straight 0.016 m (5/8 inch) diameter aluminum shaft consisting of three sections (one for each assembly section) coupled together was chosen over designs using gears. Due to internal bearings that would degrade in a radiation environment, the motor is mounted at the top of the facility. The oscillator is encased in a sturdy aluminum enclosure to prevent it from coming apart at high speeds. This enclosure is welded to aluminum rods running through the graphite to prevent the graphite from rotating within the enclosure. Aluminum was machined out of the ends of the oscillator to counterbalance the cadmium sheet on one side. Aluminum end caps were welded to the casing to provide strength and to reduce air drag that would be caused by the machined ends.

The oscillator is positioned on the far side of the sensors from the reactor to maximize the flux at the sensor location and to minimize the reactivity effect of the oscillator on the reactor. A thrust bearing supports the weight of the oscillator, and ten more bearings are spaced along the length of the assembly to prevent the shaft from whipping or bowing. An appropriate combination of sealed and needle-roller bearings was determined experimentally to strike a balance between stability and required motor power. The sealed bearings are attached firmly to the oscillator shaft with setscrew collars and have high stability but significant drag. The needle-roller bearings allow slight movement of the shaft, but they cause very little drag for the motor to overcome. An optical encoder is used to a measure the oscillator speed by reflecting light from a rotating black and white disk, which provides one square wave cycle per shaft rotation to the data acquisition system.

Before the oscillator was constructed, an analytical and experimental assessment of the design was completed to evaluate whether it would meet the performance requirements. Monte Carlo N-Particle Transport Code (MCNP) was used to model the use of both polyethylene and graphite as the body of the oscillator. A model of the LVEC tube with the oscillator was added to a detailed model of the OSURR, which had been created previously for other research. The LVEC was modeled as an empty tube with the

cylindrical oscillator near where it is currently positioned. Because aluminum has small neutron absorption and scattering cross sections, the assembly structure did not need to be modeled. A tally cell was defined at the sensor position to estimate the neutron flux to which a sensor would be exposed, and another tally cell was defined at a location in one of the existing facilities with a known neutron flux to scale estimates of neutron flux at the sensor position. Flux depression from a test sensor at the sensor position was not included in the model, as this would affect the overall neutron flux measured but not the size of neutron flux oscillations. Simulations were run for the cadmium facing towards and away from the sensor position. The oscillator model with a polyethylene core gave a flux oscillation estimate of 8%, and the oscillator model with a graphite core gave a flux oscillation estimate of 6%. These oscillation estimates were within the calculated uncertainty of each other, but the estimates were enough larger than uncertainty values to show that an oscillation effect existed for this oscillator geometry.

In addition, a mock-up of the oscillator was tested at low reactor power in the LVEC. A Teflon cylinder (similar to polyethylene) with cadmium on one side was suspended at the oscillator position in the LVEC, and a fission chamber was suspended at the test-sensor position. The fission chamber response was recorded with the cadmium facing towards and away from it. A flux difference of approximately 5% was measured, and no reactor control rod movement was necessary to compensate for the change in orientation of the oscillator. This indicated a negligible impact on core reactivity, and the agreement between the computer models and mock-up test indicated that the proposed design would give an oscillation of 5% to 10%. Figure 3 below shows the oscillator assembly and its components.

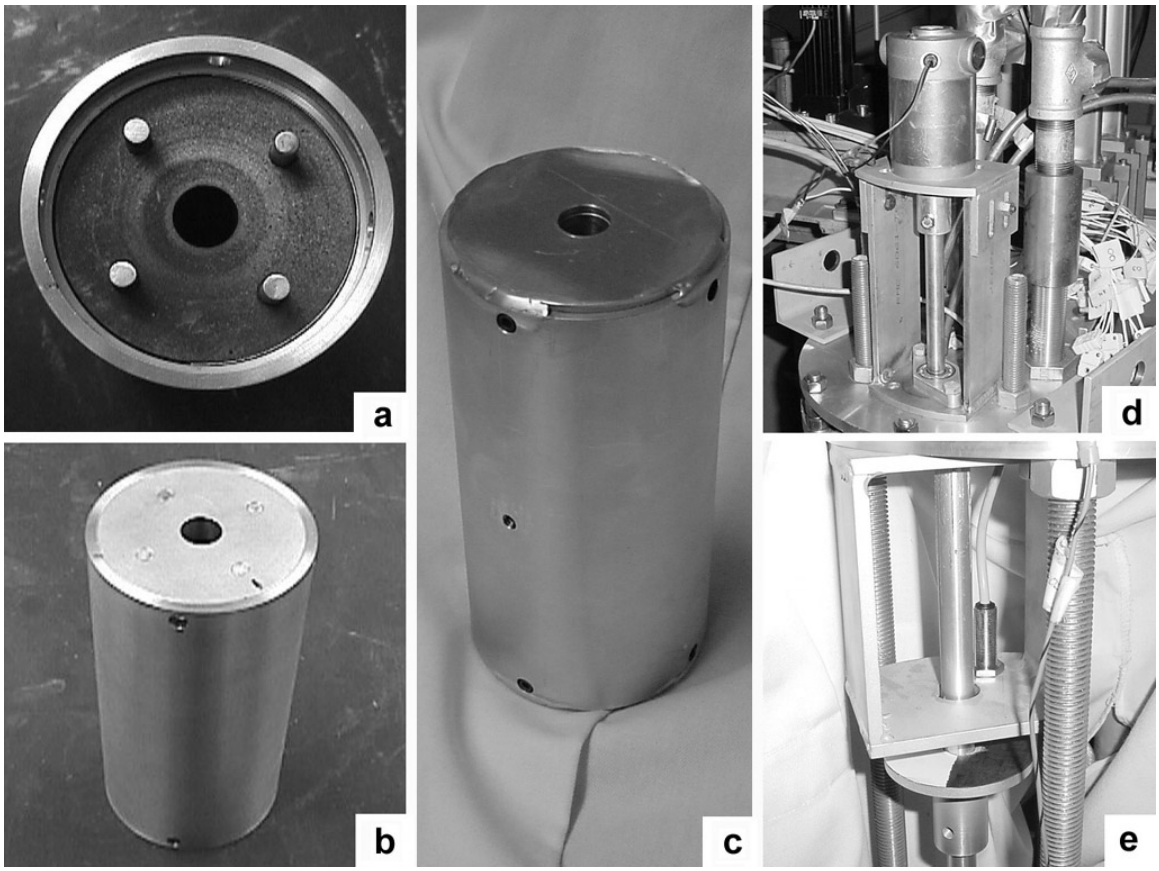

Figure 3: Flux Oscillator Components

Following the completion of a detailed safety analysis, testing of the assembly was performed in three stages: in the ladder cage of the reactor bay where it was constructed, in the LVEC tube following installation, and in the LVEC tube next to the reactor.

Testing was first performed in the ladder cage, where the assembly was constructed and modified, to assure the oscillator and oven operate correctly and safely. Because the assembly is out of sight once it is in the LVEC tube, this testing was critical in that it allowed us to visually verify safe operation. To test in the ladder cage, the assembly was bracketed to the ladder at seven vertical positions, which was deemed a reasonable approximation of how the assembly would be constrained in the LVEC tube. The oscillator was tested across the frequency range of zero to 79 Hz in steps of 5 Hz. The DC motor used for this testing was underpowered for the desired 100 Hz range, and a replacement DC motor will be identified in the future to achieve this range.

Accelerations were measured along the x, y, and z-axes with both lower and upper accelerometers. Between zero and 50 Hz, the oscillator ran quietly, and accelerations were small. The RMS accelerations measured in all directions by both accelerometers were 3 g's or less. However, as evidenced by audible noise, RMS acceleration measurements, and acceleration power spectral density (PSD) plots, the assembly coupled to the ladder cage had an excitation frequency at 60 Hz. Above 70 Hz, the accelerations decreased to RMS levels below 5 g's. Figure 4 shows plots of acceleration as a function of oscillator frequency. Figure 5 shows PSD plots of the voltage output of the lower accelerometer X-axis with the oscillator off and with the oscillator running at 30 Hz. In the lower graph, an excitation at 60 Hz can clearly be seen, and the upper graph shows that this 60 Hz peak is not the result of electrical noise.

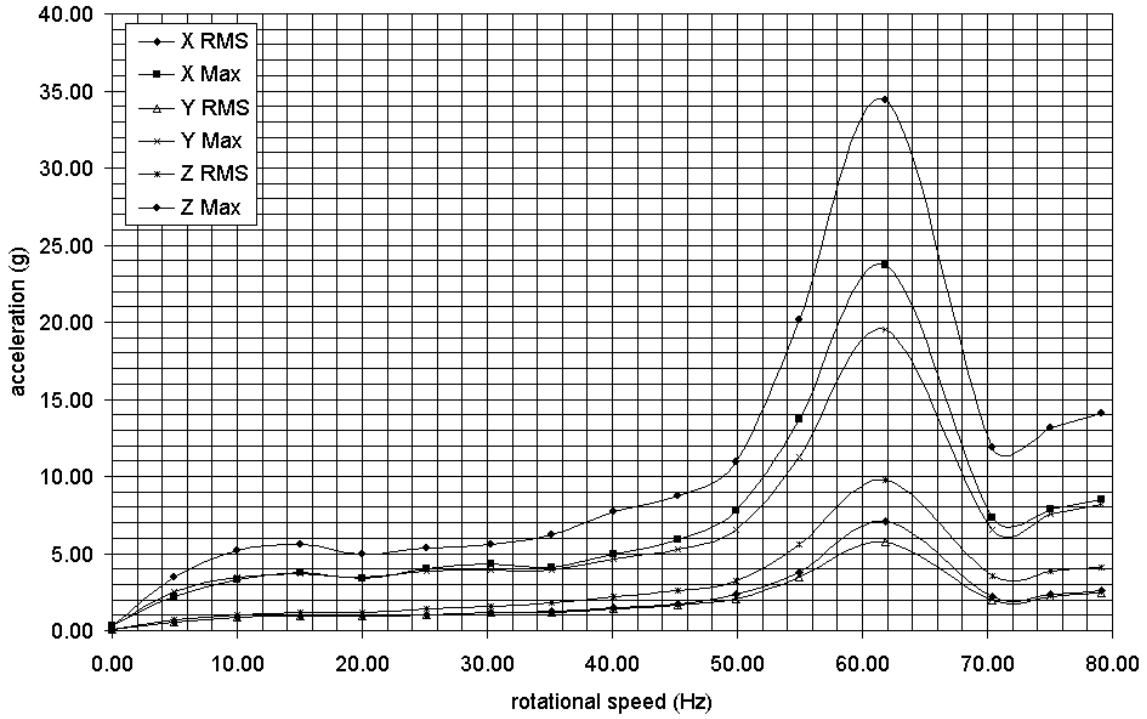

Figure 4: Measured Accelerations From The Oscillator

To test the furnace facility, the temperature at the test sensor position was raised in steps to its maximum temperature of 800 ºC, and then the LVEC facility was allowed to come into thermal equilibrium, as seen in Figure 6. Temperature measurements were taken to verify that no part of the assembly, including the aluminum expansion coupling right above the furnace, got too hot. Finally, with the furnace facility at thermal

equilibrium at its maximum temperature, the oscillator was run at 50 Hz. Since the hot leg is expanded to its maximum in this state, this is the worst-case scenario for the oscillator to cause the hot leg and high-temperature facility to vibrate. Visual observation verified that the hot leg and high-temperature facility were not vibrating, which was consistent with the measured accelerations that were unchanged from those taken when the furnace was not running.

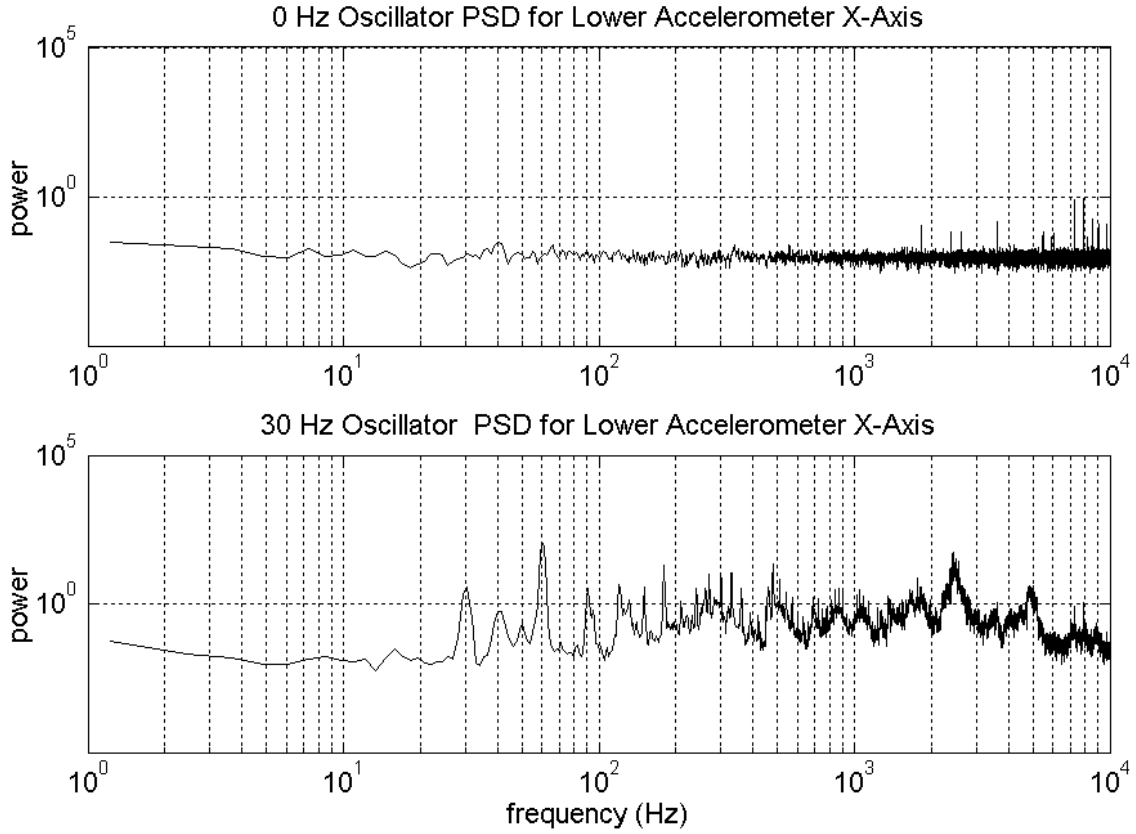

Figure 5: PSD Plots of Accelerations From the Oscillator

Following installation in the LVEC, tests were run to verify safe operation of the assembly. The oscillator was tested from a frequency range of zero to 50 Hz in steps of 5 Hz. Above 50 Hz, the fuse in the motor controller was blown. Most likely, the assembly was not perfectly straight over its entire length when it was secured in the ladder cage, but the oscillator rod was very straight within the assembly. When the assembly was

loaded into the LVEC, which forced it to be straight, the oscillator shaft was forced into a slight misalignment. However, the shaft moves freely when turned by hand, indicating that it is aligned reasonably well. Below 50 Hz, the RMS accelerations measured in all directions by both accelerometers were 3 g's or less, comparable to when the assembly was in the ladder cage. At 50 Hz, the RMS accelerations began to rise, just as they did at 55 Hz when the facility was secured to the ladder cage. However, all RMS values were still 5 g's or less. This rise may indicate that the resonant frequency has been shifted down to 55 Hz from 60 Hz, but that cannot be confirmed until a more powerful DC motor is installed so that we can test at higher speeds. The furnace was tested at 800 ºC, and all ambient and component temperatures were acceptable. With the furnace facility at thermal equilibrium at 800 ºC, the oscillator was run at 50 Hz. The furnace and oscillator exhibited no apparent interactive effects.

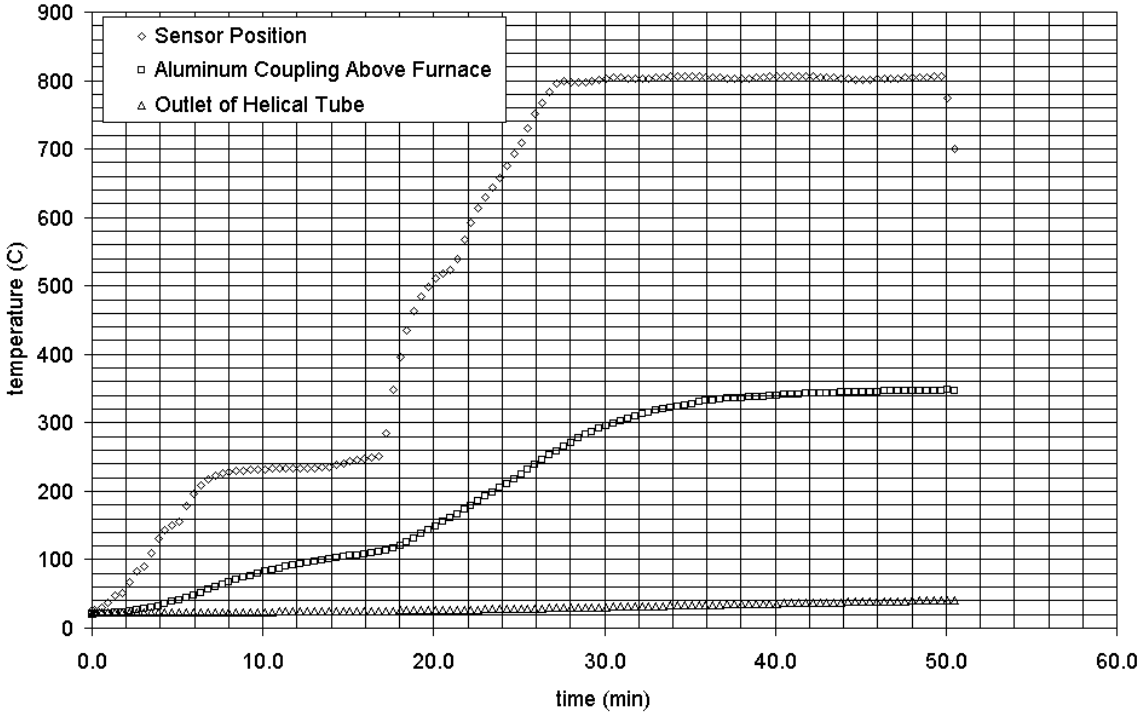

Figure 6: Temperature Profiles and Heatup Rate of the Test Facility

To test the oscillator in the neutron flux field and to measure the neutron flux in the hot leg and compare it to the flux measured by the mounted fission chamber, a fission chamber was placed in the test-sensor position. Since the fission chamber is not intended for operation in the high temperature airflow, the furnace was turned off for all such

testing. Most measurements were made with the box on the front of the LVEC filled with air; however, measurements were taken at 5 kW with a water-filled box to determine the difference in neutron flux.

As shown in Table 1, the fission chamber permanently mounted in the LVEC facility and the fission chamber placed in the flow-loop hot leg measured neutron flux magnitudes within two percent of each other, which will allow accurate verification of readings from test sensors. The flux measured at full power with an air-filled box was 36% lower than that estimated by the gold-wire analysis because the fission chamber depresses the measured neutron flux. Flooding the box with water instead of air reduces the flux measured by the fission chambers by a factor of about 3.7. This differs from the ratio of 2.1 estimated by gold-wire analysis because of the difference in the energy-dependent absorption cross-sections between gold and uranium. Compared to the reactor power measured by the control-room instrumentation, the flux in the LVEC is not linear with reactor power; however, this nonlinearity is less than 5% across the reactor power range of 1% to 100%.

The time-dependent shape of the flux oscillation seen at the test sensor position follows the shape of a sine wave reasonably well, as shown in Figure 7. The small differences from a true sine wave result from the geometry of the tube and its influence on the scattering of neutrons towards or away from the fission chamber.

Reactor Power (kW)	LVEC Box Filled with	Mounted Fission Chamber (nv)	Hot-Leg Fission Chamber (nv)	Percent Difference in Reading
5	water	7.94×10^{8}	8.06×10^{8}	1.5%
5	air	2.98×10^{9}	2.98×10^{9}	< 1%
50	air	2.92×10^{10}	2.90×10^{10}	< 1%
500	air	2.86×10^{11}	2.87×10^{11}	< 1%

Table 1: Neutron Flux Measurements in the LVEC Facility

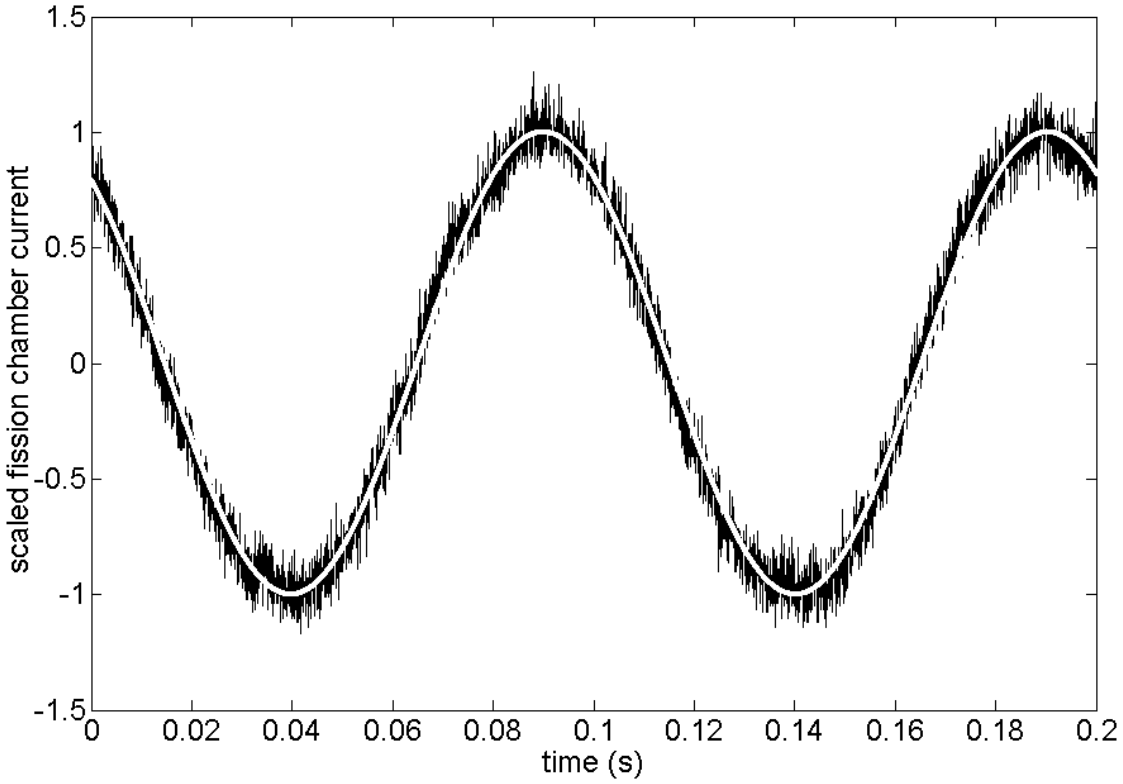

Figure 7: Measured Flux Variation Induced By The Oscillator

At low frequencies of oscillator rotation ($\leq$ 10 Hz), the fission chamber in the hot leg measured a 6.6% peak-to peak amplitude change at full reactor power, which is within the 5% to 10% estimate from the preliminary analysis. Between 10 and 20 Hz, the percentage amplitude oscillation begins to decrease with frequency. This rolloff is caused by the measurement system, not the oscillator. More specifically, the mineral-insulated cable that transmits the current from the fission chamber to the electrometer acts as a low-pass filter. To demonstrate determination of sensor parameters using the oscillator, the fission chamber's 1st-order dynamic parameters were estimated using the oscillator, as shown in Figure 8.

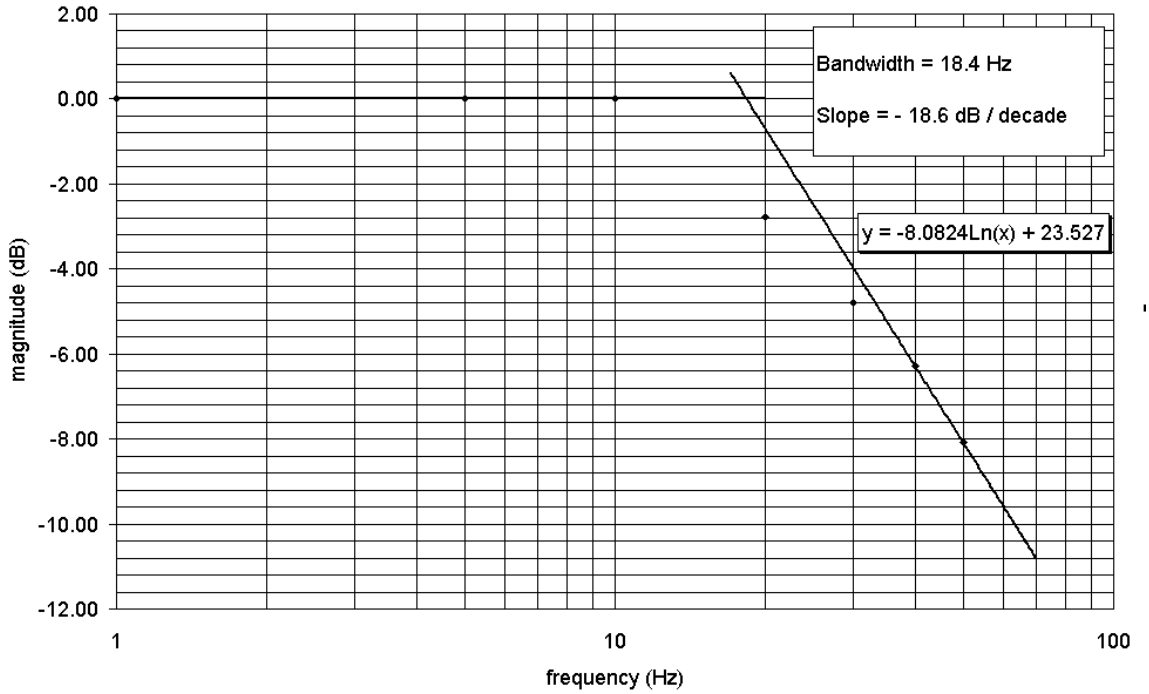

Figure 8: Fission Chamber Frequency Response

Table 2 shows a summary of the important results and data for the test facility. The furnace facility and oscillator are both working properly, but currently the oscillator does not have the full operational frequency range. When an appropriate replacement motor has been identified and purchased, this will be rectified. Figure 9 shows pictures of the completed facility.

This facility can test sensors and materials over a range of temperatures including very high values, over a range of Reynolds numbers that can be varied rapidly with a bypass valve to evaluate thermal-dynamic response, at a reasonable flux value that can be varied nearly 7% (up to 100 Hz eventually) to deterministically evaluate sensor transfer functions. This is quite likely a unique combination for sensor testing, particularly for gas-cooled reactors and pebble bed reactors.

Parameter	Value
Maximum temperature the test sensor position	800 ºC
Maximum air flow rate in the flow loop at STP	8.0×10^{-3} m^3/s
Maximum Reynolds number at STP	2.7×10^4
Maximum neutron flux on the test sensor position	2.87×10^{11} nv
Difference between hot-leg neutron flux and mounted fission chamber neutron flux	< 2%
Nonlinearity in flux measurement vs. reactor power	< 5%
Peak-to-peak flux oscillation	6.6%
Maximum oscillation speed (currently)	50 Hz

Table 2: Summary of Results for In-Reactor Test Facility

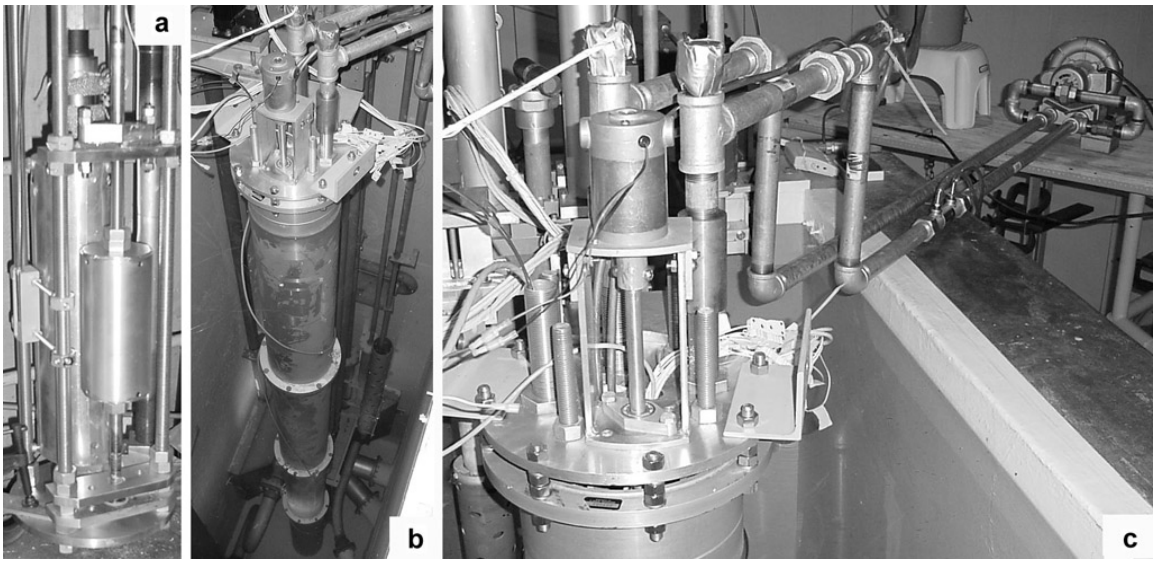

Figure 9: Completed Test Facility

The facility has performed well in the limited testing that has taken place since its installation, but several upgrades have been completed to enhance performance. These upgrades include replacing the brush type DC motor with a brushless DC motor and a more sophisticated controller. The new motor is has higher torque than the motor it replaced, and is able to reliably maintain any shaft speed up to 6000 rpm. The controller/power supply used with this motor allows several methods of speed control and

drag compensation. Currently it uses the motor's three internal hall-effect sensors to maintain a set speed regardless of the resistance. This important for our testing because the old motor required manual compensation, and could not maintain a specific speed. The oscillator shaft has several large bearings lubricated with thick grease, which produced an effect whereby if frictional heating raised the temperature of the grease, the shaft drag decreased, resulting in a corresponding increase in the shaft speed. The new motor and controller is able to detect speed change and compensate so that once a speed is set, it is maintained. This provides more consistent test data, and avoids the need for manual adjustment of the rotor shaft speed.

The motor to oscillator shaft coupling was changed. The old coupling was a solid aluminum sleeve that required careful alignment of the motor with the shaft. Some early operations noted slight but unexpected vibrations. These vibrations were caused by minor misalignment of the motor and shaft. The new motor is coupled to the oscillator shaft with a pliable rubber coupling. This coupler is tolerant of some misalignment and should eliminate the vibration.

An additional copper cooling coil was added to the air blower return (from the furnace) line. This further reduces the temperature of the air reaching the blower and lower the temperature of the air conduit. To ensure adequate cooling water flow, a larger capacity pump was bought and tested.

The design of the LVEC facility allows periodic upgrades or repairs if necessary. To ensure a quick turn around if repairs are necessary, replacements for some of the more complex assemblies were fabricated. The heater assembly consists of several parts that are difficult to fabricate, and since this is the part of the test facility that is both most important to testing and most likely to fail, it is important to have a spare assembly on hand. The parts of the assembly are shown clearly in Figure 10, with (I) being the electrical resistance heater (the item most likely to fail).

Another component that was produced as a spare was the neutron oscillator assembly. This assembly is situated in close proximity to the heater, and due to radiation concerns both would likely be replaced if either were faulty. The availability of these components leaves spare parts for most of the critical components.

An issue remaining from the construction of the test facility was how to introduce and hold test sensors in the correct position and orientation for testing. This was a challenging problem because the sensors have to be lowered 18 feet into an environment of high temperature, high radiation flux, and small space. The need for repeated retrieval and insertion of tests sensors required that any holding apparatus material, decay rapidly after activation. The high temperatures experienced in most locations in the flow loop combined with the necessary 18-foot length required that anything used to hold sensors be designed considering thermal expansion. After several attempts using various materials, the best solution was the use of alumina tubes. Alumina (aluminum oxide) activates to short half-life isotopes, and does not expand excessively with temperature. The alumina tubes chosen were three feet in long and 3/16 inches in diameter. It is available in a high purity form, in convenient, three-foot lengths. Joining six three-foot sections into a single 18-foot section requires mechanical couplings. The couplings were made from aluminum alloy 6061, which is the material chosen for much of the LVEC facility, for consideration of similar issues such as activation product half-life. The couplers were press and shrink fit onto the alumina tubes, in a manner such that they will not detach.

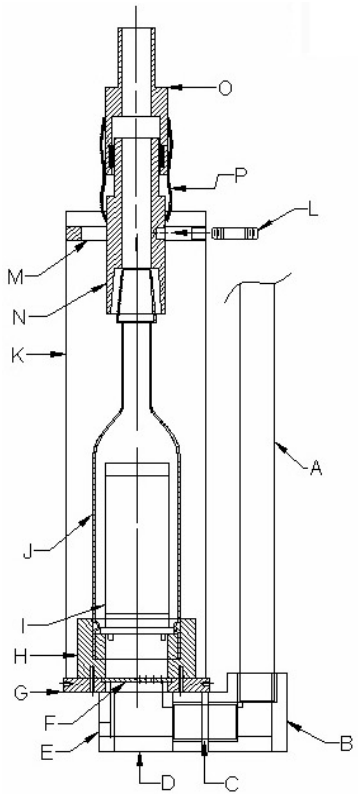

Figure 10: High Temperature Heater Assembly

The construction method used to produce the sensor mounting apparatus is as follows. The alumina tubes were specified to have an .1875-inch nominal outer diameter, but the tubes we received had a large degree of variability, so actual diameters ranged from .183 to .194 inch. This was not a problem because the tubes used were recycled from an earlier project, so that we had an abundance of samples to choose from. The tube diameters were measured at each end using a micrometer and were selected to be no smaller than .189 inch (ranging to .191 inch). Cutting 5/16 inch diameter aluminum stock to 3.1 inch lengths created the sleeves. The sleeves were drilled and enlarged to .1865 inch inner diameter. Figure 11 shows some of the materials and tools used in the construction process.

Into half of these couplers, a 2.9 inch length of 3/16 diameter aluminum rod was pressed. This was done by holding the sleeve in a lathe chuck, and the rod in the lathe tailstock chuck and advancing the tailstock, without heating either piece. This process created the “male” coupler. Inserting a 3/16 inch ream into half of another sleeve created

a female coupler. Matching sets were made by drilling keyholes into the assembled couplers as shown in Figure 12.

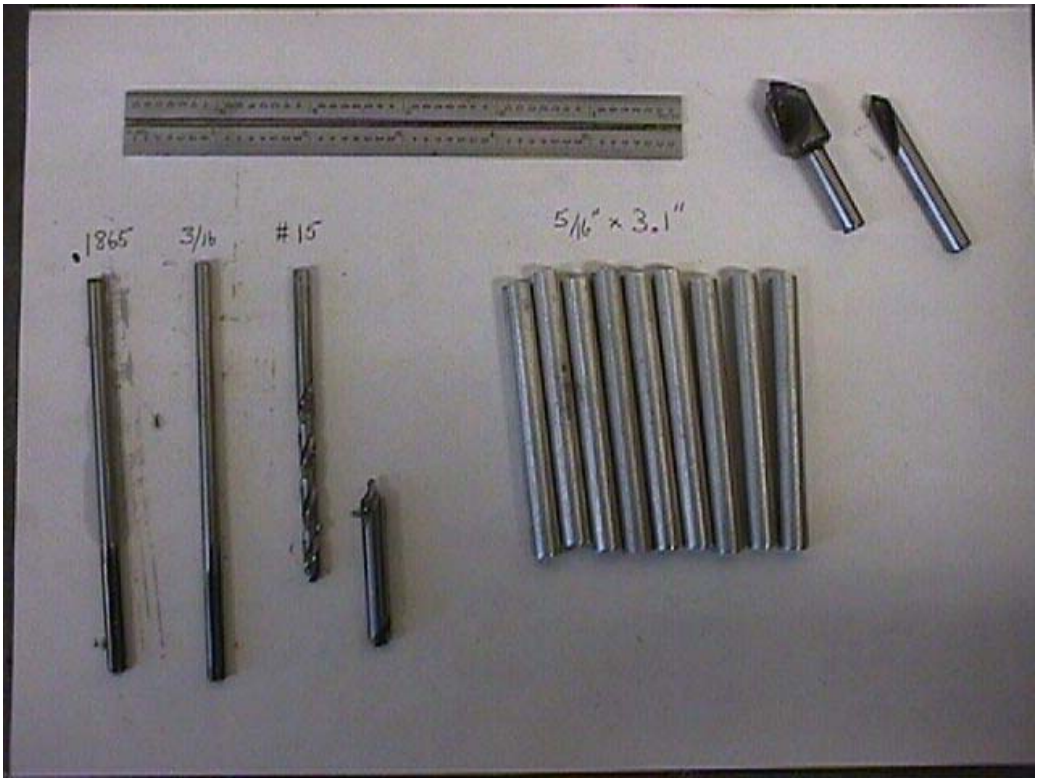

Figure 11: Tools And Materials Used For The Alumina Couplers

These holes are intended to be used with lock wire, which allows two aluminum rods to be joined. Once five coupler sets were made, the couplers were shrink fit onto the correct ends of the alumina tubes. This was done by inserting an alumina tube into the headstock chuck (using a paper buffer to prevent the chuck from crushing the tube), and inserting the correct (male or female) coupler into the tailstock chuck. The tailstock was then advanced, and heat from a handheld torch used to expand the inner diameter of the sleeve. These steps are shown in Figures 13 through 15.

The couplers were installed in the correct sequence, and each tube was numbered to allow easy assembly. Assembly of the alumina tubes requires only that mating couplers be matched, and the lock wire inserted. This lock wire is titanium, which has enough strength to be able to function as a tube spacer. That is, the wire will provide a

stand off from the hot leg pipe wall, and position the alumina tube in the center of the pipe.

Conservative calculations indicate that there is no possibility of heating the shrink fit aluminum sleeves enough to allow them to loosen and be pulled from the alumina tubes. Testing of this system using conservative sizes (smaller diameter alumina tube than was used) showed that the coupler would not fail until heated to the melting point of aluminum. At three feet up from the sensor (the coupler at the point closest to the heat source in the LVEC facility) the temperature never exceeds 450° C., which is a compatible temperature for the alumina-aluminum structure.

To mount the sensors in the correct orientation, another sleeve was fabricated using 5/16 inch titanium. A handmade wire structure was welded to the sleeve that was shaped to accommodate both sensor geometries. This welding used using a TIG welder and argon shielding gas. This sleeve was then shrink fit onto the end of the lower piece of alumina. This titanium piece will be in the zone that experiences the maximum 800° C. during operation. Another titanium piece was tested at 950° C. for four hours, and though it showed some oxidation, there was no loss of mechanical strength. Calculation and testing showed that the sleeve was not removable from the alumina tube even at this higher temperature. Since the titanium wire extends from the end of the sleeve roughly 0.75 inch, it is likely that the maximum temperature experienced by the sleeve itself will be somewhat less than 800° C.

Figure 12: Drilling Lock Wire Holes In The Coupler Set

The sensor (of either geometry) is securely fit in the titanium wire sensor holder. Once the sensor is in place, leads will be soldered to the sensor leads. The wire chosen to mate to the platinum of the sensor lead is a silver coated copper 14-gauge wire. This wire has a high temperature fiberglass-insulating sleeve. The silver coated wire is rated for temperatures up to 1000° C., but should experience no more than 700° C. The silver solder is designed to be used in temperatures up to 650° C., which is lees than is needed, but testing has revealed that this solder maintains its electrical conductivity above 650° C., but loses mechanical strength. At about 700° C., we believe that sufficient mechanical strength will be maintained to keep the wires together, since there will be no requirement for weight bearing or other physical stress. If this solder proves to be inadequate in bench tests, each sensor lead will be spot welded to the corresponding lead wire before insertion.

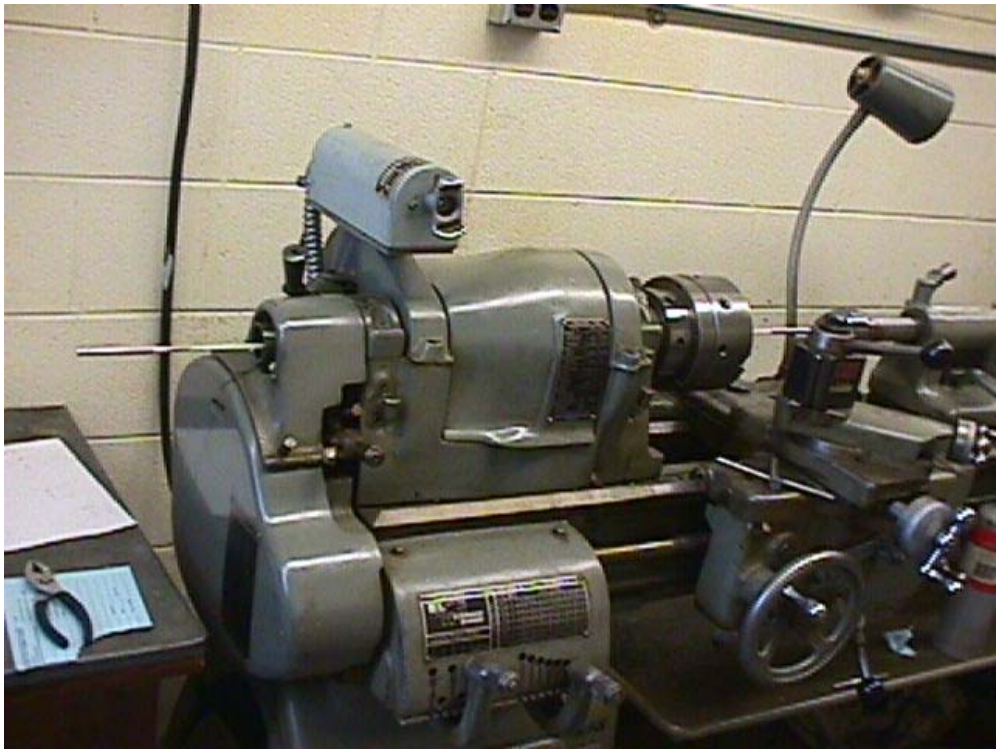

Figure 13: Alumina Tube Inserted Into The Headstock

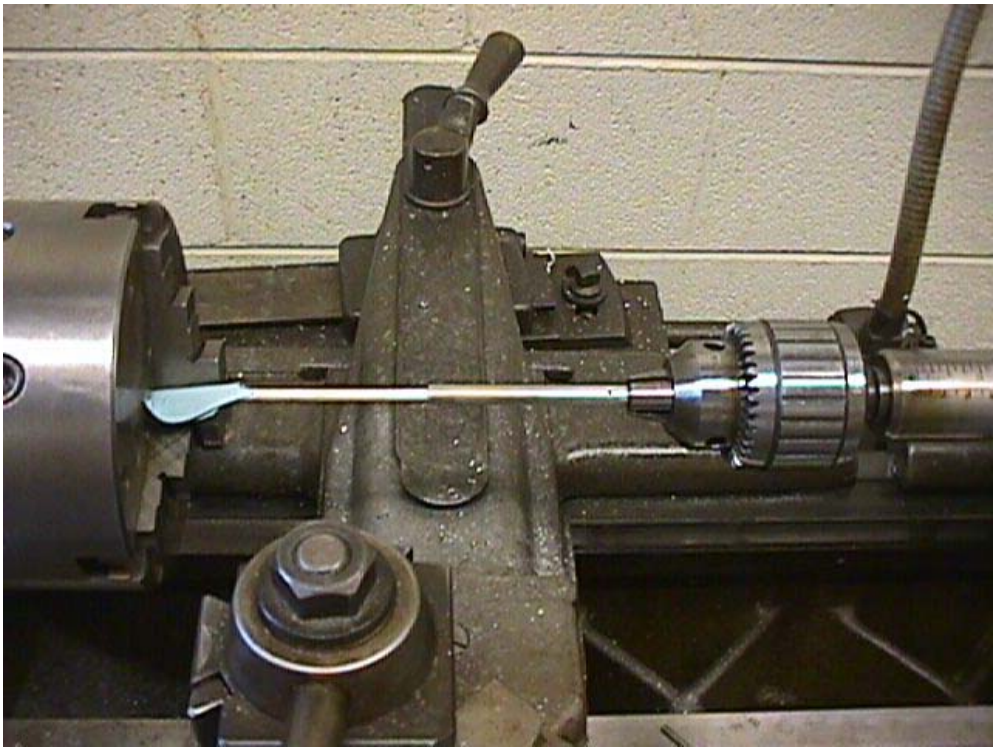

Figure 14: Assembly Setup Before Applying Heat

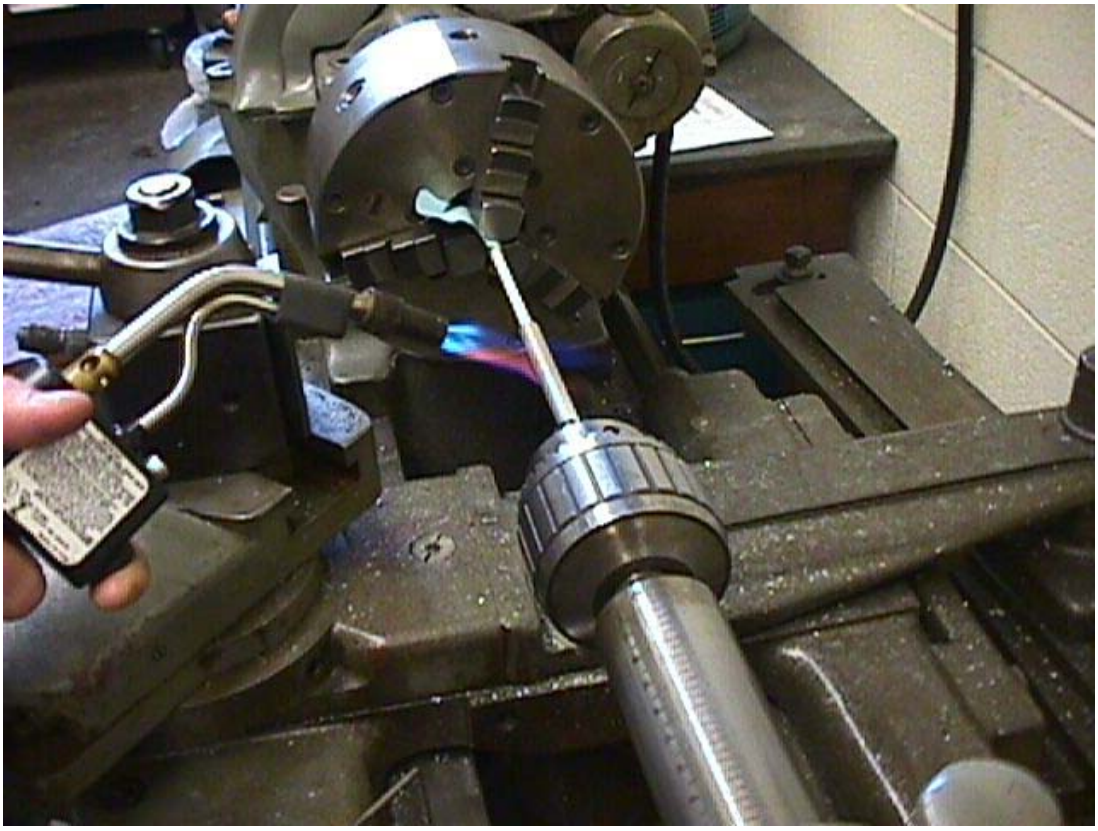

Figure 15: Applying Heat And Installing The Coupler Sleeve On The Alumina Tube

2.3 COMPLETION OF THE CONTROL AND DATA ACQUISITION SYSTEMS

The sensor feedback control and data acquisition (DAQ) system performs three functions:

1. maintenance of a constant sensor temperature,
2. execute algorithm(s) to test sensor dynamics, and
3. recording all signals relevant to sensor operation evaluation.

A study was completed to compare use of a stand-alone digital controller versus a computer-based controller to determine which better meets the requirements listed below:

1. Sample Rate:

   A rate of 200 samples/second, which is fast enough for sensor control, as well as permitting estimation of power spectral density (PSD) functions of reasonable bandwidth for evaluation of sensor dynamics.

2. Number of Channels:

   At least four analog input and two analog output channels for control of up to two sensors at a time.

3. Sampling Resolution:

   Previous studies indicated that 12-bit resolution was insufficient for providing the desired measurement precision. Thus, 16-bit resolution is specified.

4. Computing Power:

   Sufficient to allow execution of a variety of control algorithms as well as system housekeeping functions.

A computer-based control and DAQ system was selected, and two computers running Windows NT with National Instruments (NI) DAQ cards were purchased and tested. One computer controls the sensors and performs algorithms to test sensor dynamics, and the other streams data to disk. A custom interface box was designed and built to interface the sensors with the computers.

The interface provides the voltage dividers which condition the sensor signals for input to the computer DAQ card, and the power gain necessary for converting a DAQ card output to operating currents for the sensors. In addition, the interface box filters the input sensor signals with 6^{th}-order 500 Hz Bessel filters to allow generation of PSD plots from sampled data without aliasing.

Figure 16 shows a simple schematic of one channel of the interface box. Differential voltages proportional to the voltage drop across the sensor and the current through the sensor (voltage drop across a 10-ohm resistor in series with the sensor) are passed through low-pass filters and input to the control computer. The control computer processes these voltage and current measurements in an algorithm such as PID control to generate a control signal. The control signal establishes the current through the sensor by adjusting the gate voltage of an FET transistor in a feedback configuration. The source current from the FET, which is controlled via the non-inverting feedback loop seen at the bottom of the figure, is the same current that is passed through the sensor.

The design has been completed. A local company familiar with fabrication of electronic systems has produced a detailed schematic and circuit board layout and built the electronics board. The interface box has been assembled and tested. Figure 17 shows the circuit board of the interface box. The white cables on the left connect the interface box to the control and DAQ computers using NI 68-pin connectors, and the sensors and DC supply voltages connect to the interface box via jacks on the front. Power MOSFETs and resistors are mounted separate from the board in the interface box for better cooling, and are not seen in the picture.

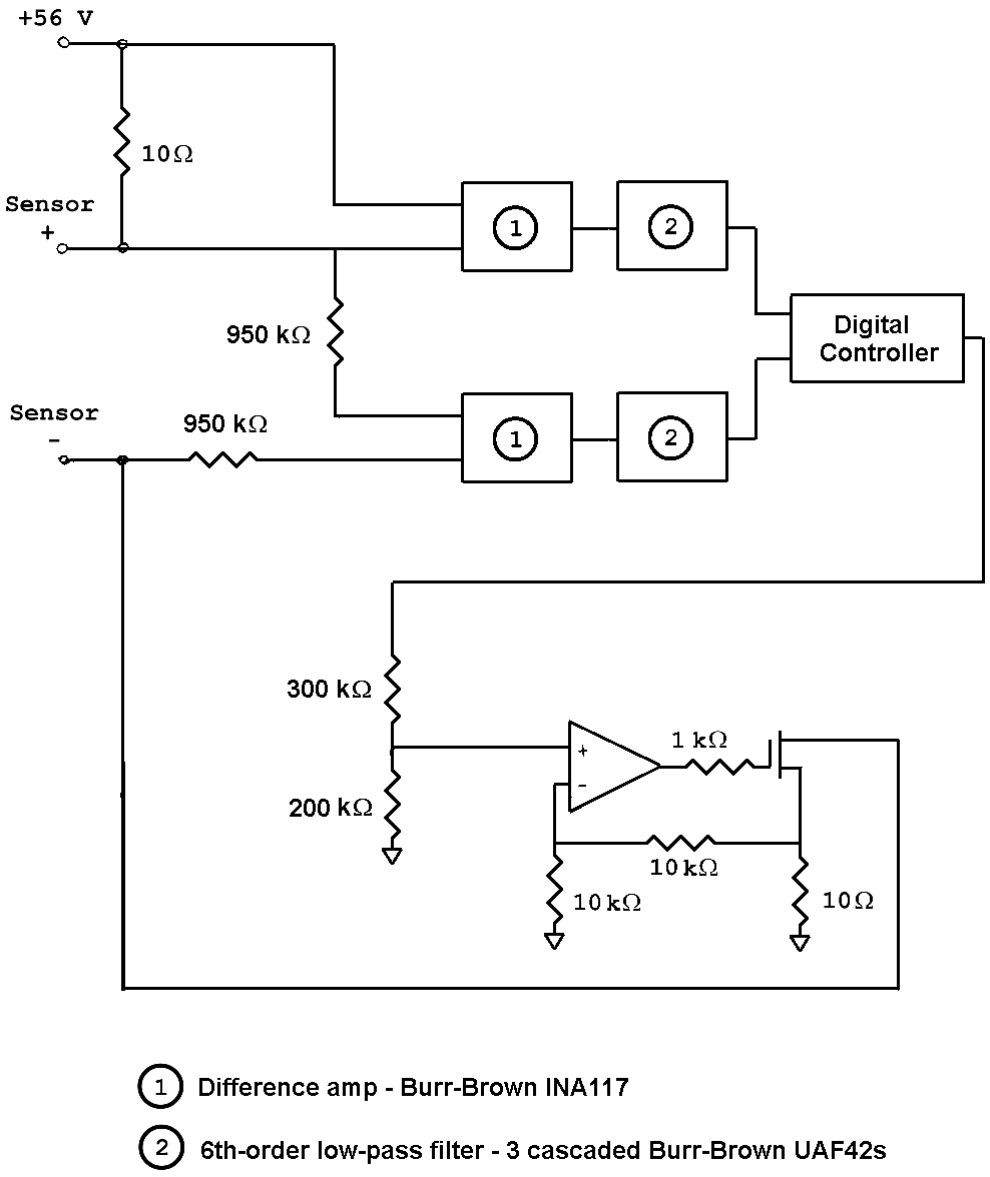

Figure 16: Simple Schematic of Single Channel of the Interface Box

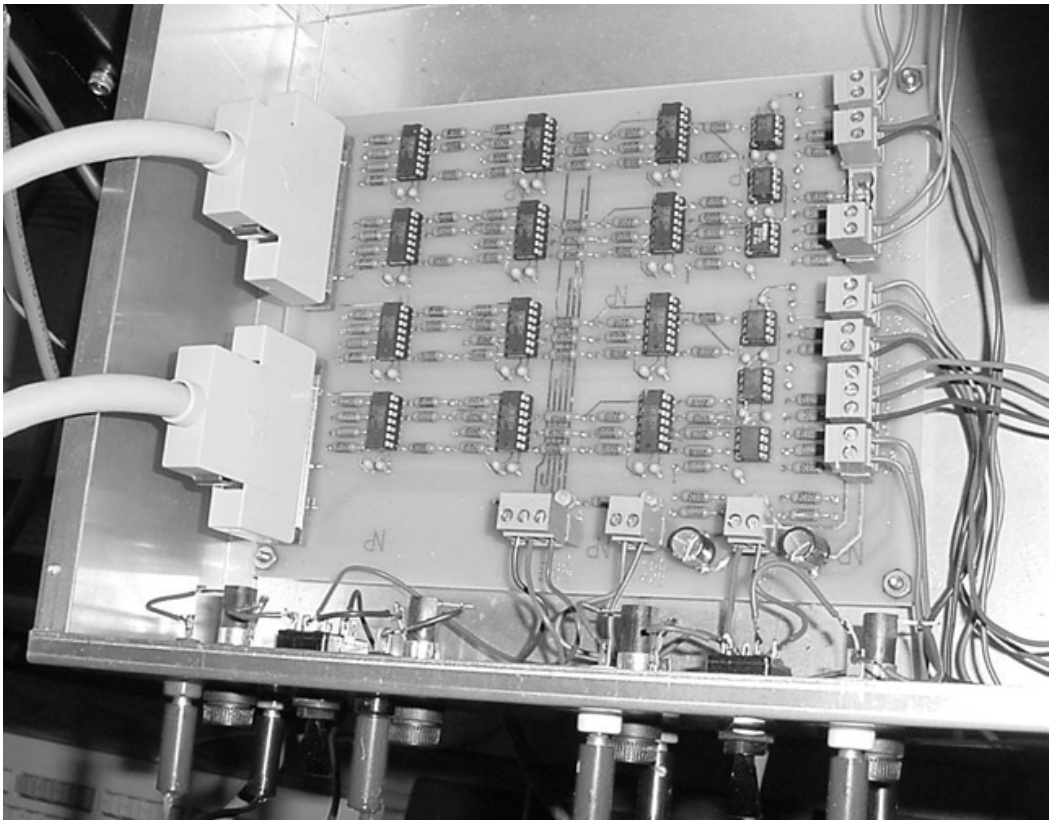

Figure 17: Control and DAQ Interface Box

The control computer contains two DAQ boards, each of which has eight differential analog inputs and two analog outputs. The first board samples the sensor voltage and current signals and provides control signal outputs. The output signals from the second board are proportional to compensated power estimates to be recorded by the DAQ computer.

To verify that the control computer with its NI DAQ card could provide reliable control at 2 kHz, it was tested in a simple control configuration. A 60 Hz sine wave was connected to the input, the LabVIEW virtual instrument software applied the input to the output, and the two signals were captured and compared on a digital oscilloscope. Figure 18 shows this comparison. The control computer accurately tracks the input with a short delay, except in a few instances. In these instances, the output voltage latches for an extra time step or two because the operating system consumes enough processor resources that the controller state cannot be updated within the required time window.

Further testing has shown that this control system works well for controlling dummy sensors, and will be discussed in the section of this report on the software portion of the controller.

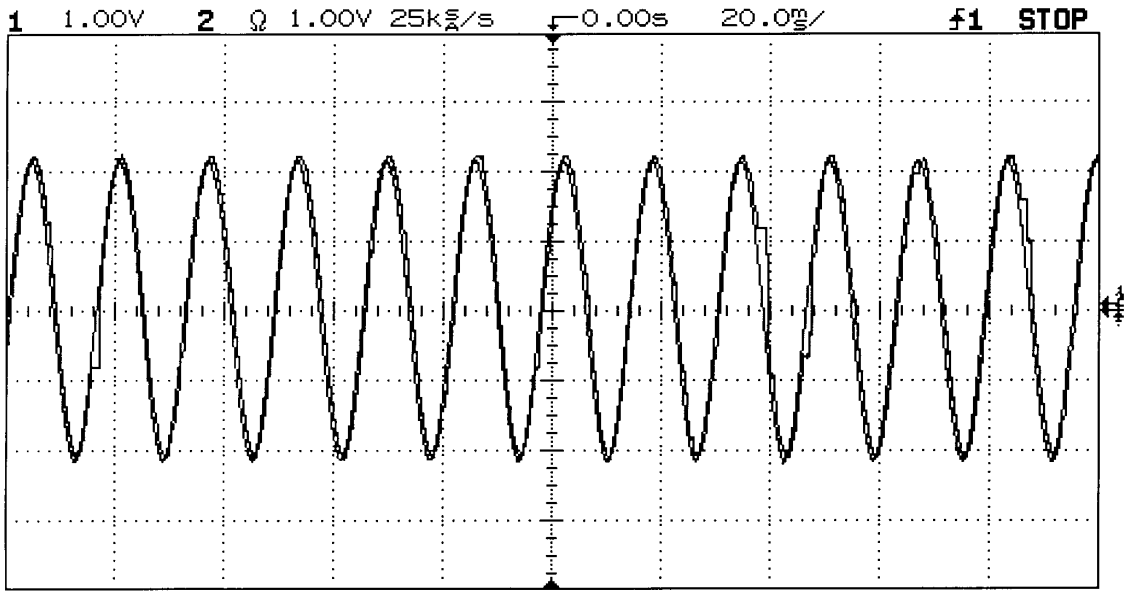

Figure 18: Control Computer Test With A 60 Hz Sine Wave

The DAQ computer monitors a number of parameters, which include:

- Test sensor measurements
    - Test sensor voltage and current for two sensors
    - Test sensor control signal for two sensors
    - Compensated power signal for two sensors
- Baselines for comparison to test sensor measurements
    - Neutron flux measurement from fission chamber
    - Gamma exposure rate measurement from gamma ionization chamber
    - Temperature in high-temperature facility
    - Oscillator rotation measurement
- Flow loop measurements
    - Flow loop temperature profile measurements
    - Gas flow rate
- Facility measurements
    - Ambient and component temperatures in the LVEC
    - Structure acceleration measurements

The test sensor voltages, currents, and control signals are acquired through a DAQ card connected to the interface box, and the remaining signals are acquired through a DAQ card connected to a signal-conditioning chassis that multiplexes the signals to allow more to be captured by a single card. All of the signals are sampled at 2 kHz, averaged once per second, and written to a tab-delimited text file. If data for PSD plots is desired,

the data for all or a select number of signals can be streamed to disk at the sampling speed.

Much of the equipment that comprises the control and DAQ system is mounted in an instrumentation chassis, shown in Figure 19. This chassis contains:

- DC Power supplies
- Control and DAQ interface box
- Pressure transducers that connect to the flow element in the flow loop
- Instrumentation for control and measurement of oscillator speed
- DAQ signal-conditioning chassis
- DAQ signal breakout boards
- Networking hub to allow DAQ and control computers to exchange data

The interface box is the silver box at the front of the chassis, and the control and DAQ computers are positioned to either side of the chassis.

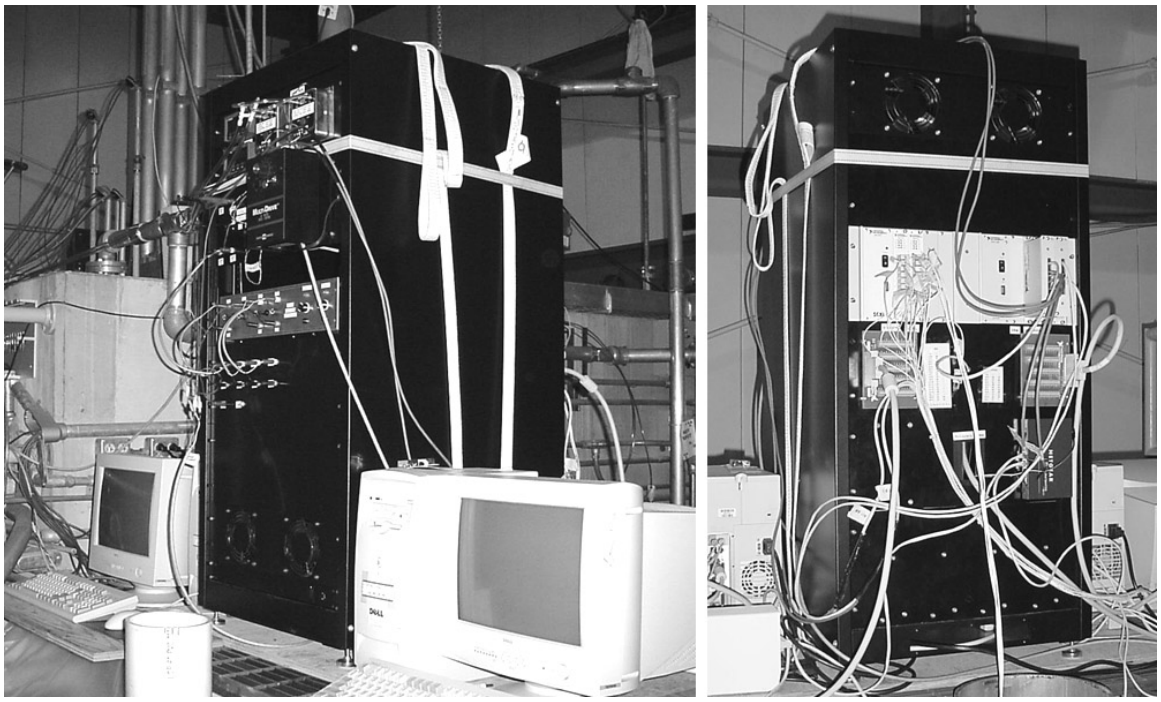

Figure 19: Instrumentation Chassis

2.4 COMPLETION OF ANALYTICAL MODELING

Difficulties encountered in attempts to fabricate the original CTPS senor have led to the development of an alternative sensor design, the Planar Constant Heat Flux Power Sensor (CHFPS). In addition, temperature compensation is currently a topic of study and an issue to which the CHFPS is expected to be less sensitive. The CHFPS sensor maintains a constant temperature difference between two points on the sensor. It employs a temperature differential as the set point variable and involves selecting two points on the sensor and monitoring the temperature difference between them. The planar sensor is an alternative design that promises greater ease of construction and reduced complexity. Figure 20 shows the planar sensor design concept.

The technique for fabricating the planar sensor is briefly described below. It is essentially the same method used in screen-printing heater elements and similar devices.

The first component to be considered is the substrate upon which the platinum heater and fissile material are to be printed. The first generation planar sensor uses alumina (AL_2O_3) as its principal housing material. The simple method in which all of the materials are laid down upon the substrate is sometimes denoted as screen-printing. This, in fact, is exactly the process involved. Screens are made from stainless steel mesh fashioned in the required dimensions and fastened to the printing apparatus.

The disk shaped alumina substrate has two holes drilled to allow fastening of lead wires to the heater circuit. An ink containing platinum in suspension is printed on the alumina disk in a manner consistent with the depiction in Figure 1. After printing and drying, the sensor is fired at temperatures above 1300 °C and the platinum ink becomes a cohesive continuous platinum heater coil. Desired resistance values can be reached by applying subsequent printings and firings.

Highly enriched uranium is then printed in the same manner over the existing platinum coil. Printings and firings are done until the desired fissile loading is reached and the sensor construction can be completed.

The housing of the first-generation sensor is exclusively alumina. The housing includes the base substrate disk upon which the platinum and uranium are printed, an alumina ring that creates the outer wall of the sensor and another alumina disk as the cap. The alumina pieces are held fast with feldspar ink applied to the substrates by the same screen-printing process described earlier. The feldspar melts to form a glass seal after firing. The final firing of the sensor is done in a vacuum furnace to avoid generating high pressure by heating gases within the casing and to provide a reservoir for fission gases.

Variations on this basic design include sensors that have an intervening layer of alumina between the platinum heater and the fissile uranium layer and sensors that are packed with alumina powder to increase the conductive nature of the void above the uranium oxide layer.

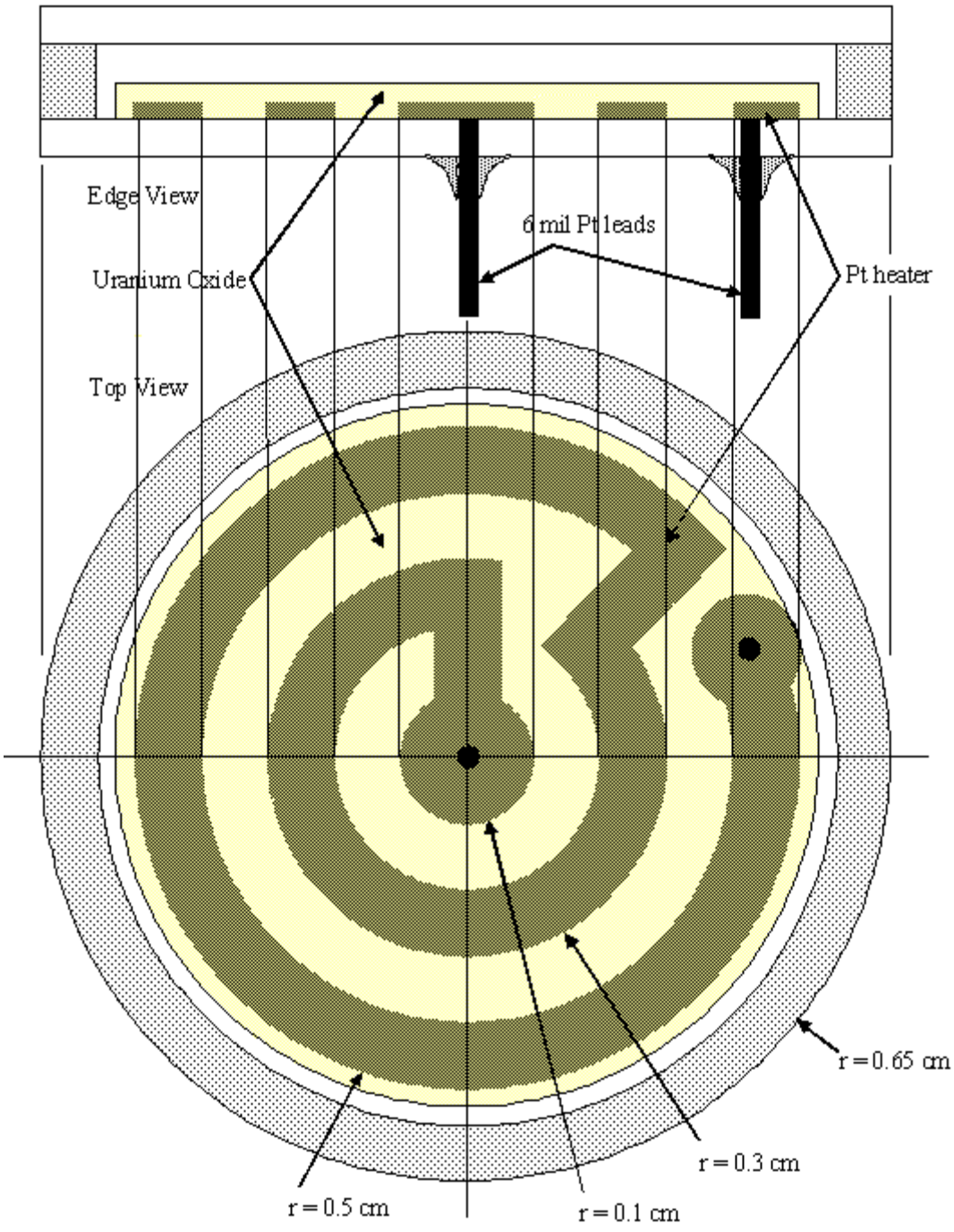

Figure 20: Planar Sensor Configuration

It is thought that fission fragments bombarding the platinum heater may threaten the longevity and integrity of the platinum heater and lead to sensor failure. The effect of this layer on sensor performance is evaluated in a thesis as it applies to the first generation sensors. A scoping calculation to determine the thickness of protective layers of alumina and beryllium oxide was done by using the software package SRIM (Stopping Range of Ions in Matter, available for download at www.SRIM.org). The SRIM simulation shows the results of impinging 100 Mev Yttrium ions upon layers of alumina and beryllium oxide. A layer of 15 microns of either material appears to be sufficient to protect the platinum from the lightest and highest energy ions. Two of the first generation sensors were made with a layer of alumina and as mentioned earlier, the effect of this layer on sensor performance is investigated in the thesis.

The numerical model has been modified to reflect the new sensor geometry with different boundary and symmetry conditions. The numerical model simulates heat transfer from the sensor to the environment considering power deposition due to gamma interaction, electrical power delivery, and fission events. Figure 21 shows a block diagram of the sensor numerical model.

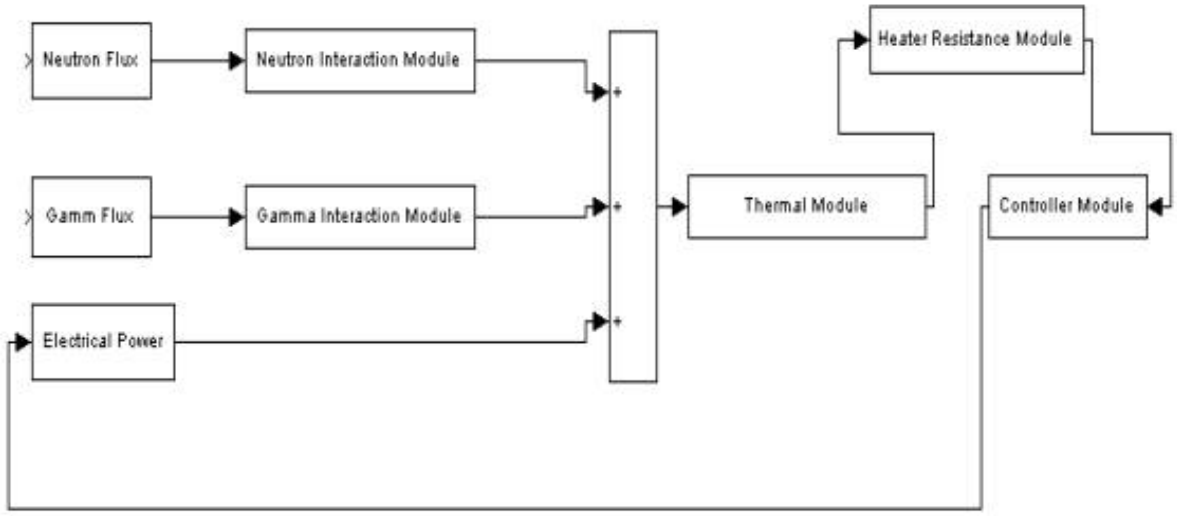

Figure 21: Block Diagram Of The Sensor Model

As its name implies, the CTPS sensor operates by delivering an appropriate amount of electrical energy to a platinum wire such that the combination of deposited nuclear power and deposited electrical power maintain a pre-selected resistance level. Obviously, maintaining constant resistance implies constant temperature. Detailed chemical and material information regarding the CTPS construction components can be found in the January-March quarterly report to the Department of Energy Nuclear Energy Research Initiative. Conversely, the CHFPS employs a temperature differential as the set point variable and selecting two points on the sensor and monitoring the temperature difference between them to achieve this. The CHFPS numerical model employs similar methods in calculation of temperature field distribution and nuclear deposited power but it has quite different design/structure and control method.

The numerical model adapted from the CTPS model to simulate the CHFPS contains the three major modifications listed below:

- modification of the thermal module and input/output interface to reflect the sensor geometry with different boundary and symmetry conditions,
- modification of the control algorithm for the CHFPS control and measurement, which are different from the CTPS, and
- improvement in computation speed.

The methods used in the CHFPS thermal module are basically identical to the CTPS numerical model and thus are omitted in this report (see previous progress reports for details). The thermal module calculates the temperature distribution in the sensor. The platinum heater resistance, a function of temperature, is calculated based on the instantaneous operating temperature of each platinum heater node. Inputs to the thermal module include nuclear and electrical heat shown in Figure 21. The thermal characteristics of the sensor are dependent on a convection coefficient h and an ambient coolant temperature T_∞ from the initial conditions defined by the programmer. The module applies the convective heat transfer coefficient to each node on the outer parts of the sensor, the so-called zero mass nodes, without regard for the nodes residence in the coolant flow. In other words, the convective heat transfer is taken to be the same at the

surface of the sensor facing upstream as the surface of the sensor facing downstream. The module outputs are the temperature distribution matrix referred to as *T* and the platinum heater resistance value that will be used to calculate electrical power deposition in the subsequent time-step. As mentioned earlier, the module assumes radial symmetry and uses a finite difference method. The resultant geometry to be considered is an r-z plane representing radial and axial node positions. The finite difference method requires that the sensor be defined as a sequence of nodes.

The nodal layout and the corresponding geometrical and material parameters inputs are quite different for the CHFPS from the CTPS. Figure 22 shows the nodal layout of a CHFPS sensor similar to those of the first generation planar variety. This sensor was meshed with 30 radial nodes and 12 axial nodes. The resulting two-dimensional geometry has nodes representing azimuthally uniform annular regions. The annular solids are chosen to faithfully represent the cylindrical nature of the sensor. The actual node position is the center of each cell and quantities such as node-to-node conduction path lengths are taken from the node center to the node edge of the first material and the node edge to the node center of the next material. Node sizes also differ, as do material types.

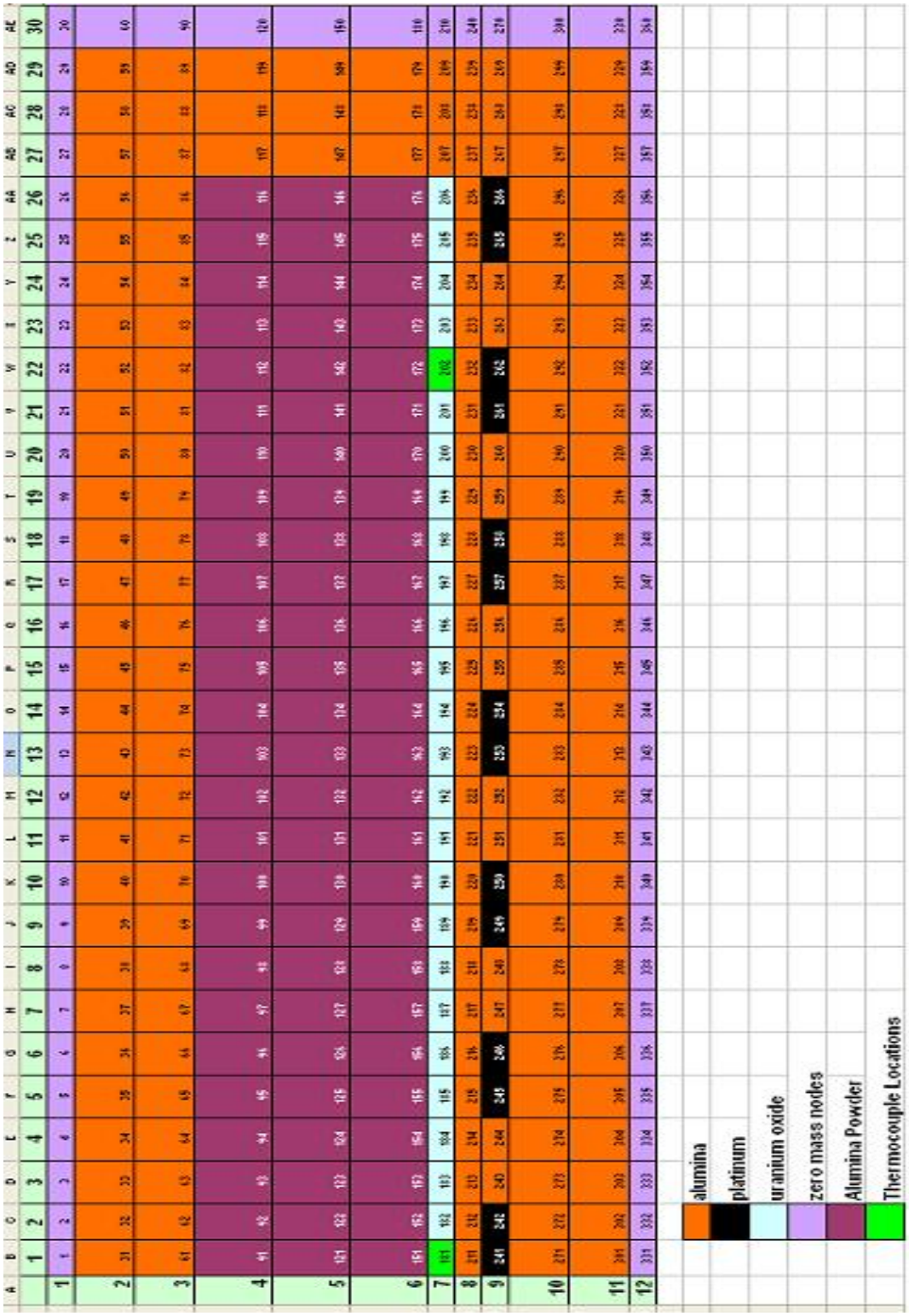

Figure 22: Nodal Map With Thermocouple Positions Identified

The original CTPS model uses a proportional controller with an error input between the temperature setpoint and measured/calculated sensor temperature. The CHFPS uses an error input between the temperature difference setpoint and measured/calculated temperature difference at two optimally selected locations for two thermocouples.

Scoping calculations for the sensor were done with a simple proportional control algorithm implemented for evaluation of the constant heat flux cylindrical sensor. The proportional gain used for the simulations was $0.005\frac{amps}{^{o}K}$. The type of proportional control implemented in earlier models differs from classical proportional control in that the error signal is the difference between the recent ΔT and the set point ΔT_o and the output signal is an incremental change in current, dI:

$$dI = G(\Delta T_o - \Delta T), \tag{1}$$

where G is some proportional gain relating the error of temperature difference $\Delta(\Delta T)$ and dI. Henceforth this control scheme will be referred to as the 'delta I' controller.

Traditionally, the output would be a new value of sensor current as follows:

$$I_0 = Kp(\Delta T_O - \Delta T), \tag{2}$$

where K_p is proportional gain relating $\Delta(\Delta T)$ and $I_{O.}$ The mode of operation of the original proportional controller was not deeply considered until the design of the more advanced controller with integral and derivative control was undertaken.

Initially nearly all of the simulations were run with the delta I controller. The control scheme works very well in that there is essentially zero steady state error and indicated response times are faster than traditional proportional control. The significant disadvantage of the method is its inability to avoid overshoots. The current supplied to the sensor is not modified until the set-point temperature is reached. For example, if the

setpoint for maximum current delivered to the sensor is 0.8 amps, the controller supplies current until the set point is reached, at which point it begins to reduce power.

Once the sensor with the largest bandwidth (beryllium oxide coated platinum sensor or BCPS) was identified based on the delta I controller, the pursuit of creating a numerical controller with proportional, integral, and derivative control (PID) began. The PID controller is described in s-domain as follows:

$$D(s) = K(1 + \frac{1}{T_I s} + T_D s), \tag{3}$$

where T_I is integral time, T_D is derivative time and K = proportional gain.

The purpose here is to re-write the above equation in a form that is discretized in the time domain. Applying the inverse Laplace operation we have the controller output (current increment ΔI) in the form of:

$$L^{-1}\{D(s)E(s)\} = K[e(t) + \frac{1}{T_I}\int_0^t e(t)dt + T_D \frac{d}{dt}e(t)], \tag{4}$$

where the quantity e(t) is the error signal between the temperature difference set point ΔT_O and the actual temperature difference ΔT:

$$e(t) = (\Delta T_O - \Delta T). \tag{5}$$

The derivative term in Eq. (4) is approximated with the backward difference method. The integral term is expressed as follows:

$$\int_0^t e(t)dt = e_n \Delta t + F_{n-1} \tag{6}$$

where:

e_n = Error signal at the n-th time step

$$F_{i-1} = \sum_{m=1}^{n-1} e_m \Delta t \tag{7}$$

Finally, Eq. (4) is cast in the form of Eq. (8) that can be directly written into the MATLAB code as a functional PID controller:

$$d(t) = K[e_n + \frac{1}{T_I}(e_n \Delta t + F_{n-1})] + T_D \frac{e_n - e_{n-1}}{\Delta t}] \quad (8)$$

where the d(t) term is the controller output signal.

Applying the Ziegler-Nichols tuning method and performing subsequent iterations accomplished controller tuning. Ziegler and Nichols defined two methods of tuning system parameters. The first method is tuning for a quarter decay ratio by analysis of a process reaction curve obtained from open loop control of the system. The second involves increasing proportional gain until reaching the marginally stable condition of continuous oscillation.

Initially it was thought that the open loop process reaction curve method would be the best way to tune the controller. Allowing the sensor to come to steady state with a constant current and applying a step change to the current value created the process reaction curve. All of the model modules were functional, implying that neutron and gamma interactions occurred as normal. The process reaction curve is shown in Figure 23.

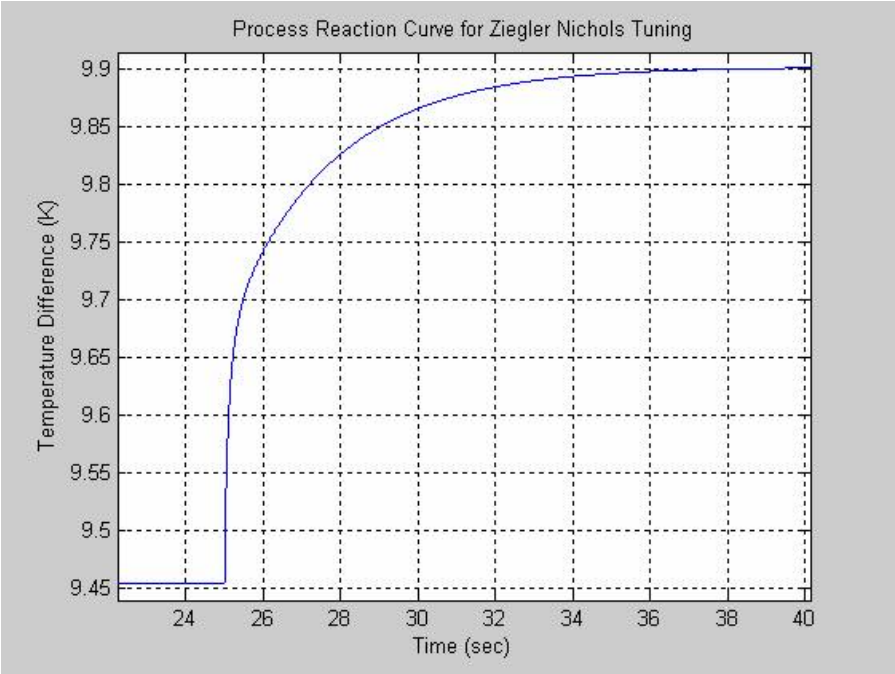

Figure 23: Process Reaction Curve For Controller Tuning

Analysis of the figure reveals an interesting aspect of the behavior of the code. The process reaction curve was expected to show a measurable time lag. As soon as the current value is changed, the temperature values reported from each thermocouple change. There appears to be no observable time lag. Heat is transported into the platinum heater nodes and begins to migrate to surrounding nodes. The thermocouple positions are picked as nodes in the uranium. The proposed design of the sensor calls for the thermocouples to be located directly on the layer of fissile material. This design was approximated as seen in Figure 22. This location promises the fastest response time as thermal energy is rapidly transferred from both the platinum heater and the uranium oxide layer. Note that Figure 22 is a broken representation where middle nodes have been removed in order to present the picture more clearly. The mesh may be too coarse to adequately identify the very short time lag. The model allows for only one node between the platinum and thermocouple, which means that in a single time step the heat generated in the heater node is calculated as heat entering the thermocouple node. This effect requires resorting to the ultimate gain method of tuning the controller.

The ultimate gain method turned out to be less time consuming than initially expected. The code shows signs of stability or instability relatively quickly. The iterative process of finding the ultimate gain K_u begins by incrementally increasing proportional gain. As noted earlier, a gain of 0.005 $\frac{amps}{^oK}$ was used for all of the simulations until the fastest performance was observed. The K_u identified after about 10 iterations was approximately 24.0625 $\frac{amps}{^oK}$. Values for T_I and T_D were determined using the following relationships:

$$K = 0.6K_u, \quad T_I = 0.5P_u, \quad T_D = 0.125P_u, \tag{9}$$

where P_u is the ultimate period or the period of oscillations during ultimate gain operation.

As simulations for the planar sensor were performed, the 1,000,000 step steady state cases required close to four days of run time on a 1.3 GHz Intel Celeron processor. At this rate multiple cases would require a great deal of processing time. As the code runs, information such as thermocouple temperature, output current and power production are recorded for future analysis. In the previous simulation code, MATLAB rewrites the entire matrix each time step instead of simply adding a value to a stored running matrix. That is, as run time increases to hundreds of thousands to a million time steps near the end of the simulation, the computer is writing a matrix with five columns and essentially one million rows each times step. For the 0.00005-second time step simulation above the matrix approaches two million entries.

The addition of a module that flushed the workspace incrementally solved this problem in the modified code. The algorithm divides the total number of time steps to be carried out by 20. Consider the steady state cases in which the ultimate number of time steps is one million. As the simulation passes each multiple of 50,000 the code saves the desired information to the hard drive and flushes the operating data collection matrix. This algorithm is extremely effective in increasing the speed of the code. The speed

increase reduced the 3.7-day or 88.8 hour run time to 1.17 days or 28 hours. This change represents an overall speed increase of 3.17 times.

We have completed a thorough study involving parametric analysis of the constant heat flux power sensor for the planar geometry, with the goal of enhancing the numerical simulation of the sensor and optimizing its performance. Given that the sensor may be used in safety-related power monitoring channels, it must have a fast response time to adequately respond to anticipated transients and activate downstream safety channel functions. The sensor performance simulations were carried out in MATLAB using a numerical model that was modified from previous simulations of CTPS sensors.

Sensor bandwidth was a primary consideration throughout the optimization process. In general, there is a tradeoff between sensitivity and bandwidth. The CHFPS sensor contains 15 milligrams of fissile uranium. Since current-generation miniature fission chambers used for in-core power monitoring have about 2 milligrams of enriched uranium, it could be inferred that the planar sensor has the potential for being a sufficiently sensitive instrument. The goal of the numerical simulation of the CHFPS is to determine the combination of materials and configurations that produce the optimum response time.

The environmental conditions used for the evaluation of the sensors are taken from the conditions expected in the Westinghouse IRIS reactor. Sensor performance was evaluated in two other environments to document model predictions for comparison with anticipated test results. The convective heat transfer coefficient was significantly reduced to reflect the heat removal conditions that the sensors will experience in the high temperature test facility at the OSURR. This facility features a high temperature loop in which heated air is directed across test sensors to simulate temperature conditions similar to those in an operating power reactor. Another simulation was performed in which the convective heat transfer conditions were modified to reflect the environment in a high temperature gas cooled reactor. The coolant was taken to be helium at an operating

temperature of 800 ^{o}K and operating pressure of 4.9 MPa. These operating conditions led to the use of an estimated heat transfer coefficient of 1750 $\frac{W}{m^2 K}$.

All results discussed from this point forward are based on simulations for IRIS conditions. These conditions include forced convective heat loss to water at 310 ^{o}C with an estimated heat transfer coefficient of 1000 $\frac{W}{m^2 K}$.

Each sensor with its unique materials and configuration was allowed to come to steady state in the environmental conditions expected in an operating reactor. In simulation time the steady state runs were performed for 100 seconds. Changes in the temperature profile were undetectable after about 30 seconds, with changes in output current becoming minor after about 25 seconds. A simulation time of 100 seconds assures attainment of steady state sensor operation. This is implied by the flat "plateau" region at the beginning of the frequency response curves.

Random fluctuations were imposed upon the neutron flux parameter for 50 seconds in simulation time to determine the bandwidth to an accuracy of approximately 0.5 Hz bandwidth. Other simulations such as step changes in neutron flux and gamma flux were allowed to run for 25 seconds although most of the transient behavior was gone after 10 to 12 seconds.

The first generation planar sensors were constructed from materials known to be compatible with the fabrication process. The housing and heater substrate were made from alumina. Alumina has desirable characteristics such as in high temperature compatibility and low neutron absorption cross section. Simulations were run to determine the bandwidth of the following sensor configurations:

1) the base sensor that has no protective layer of alumina between the fissile layer and the platinum heater,

2) the sensor has alumina powder filling the gap between the fissile layer and the alumina cap,

3) there is a protective layer of alumina between the fissile material and the platinum heater, but no alumina powder in the gap between the cap and the sensor surface, and

4) the alumina powder is added to case 3 above.

Figures 24 through 27 show frequency response data for the aforementioned sensors. The frequency response graphs were generated in the following manner. After reaching steady state, the sensor was subjected to neutron flux containing random fluctuations around the mean neutron flux level at which steady state was reached. The fluctuations fell within a +/- 3% range of the mean flux. Using MATLAB's '*psd'* command the common practice of performing a Fast Fourier Transform (FFT) on the resulting output current data, and manipulating the data by operations such as averaging, was carried out. Averaging allows for the removal of noise in the resulting power spectral density. The frequency response curves were generated in Excel by converting the power values (P) into decibels by,

$$dB = 20\log_{10}(\sqrt{P}) \tag{10}$$

and plotting on a logarithmic frequency scale. This was the method commonly used for determining the bandwidth of all instruments. Bandwidth here is used to describe the frequency at which the amplitude ratio has fallen to a value of 3 dB below the initial plateau.

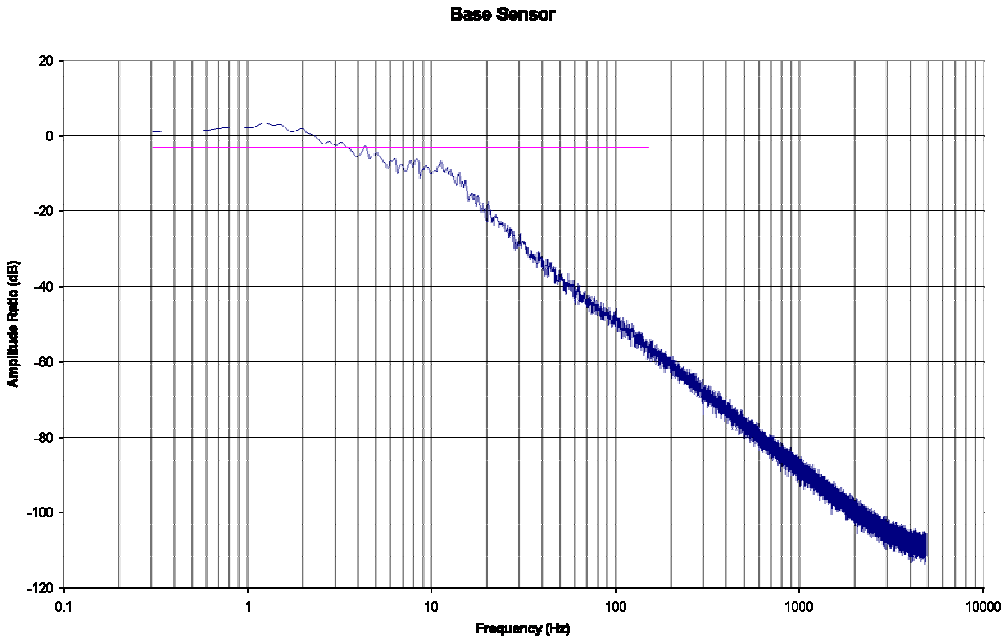

Figure 24: Frequency Response Of The Base Sensor
(Cutoff Frequency of 3 Hz, Sampling Frequency of 10 KHz)

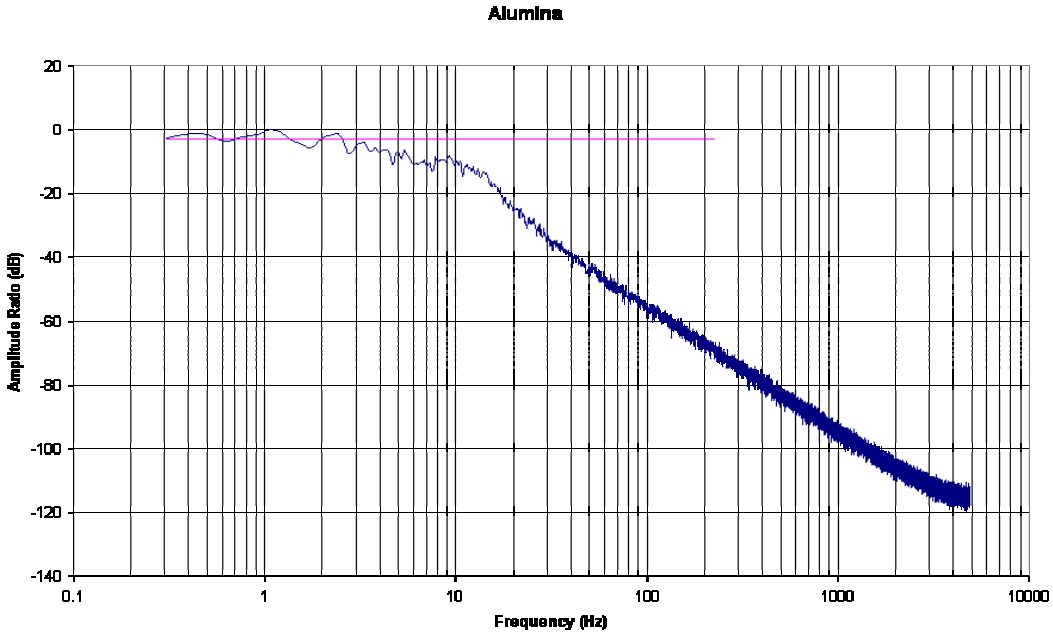

Figure 25: Frequency Response Of The Alumina Sensor
(Cutoff Frequency of 2.5 Hz, Sampling Frequency of 10KHz)

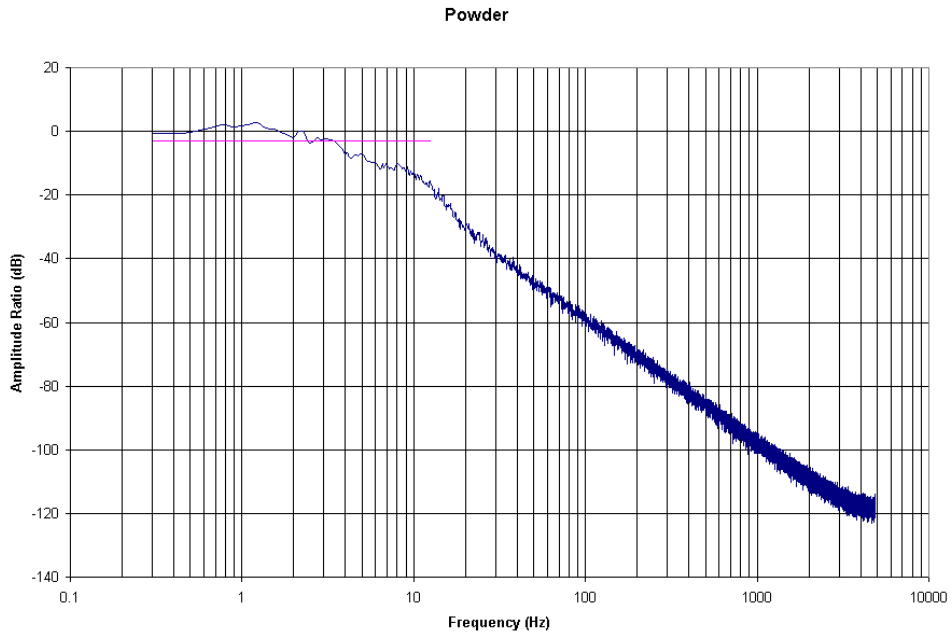

Figure 26: Frequency Response Of The Powder Filled Sensor
(Cutoff Frequency of 3 Hz, Sampling Frequency of 10KHz)

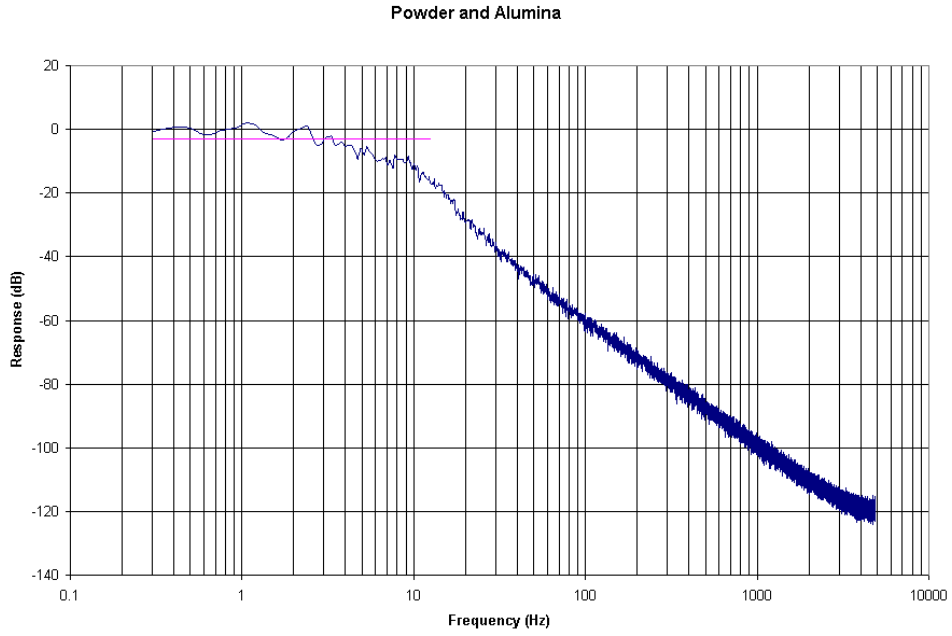

Figure 27: Frequency Response Of The Powder and Alumina Sensor
(Cutoff Frequency of 2.5 Hz, Sampling Frequency of 10KHz)

Previous use of the simulation model indicates that faithful representation of frequency content can be achieved when the sampling frequency is three orders of magnitude higher than the highest frequency of interest. So for faithful data representation at the 1 Hz frequency range a sampling frequency of 1000 samples per second or a time step of 0.001 seconds is required. Until the faster sensors were developed the sampling frequency used was 10,000 samples per second, which preserves frequency data up to 10Hz. The corresponding time step for this sampling frequency is 0.0001 seconds and this value was used for the first generation planar sensor simulations. This issue will become more important as the results are discussed further.

Referring to Figures 24 through 27, we are able to evaluate the characteristics of the various configurations. The addition of alumina layers and alumina powder to the base sensor does not have a major impact on sensor performance. Recall that the alumina layer is placed between the platinum heater and the fissile material to serve as a fission fragment barrier to protect the integrity of the heater. The alumina powder is present to increase the heat transfer across the 'gap' between the fissile layer and the underside of the top disk. Speculative values for the sensor cutoff frequency are presented but it should be clear that these values approximate the actual value. The goal is not to specify the exact effect of the addition of these materials but rather to confirm that deleterious changes to sensor performance are not induced by the changes in sensor configuration.

As noted earlier, the model does not encompass radiant heat transfer. The powdered alumina is assigned an estimated thermal conductivity of $1\ \frac{W}{m-K}$ and the evacuated gap is assigned an estimated thermal conductivity of $0.001\frac{W}{m-K}$. Thus we have compared the effect of three orders of magnitude difference in the thermal conductivity of the area in question. It is clear that the heat transfer due to convection through the bottom of the sensor dominates all other modes of heat transfer.

Figures 28 and 29 show the temperature profile of the alumina sensor after reaching steady state. The figures show that the profile follows the shape that one would

intuitively expect. First, looking at Figure 28, it is clear that the coolest part of the sensor is its top center region. This is reasonable because of the low conductivity of the evacuated area and the comparatively low conductivity of the alumina ring and top disk. It is clear that heat is being conducted up the alumina ring, as there is a definite temperature change along the axial node two from radial nodes one to 30. This figure also shows a decrease in temperature along the axial nodes 11 and 12 as viewed from radial nodes 1 to 30. The center of the sensor is the hottest area, which is reasonable given the nature of the available pathways for heat transfer. In addition, a temperature drop is clear at about node 26 that represents the end of the uranium oxide and platinum heater and the beginning of the alumina ring. Figure 29 shows the same profile from a different angle. Finally, from Figure 30, we see that the absolute hottest axial positions of the sensor are in fact the axial sets of nodes that contain the platinum and uranium.

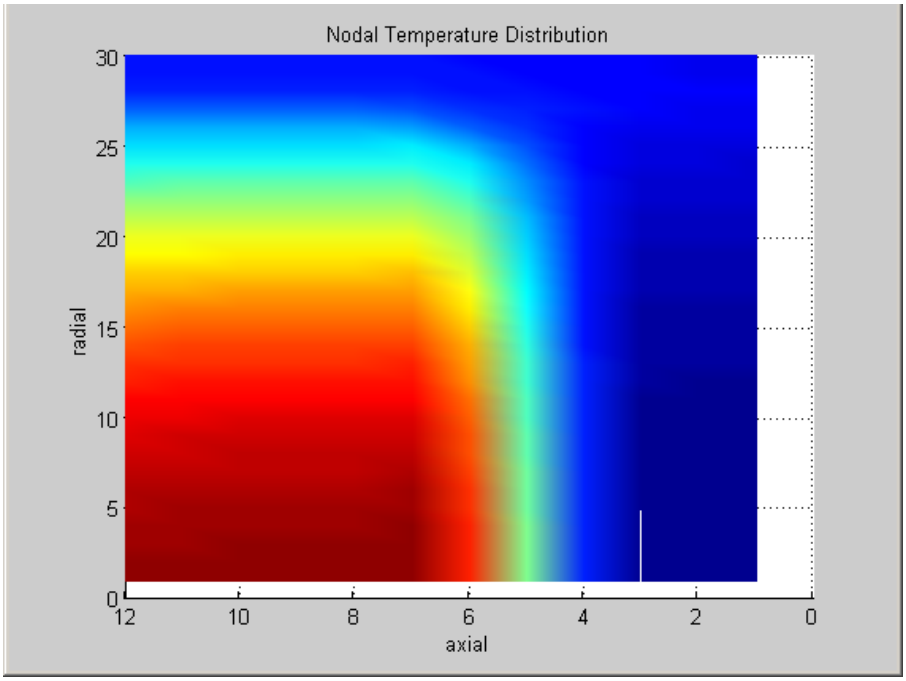

Figure 28: Sensor Temperature Profile (Top View)

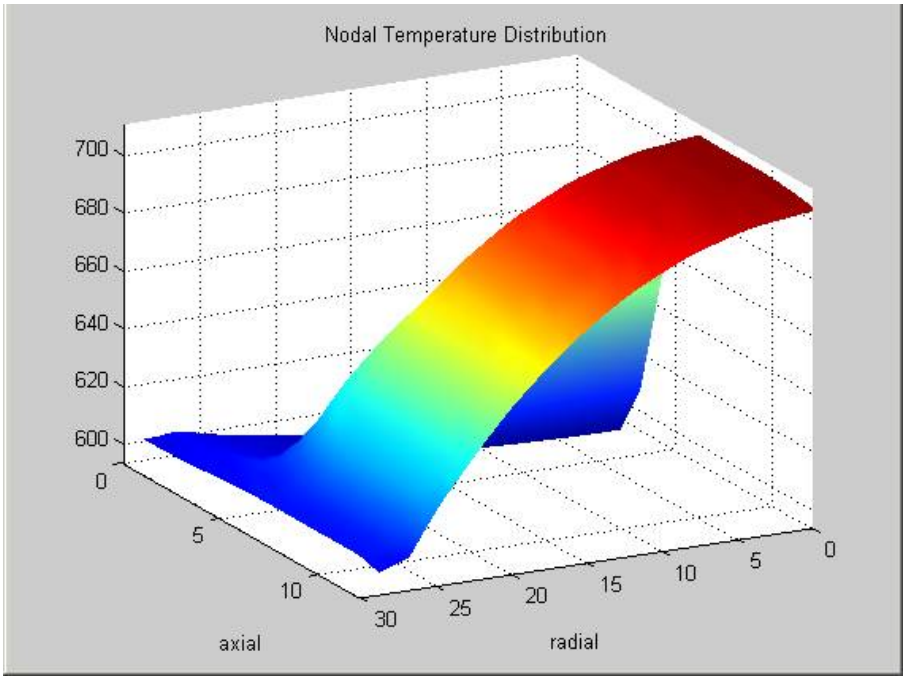

Figure 29: Sensor Temperature Profile (Isometric View)

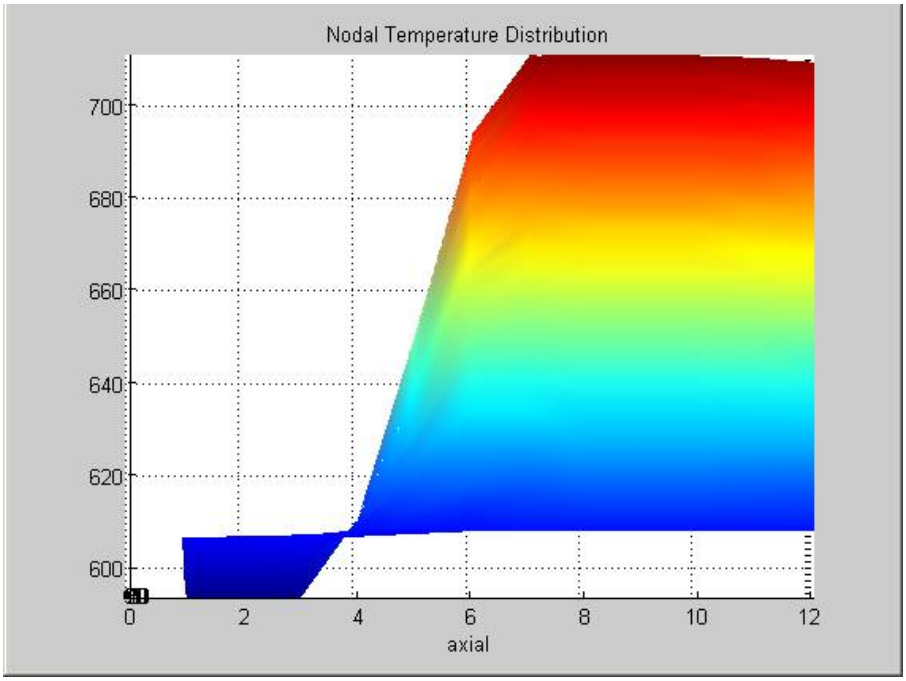

Figure 30: Sensor Temperature Profile (Vertical Cross Section)

Before considering possible sensor designs, we first consider the predicted sensitivity of the base sensor. This will be useful when comparing the sensitivities predicted for subsequent sensors. Sensor design requires a balance of trade-offs. As

noted earlier, faster response will result in decreased sensitivity, and vice versa. Figure 31 shows the response of three different sensors to step changes of –5%, -20%, -50%, and +10% in neutron flux. The base sensor sensitivity is reported as deposited electrical power as a function of neutron flux. The sensitivity for the base sensor is,

$$2.901 \times 10^{-13} \ \frac{\text{Watts}}{\left(\frac{\text{n}}{\text{cm}^2\,\text{sec}}\right)}$$

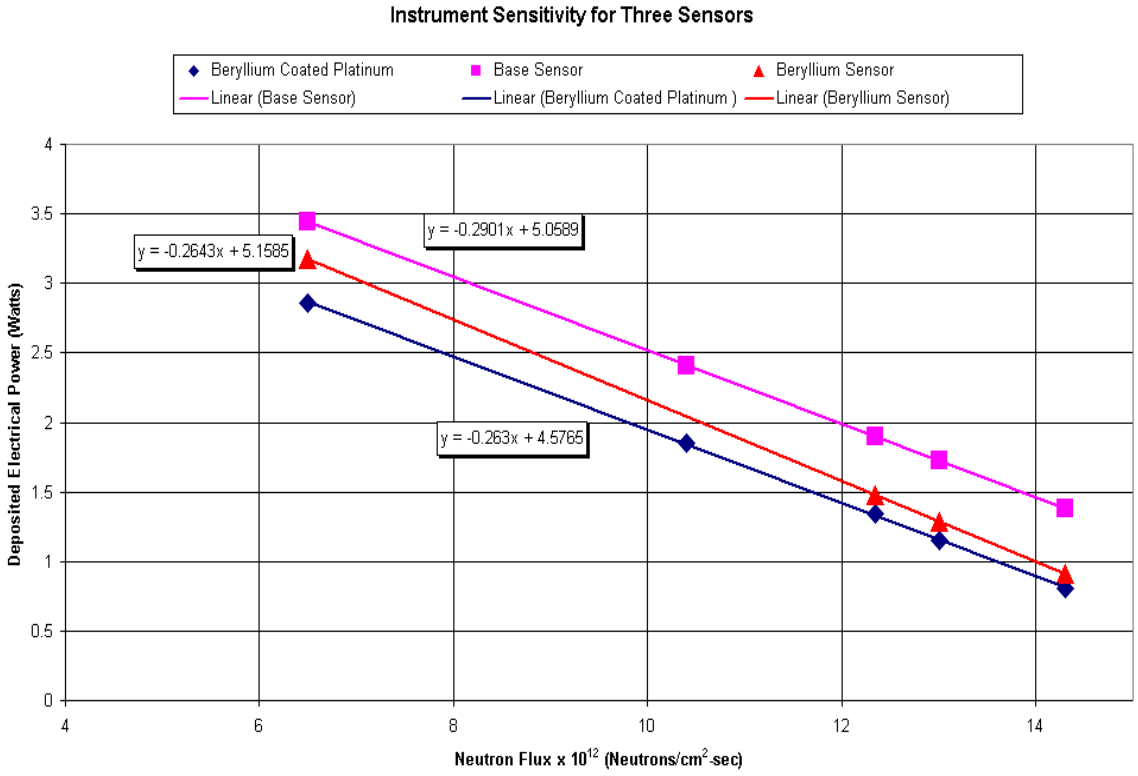

Figure 31: Sensitivity Data For Various Sensors

Attempts to design a faster sensor began with a search for substitutes for alumina. If a material with similar properties and increased thermal conductivity could be identified, a sensor utilizing this material would exhibit faster response. Beryllium oxide (BeO) is a material used for the fabrication of the cylindrical sensor as a conduction path. Cylindrical sensor performance is enhanced when heat flow is directed axially. Thus the cylindrical cores are "painted" with a BeO coating and surrounded with insulation to facilitate heat flow. Beryllium oxide has superior heat transfer properties and would be a

suitable sensor housing material. Sensor fabrication using BeO is not an issue. Simulation runs now were focused on sensors making use of this material. A series of studies were conducted using a thermal conductivity for the housing of the sensor of 55 $\frac{W}{m-K}$ instead of 15 $\frac{W}{m-K}$ for alumina. The 55 $\frac{W}{m-K}$ value is conservative as the literature consulted reports this to be the value of thermal conductivity at 500 degrees C and we are operating below this temperature where the conductivity will be higher. Again, the exact values of conductivity are not as important as the performance of the sensor based on the *difference* in the values used. Values such as density and specific heat and gamma attenuation also play a role and thus it is important to identify material properties as closely as possible. The beryllium sensor simulations were run using the above value of thermal conductivity for solid beryllium and a value of 5 $\frac{W}{m-K}$ for beryllium powder packed into the 'gap' area.

Figure 32 shows the frequency response generated from white noise superimposed on neutron flux for the beryllium sensor. Clearly the increased thermal conductivity of the sensor housing leads to a substantial increase in the speed of this sensor. The sensor with superior heat transfer is faster because changes in the temperature profile occur sooner. Consider an increase in neutron flux. The electrical power deposition must be reduced to maintain a constant temperature profile. The energy deposited electrically must be dissipated. A sensor having good heat transfer properties enhances energy transport.

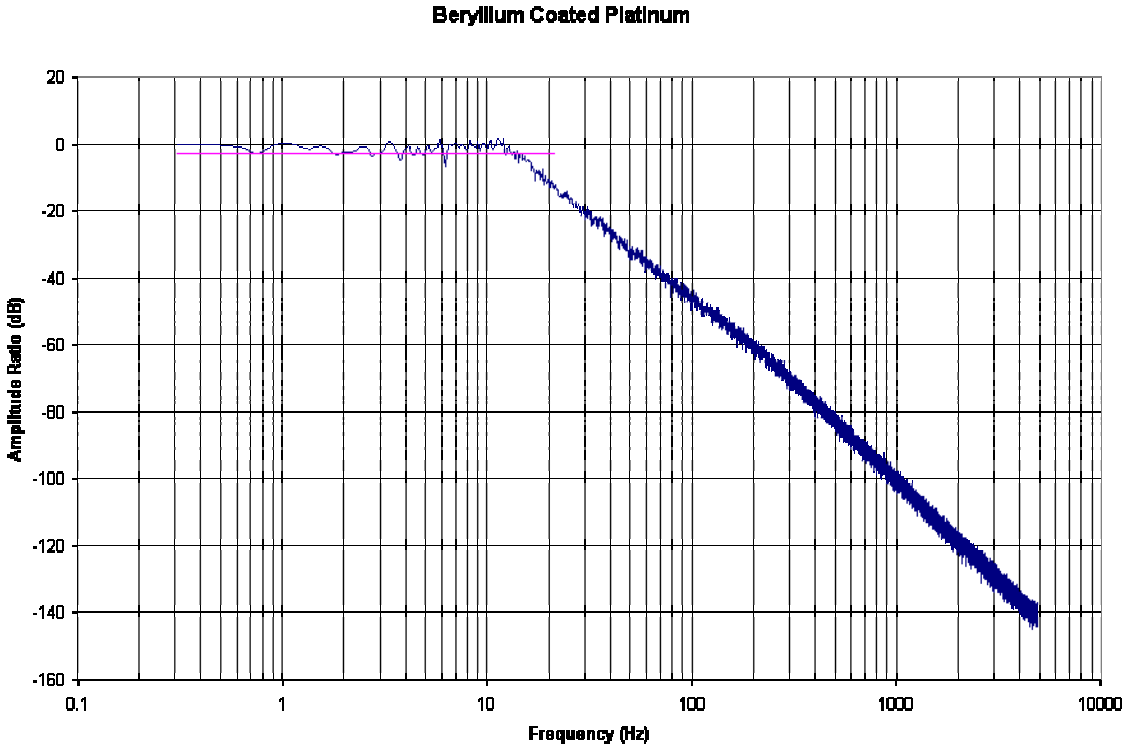

Figure 32: Beryllium Sensor Frequency Response
(Cutoff Frequency of 10 Hz, Sampling Frequency of 10 Khz)

This represents a significant result because it requires only a material change. All of the fabrication techniques developed to this point can still be utilized, and the sensor could be constructed relatively quickly. Figure 31 illustrates sensitivity with respect to deposited electrical power as a function of neutron flux. The sensitivity value here is reported as:

$$2.64\text{x}10^{-13}\ \frac{\text{Watts}}{\left(\frac{\text{n}}{\text{cm}^2\ \text{sec}}\right)}.$$

We see that this sensor is slightly less sensitive than the base sensor.

The next step in maximizing the thermal conductivity of the sensor is consideration of the use of a metallic housing. The sensor is intended to operate in a high-pressure, high temperature, wet environment. Ceramics are well suited for this application and are the reason they have been the major focus of attention in this study.

The next simulation studies the performance of a metallic housing that has been coated with a thin layer of beryllium oxide. Obviously this thin layer is essential to provide electrical insulation between the platinum heater and the platinum housing. The code was modified to include platinum as the main housing material with all of the housing material coated with about 20 microns of beryllium. This thickness theoretically provides sufficient electrical insulation and is a feasible deposition thickness for the screen-printing operation. Extensive simulation effort has been spent on this sensor because it has exhibited the fastest response times. This sensor simulation was also carried out using a value of thermal conductivity of 5 $\frac{W}{m-K}$ for beryllium powder packed into the 'gap' area of the sensor. Figure 33 shows the frequency response for the sensor now referred to as the beryllium coated platinum sensor (BCPS). The increase in thermal conductivity from 55 $\frac{W}{m-K}$ to 72 $\frac{W}{m-K}$ from beryllium oxide to platinum results in a slight increase in sensor bandwidth as comparison of Figures 32 and 33 confirm.

Neutron sensitivity and instrument linearity were determined using the results from several different step changes in neutron flux. Reference is again made to Figure 4.8 as the responses of three sensors to step changes of neutron flux are shown. Here the sensitivity is:

$$2.63 \times 10^{-14} \frac{\text{Watts}}{\left(\frac{n}{cm^2\,sec}\right)}.$$

We see that this sensor is slightly less sensitive than the others in the figure. Thus the trend of sacrificing speed for sensitivity is confirmed. The fastest sensor is also the least sensitive, Table 3 summarizes the speed and sensitivity data for the three sensors discussed.

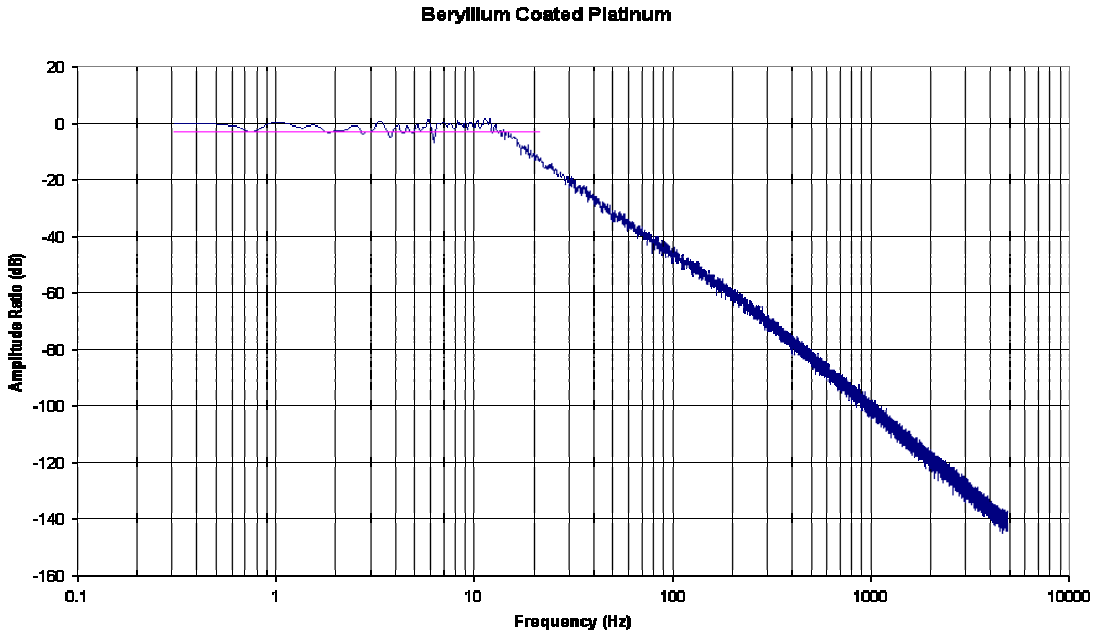

Figure 33: BCPS Frequency Response
(Cutoff Frequency of 10.5 Hz, Sampling Frequency of 10KHz)

Sensor	Bandwidth (Hz)	Sensitivity (Watts/(n/cm^2-sec))
Base Sensor	3	2.901×10^{-13}
Beryllium Sensor	10	2.643×10^{-13}
Beryllium Coated Platinum Sensor	10.5-11	2.630×10^{-13}

Table 3: Bandwidth and Sensitivity Data

As is the case with all measurement devices, the instrument may be sensitive to inputs other than the process variable it is intended to measure. The numerical model uses a gamma interaction module to calculate gamma heating in the sensor. Results suggest that the planar sensor will be largely insensitive to gamma radiation.

Verification of this expected response required calculations to validate the output of the gamma power deposition module. Using the respective volumes and linear attenuation coefficients for 1 Mev gamma rays found in Table 4, the value of gamma power deposition is calculated. Gamma flux intensity is 4.843×10^{18} and we use a conversion of 1.6×10^{-13} joules/Mev. The materials are listed in Table 4 along with their

dimensions other relevant data. The numbers match exactly the output of the code and we see that the fission power deposition is approximately 5 watts while the gamma power deposition is approximately 0.022 watts. Thus the sensor is orders of magnitude more sensitive to neutrons than gammas. The beryllium coated platinum sensor is more sensitive to gamma heating due to the increased volume of platinum. A similar calculation showed that the gamma power deposition in the beryllium coated platinum sensor is 0.06 watts. This is sufficiently small to conclude that the device is relatively insensitive to gamma heating.

Alumina			Platinum			Gap		
Disk			height	0.000	m	height	0.00098	m
Radius	0.0065	m	length	0.1101	m	radius	0.0055	m
Thickness	0.0005	m	x sect	0.0004	m	Volume	7.02E-08	m^3
Volume	6.637E-08	m^3	Volume	4.02E-10	m^3			
Ring			Uranium					
Inside Radius	0.0055	m	height	1.00E-05	m	Linear Attenuation		
Outside Radius	0.0065	m	radius	0.0055	m	Alumina	9.88E-02	m^{-1}
Height	0.001	m	volume disk	9.50E-10	m^3	Uranium	7.57E-01	m^{-1}
Volume	3.77E-08	m^3	volume gaps	4.02E-10	m^3	Platinum	1.47	m^{-1}
Total Volume	1.65E-07	m^3	Volume	1.29E-08	m^3	Gap	3.15E-02	m^{-1}

qdot alumina	0.01266	watts
qdot platinum	0.00046	watts
qdot uranium	0.00756	watts
qdot gap	0.0017	watts
Total qdot	0.02240	watts

Table 4: Gamma Power Deposition Validation

As discussed earlier, the need for temperature compensation was recognized upon testing the first generation cylindrical sensors. Recall that coolant temperature changes will appear as power deposition changes in the sensor due to assumptions made in our initial energy balance. The behavior of the sensor in the presence of changing coolant temperatures was analyzed for three different kinds of coolant temperature change.

Figure 34 shows the frequency response of the sensor for randomly fluctuating coolant temperature changes. This analysis indicates there are no resonant frequencies that lead to disruptive behavior of the sensor. Observing sensor response to step changes

in coolant temperature provides additional information. Figure 35 shows the response of the sensor to a three percent increase in coolant temperature. Analysis of the early time steps shows the separation that exists in node temperatures, as well as differences in the speed with which each node reaches its new steady state temperature. This difference is expected as the edge node is more quickly influenced by changes in coolant temperature. The important result is that each node increases by exactly the same amount as the magnitude of the step change in coolant temperature. Table 5 shows the numerical data to illustrate this point. The results show that the individual nodes re-establish the set-point temperature differential in about eight seconds and they do so by both changing in temperature by the same amount. Further, the magnitude of this shared temperature change is essentially the same as the coolant temperature change.

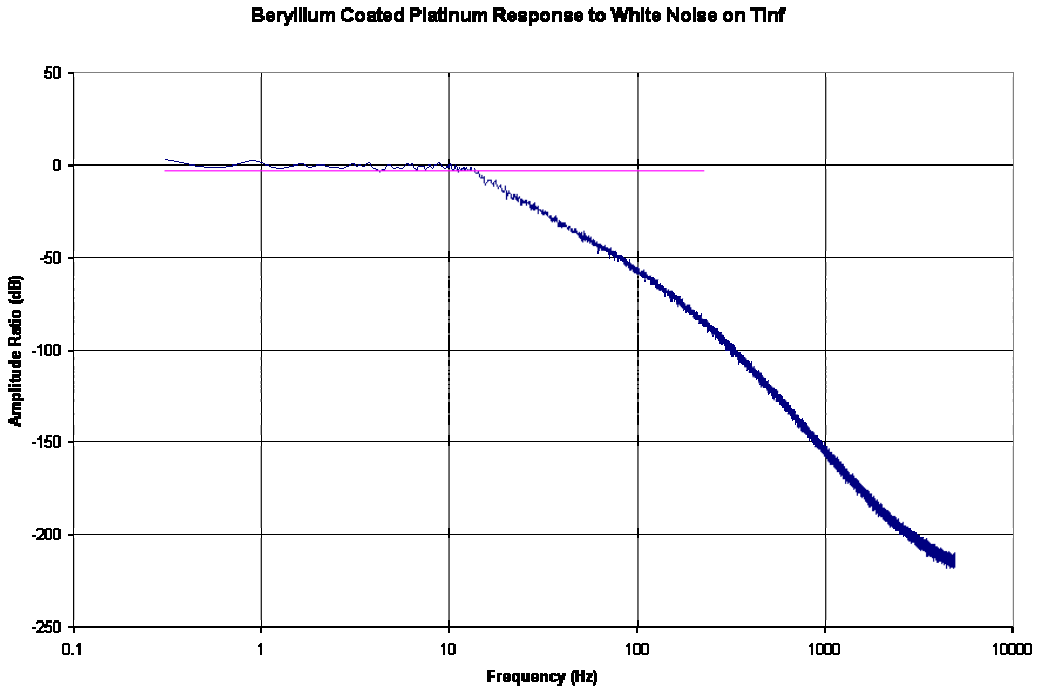

Figure 34: Frequency Response to Random Fluctuations in Coolant Temperature
(Sampling Frequency of 10KHz)

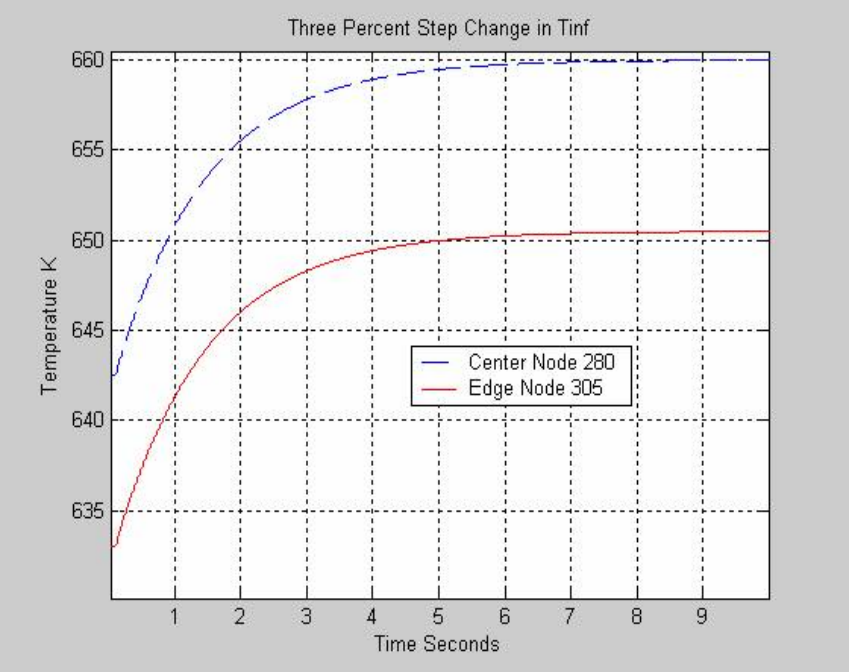

Figure 35: Response Of The Sensor To A Step Change in Coolant Temperature

Temperature	Units	Initial	Final	Difference ^{o}K
Tinf	^{o}K	583	600.49	17.49
Node 280 (Center)	^{o}K	642.5116	659.9938	17.4822
Node 305 (Edge)	^{o}K	633.0116	650.4938	17.4822
Sensor Current	Amps	0.2326	0.2344	

Table 5: Nodal Data for Response to 3% Step Increase in Tinf

Also included in Table 5 is the sensor current to show that a compensating method is necessary to avoid being misled by coolant temperature changes. It is clear that the sensor itself supplies all of the information needed to establish the compensation methodology. As long as the temperature at one node is known, changes in coolant temperature can be tracked.

As a final illustration, consider Figure 36 in which a slow ramp in coolant temperature is introduced where temperature increases one percent every 20 seconds. Careful analysis of the response in the early time steps shows that the change in node temperatures, while not instantaneous, parallels coolant temperature changes after approximately two seconds.

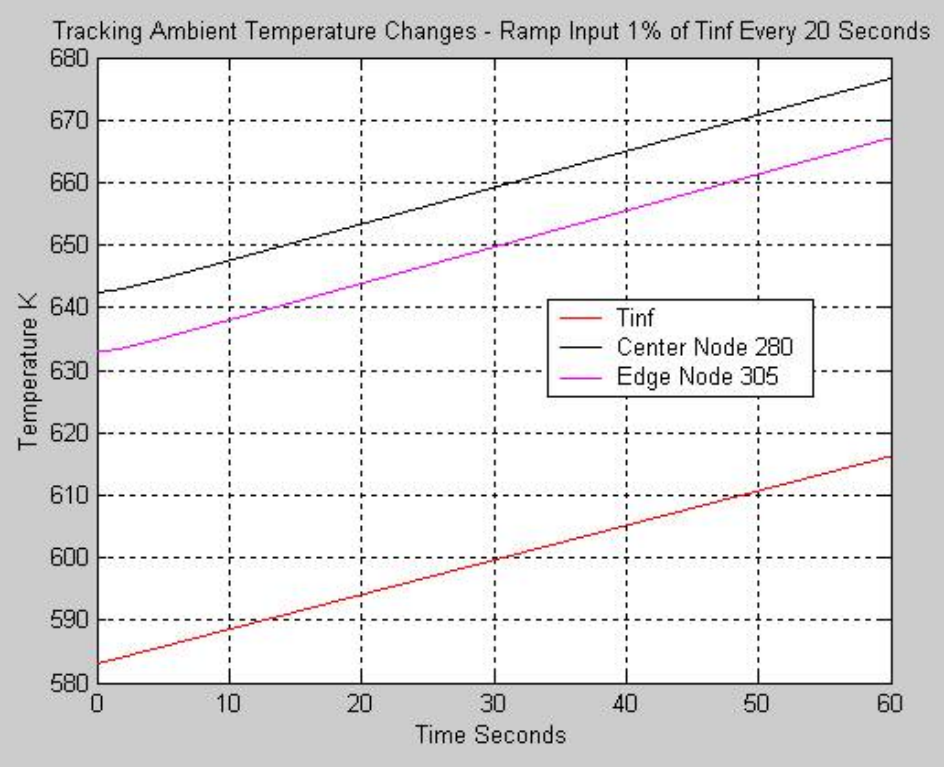

Figure 36: Sensor Response To A Slow Ramp Change In Coolant Temperature

A more detailed analysis the beryllium coated platinum sensor (BCPS) is desirable as it has been identified as the fastest sensor. Previous analyses showed sampling frequencies three orders of magnitude beyond frequencies of interest were required to have confidence in the results. A cutoff frequency of greater than 10 Hz requires simulation at a finer time step to assure the data are valid. A time step of 0.0001 seconds provides valid frequency information up to 10 Hz. We now examine the results of a simulation run with a time step of 0.00005 seconds. This shorter time step provides valid results up to 20 Hz. We again run for 100 seconds of simulation time to come to steady state and another 50 seconds of simulation time to impose the random fluctuations on the neutron flux. The resulting data were processed as before to generate the frequency response shown in Figure 34. Analysis of this figure and comparison with Figure 33 highlights important information. Figure 33 shows the cutoff frequency to be slightly above 10 Hz while Figure 37 shows the cutoff frequency to be 11 Hz. Other than this and the lower levels of noise seen in Figure 37, the results are similar. They illustrate an important feature of the simulation model and the improvement in computational

efficiency that has been implemented. This simulation would have been almost impossible to run with the code in its original form as it takes about 170 hours to complete the three million time steps necessary to produce the results.

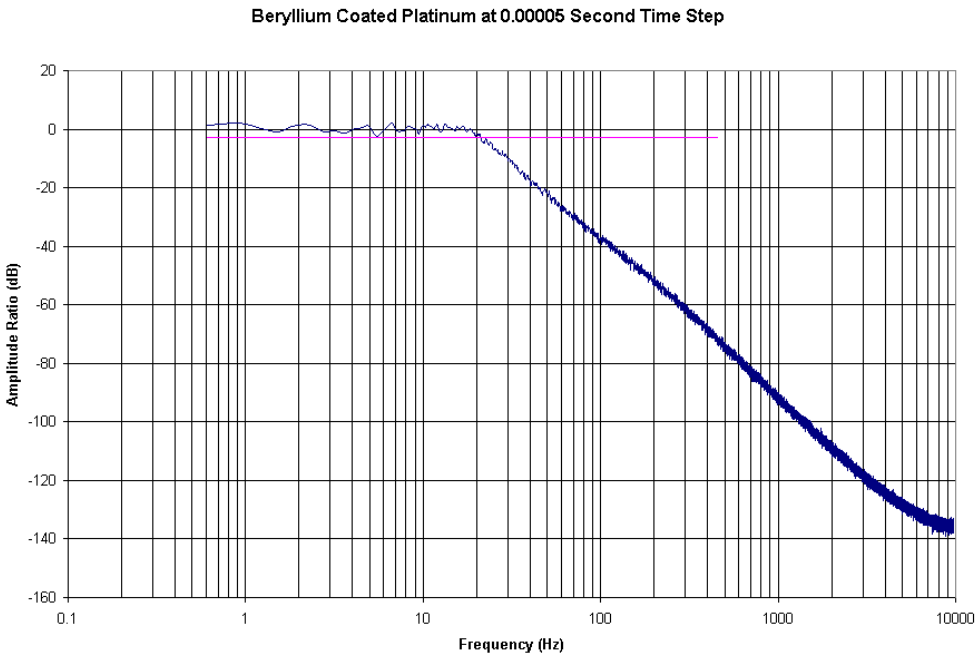

Figure 37: Frequency Response Of The BCPS
(Cutoff Frequency of 11 Hz, Sampling Frequency of 20 KHz)

The above simulation is based on the nodal layout shown in Figure 22. In order to investigate if the addition of another layer of nodes into the thermocouple-heater interface retards the transmission of heat significantly or not, the code was modified to reflect the nodal layout shown in Figure 38, which adds another row of nodes between the heater and the thermocouples. Actual material dimensions were not changed, but the height of the fissile layer was divided in two and the set of nodes was recast. The steady state and white noise neutron fluctuation cases were run again and Figure 39 illustrates the resulting frequency response, and shows a small change in sensor response time.

Nearly all of the simulations were run with the delta I controller. Numerical simulations using the PID controller developed for the sensor were also performed. Tuning of the PID controller was begun by increasing proportional control until continuous oscillations were observed. After determining this ultimate proportional

value, various PID parameters were adjusted until the controller showed minimal overshoot and steady state error.

Integrator windup was a significant problem with this controller and required imposition of a limit, or anti-windup condition. Because the integral signal is a function of the total history of previous errors it is obvious why this limit needs to be established.

The sensor simulation was run again to attainment of steady state and subjected to random fluctuations in neutron flux. The resulting frequency response is shown in Figure 40. We see that the controller has not affected the cutoff frequency of the sensor but this does not imply that the performance of the sensor channel has not been enhanced by the new control algorithm. Figure 40 shows that the controller is opposing the steep roll-off found in Figure 33.

Further insight into the performance of the different controllers can be obtained by observing each controller's ability to recover after being subjected to a step change in neutron flux. First the sensor was subjected to a five percent step decrease in neutron flux. Figure 41 compares the responses of the sensor channel for the PID and Delta I controllers. Settling time here refers to the approximate time that the steady state value is reached. From Figure 41 we see that the PID controlled sensor achieves an essentially steady value after 0.09 seconds. The Delta I controller exhibits overshoot and ringing and shows a settling time of approximately 0.15 seconds. Figure 42 is provided to allow the controllers to be compared to classical proportional control. Figure 42 shows that the proportional controller takes almost a full second to achieve a steady value. In addition, the sensor exhibits its response by showing an increase in steady state error. These results match results observed in early testing of the proportionally controlled sensors. We will later show that this control scheme results in a reduction in the steady state error when the neutron flux increases.

A second round of tests was carried out to observe the response times of the sensor when subjected to an increasing neutron flux. The sensor is expected to be slower

to respond to increases in neutron flux because the applied electrical power at the time of neutron flux change must be dissipated before establishing a new steady value. These responses can bee seen in Figures 43 and 44. Here the Delta I controller settles in approximately 0.22 seconds, the PID controller settles in approximately 0.15 seconds, and the proportional controller settles in approximately 0.9 seconds. As expected the sensor is slower to respond to increases in neutron flux. Table 6 details the settling time for each controller at each step change value.

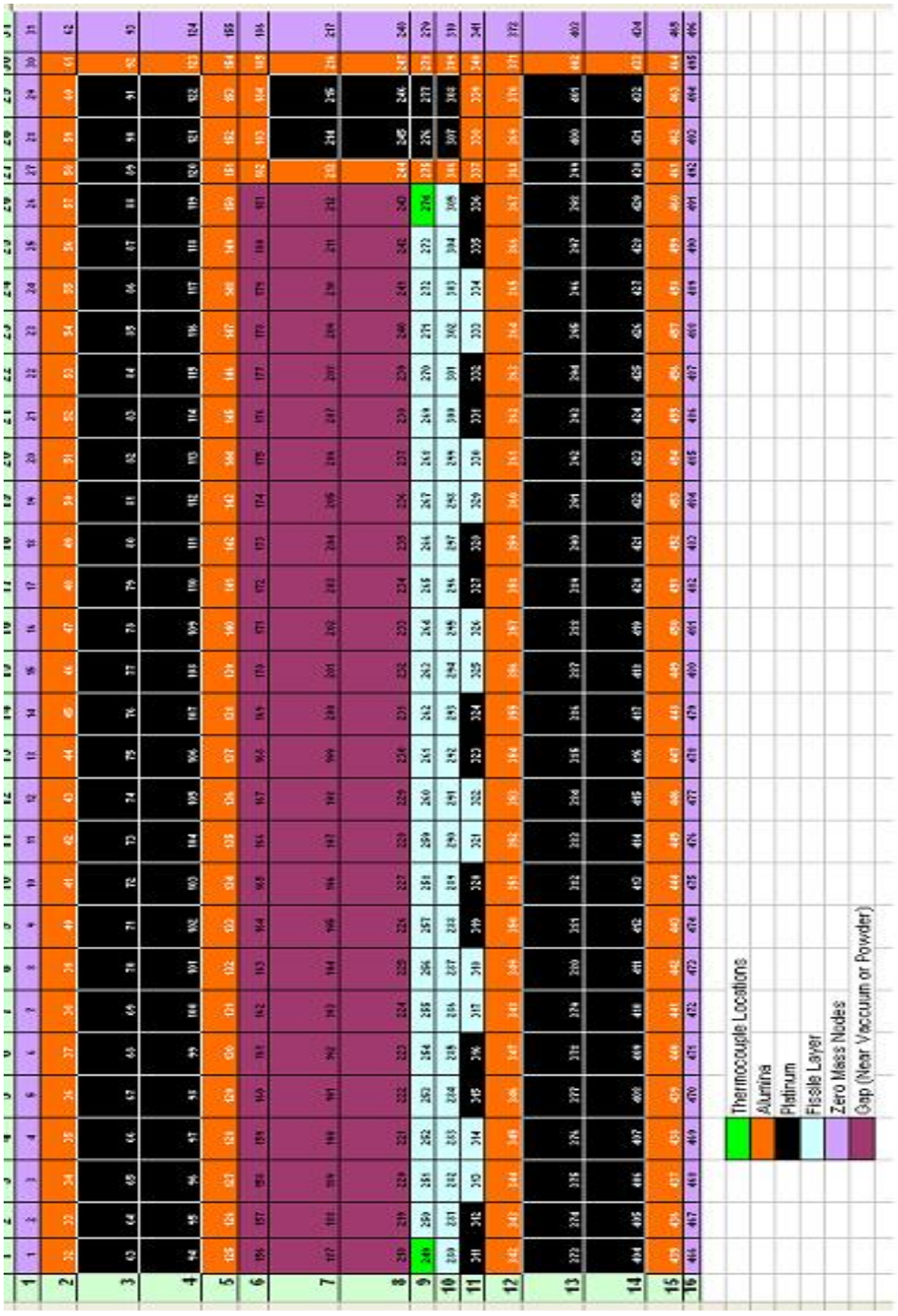

Figure 38: Coated Platinum Sensor Nodal Layout With An Added Layer Of Nodes At The Thermocouple Locations

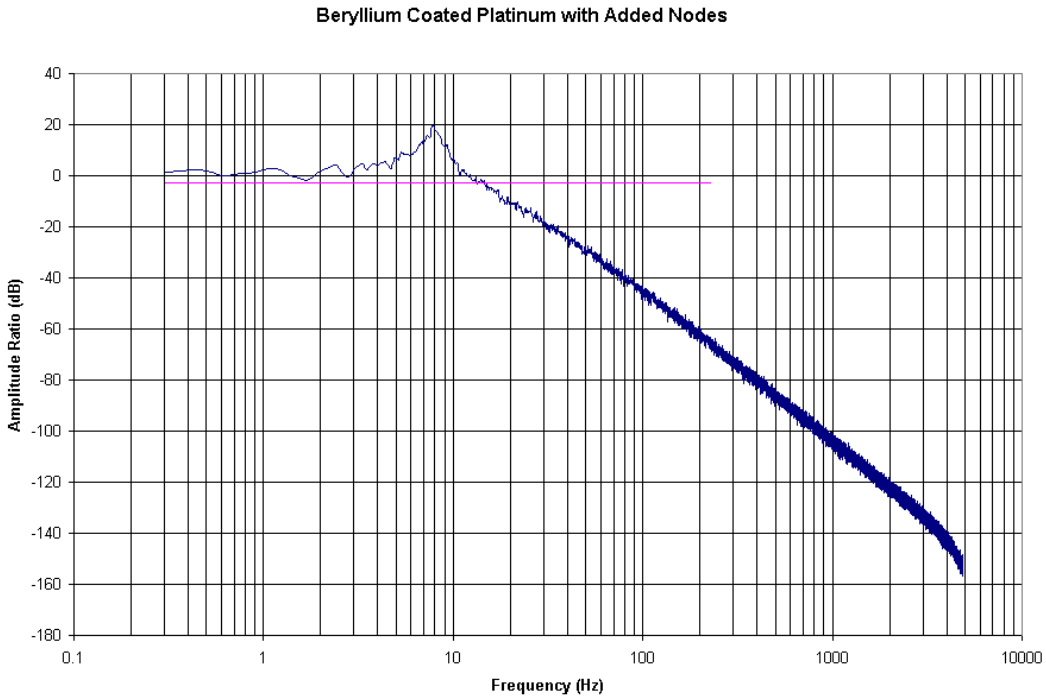

Figure 39: Frequency Response Of The BCPS With The Modified Nodal Definitions
(Sampling Frequency of 10 KHz)

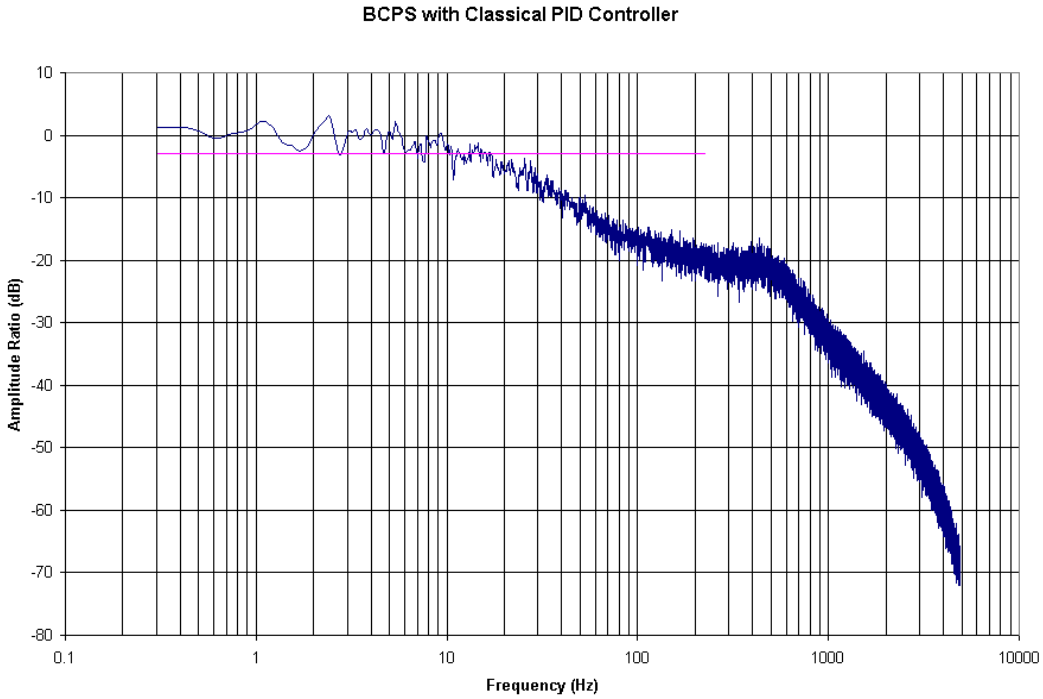

Figure 40: Frequency Response Of The BCPS With PID Control
(Sampling Frequency of 10 KHz)

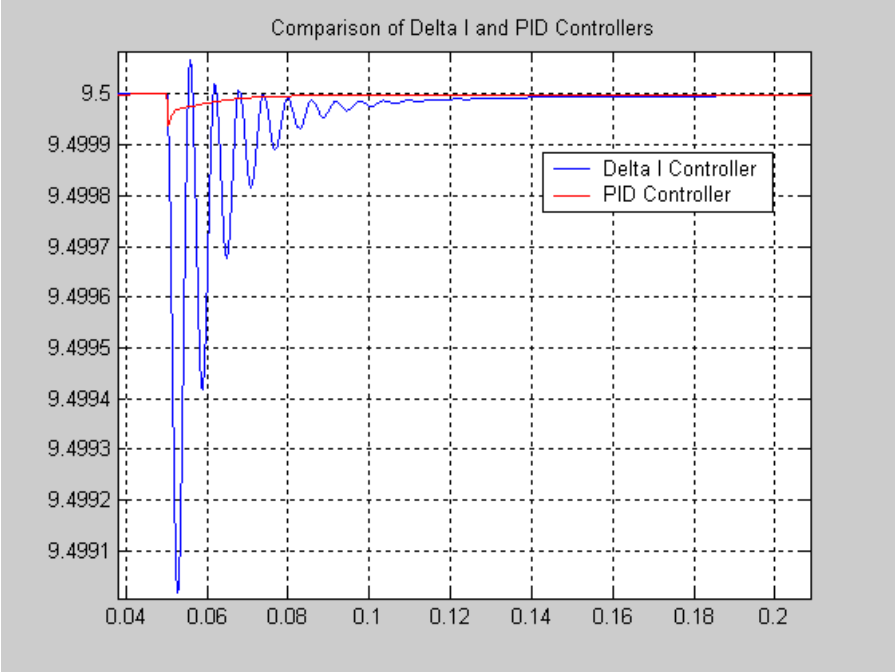

Figure 41: PID and Delta I Controller Comparison
(5% Step Decrease in Neutron Flux)

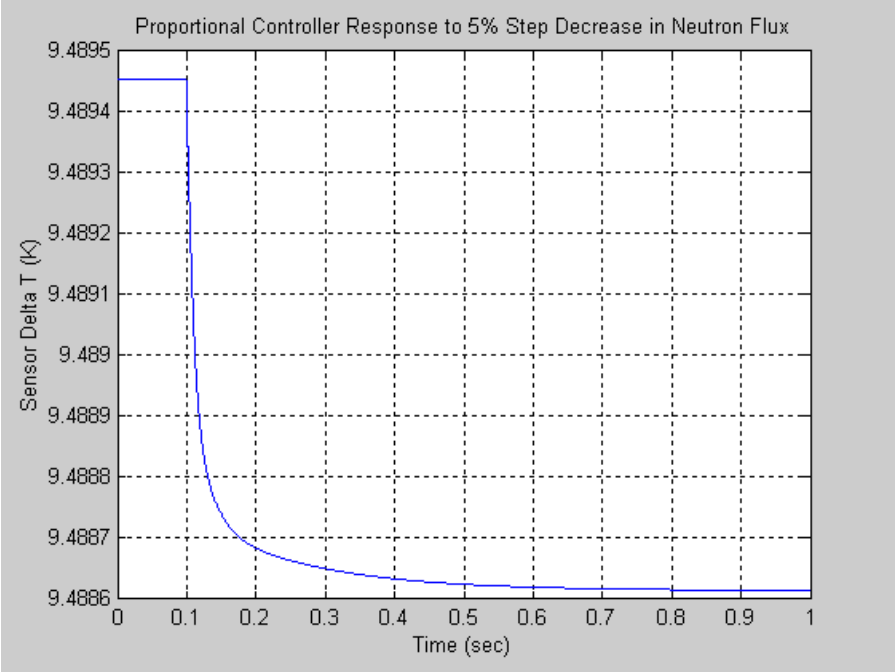

Figure 42: Response Of A Proportional Controller
To A 5% Step Decrease In Neutron Flux

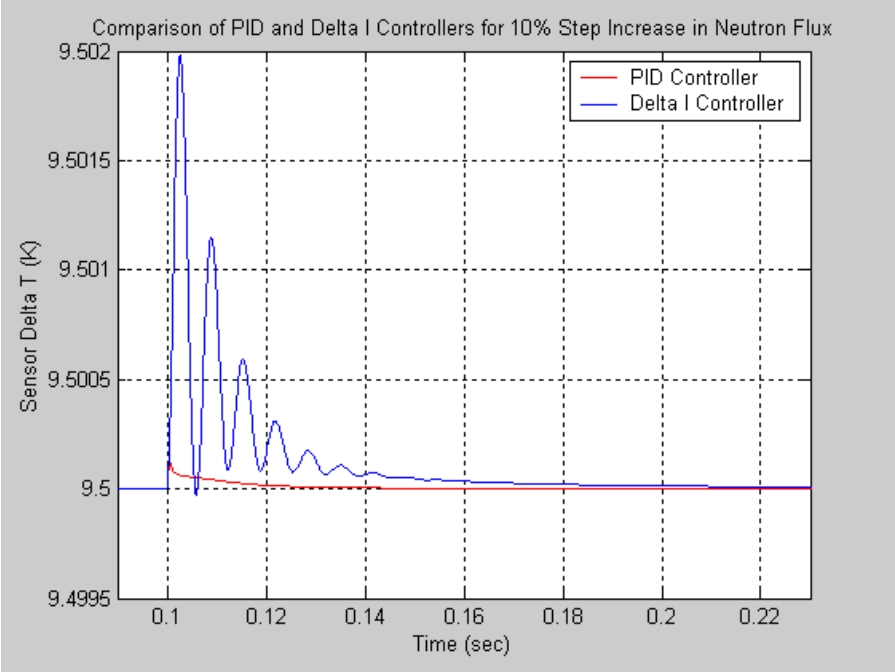

Figure 43: PID and Delta I Controller Comparison
(10% Step Increase in Neutron Flux)

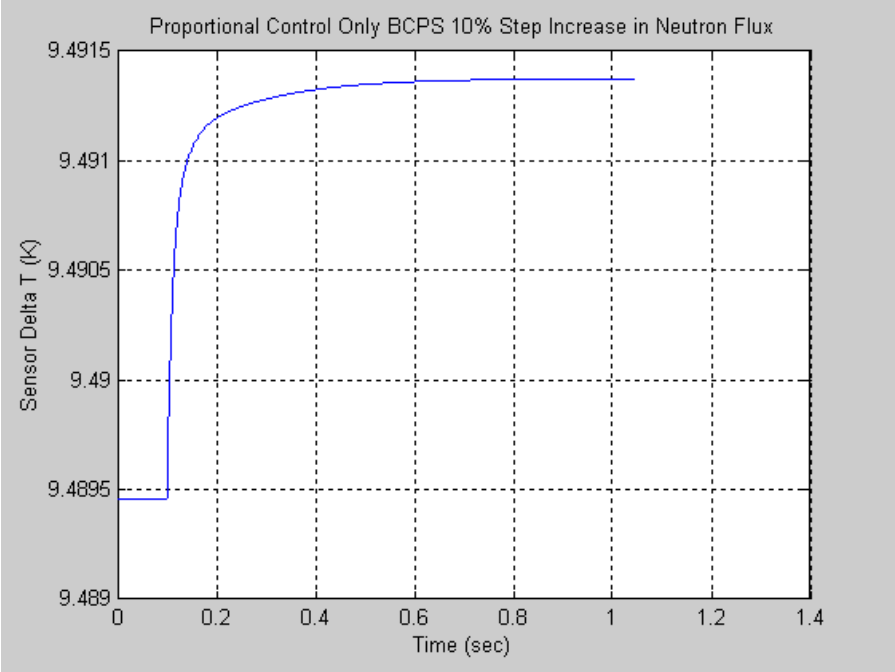

Figure 44: Response Of A Proportional Controller To A 10% Step Increase in Neutron Flux

Controller Type	Settling Time 5% Step Decrease (Sec)	Figure	Settling Time 10% Step Increase (Sec)	Figure
Delta I	0.15	4.18	0.22	4.21
PID	0.09	4.18	0.15	4.21
Proportional	0.9	4.19	0.9	4.22

Table 6: Responses to Step Changes in Neutron Flux for Various Control Schemes

In summary, the simulations have shown that the beryllium coated platinum sensor (BCPS) is the fastest sensor. The modified numerical model predicts linear sensor sensitivity to neutron flux and insensitivity to gamma heating. The model predicts a bandwidth of approximately 11 Hz and the ability to discern ambient or coolant temperature changes from changes in neutron flux. These predictions make this sensor a promising candidate for future use in reactors in the nuclear power industry.

2.5 SENSOR FABRICATION

The construction of the in core sensors has been a much more challenging problem than initially anticipated. The requirements for small size, durability, and high temperature compatibility make for a challenging combination. A number of sensors have been produced (of both planar and cylindrical geometry), but production difficulties with the cylindrical sensor continue to make the process a slow one. The planar sensors have proved to be easier to produce, and the amount of scrap produced is significantly reduced versus the cylindrical sensors.

The cylindrical design is shown in Figure 45. It requires production of ceramic cores ~0.7mm dia. x 12.0mm long containing ^{235}U. We chose UO_2 as the chemical form of uranium for several reasons. The most common oxide U_3O_8 is volatile in air at high temperatures and cannot be sintered to form a coherent structure. However, UO_2 rapidly oxidizes to U_3O_8 when heated in air, so UO_2 has to be fired in oxygen free environments. Firings up to about 1400°C were done in an atmosphere of flowing forming gas (5% H_2 and 95% N_2) in a tube furnace. Firing at higher temperature (up to 1750°C) was done in a vacuum furnace.

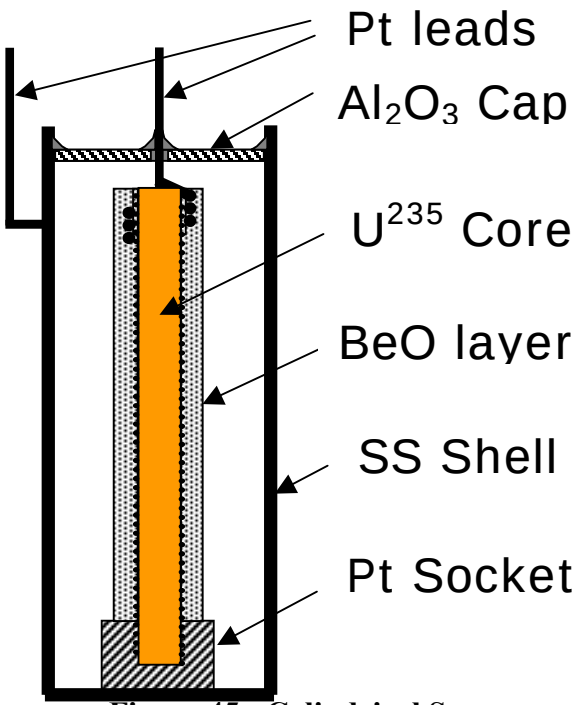

Figure 45: Cylindrical Sensor

The UF (UO_2, Feldspar) sensor bodies consist of only UO_2 and feldspar. These bodies produced smooth crack free surfaces when fired at 1325°C in forming gas as shown in Figure 46 (upper). The interior of the body was also free of cracks (Figure 46, lower). The bright areas in lower Figure 46 consist of an intimate mixture of rounded UO_2 grains in a matrix of feldspar glass. Energy dispersive x-ray analysis, confirmed this interpretation since x-ray fluorescence lines characteristic of both UO_2 (U, O) and feldspar (Al, Si, K, O) were observed in the bright regions. The large dark spots are pockets of feldspar glass. The glass apparently had a small amount of UO_2 dissolved in it. The UF sensor bodies are considerably stronger than other bodies previously prepared and tested. They do not contain cracks and porosity is limited to about 12% of the total volume.

Cylindrical rods of ceramic materials are usually made by extrusion, and this method was adopted for this project. For the cylindrical sensor, the ceramic core had to be a cylindrical rod with finished dimensions of ~0.7mm diameter and 12.0mm long. This is not an unusual size for extrusion methods. However the small amount of $^{235}UO_2$ material available (~2.0 grams) required that a special miniature extrusion apparatus be built. The device is shown schematically in Figure 47.

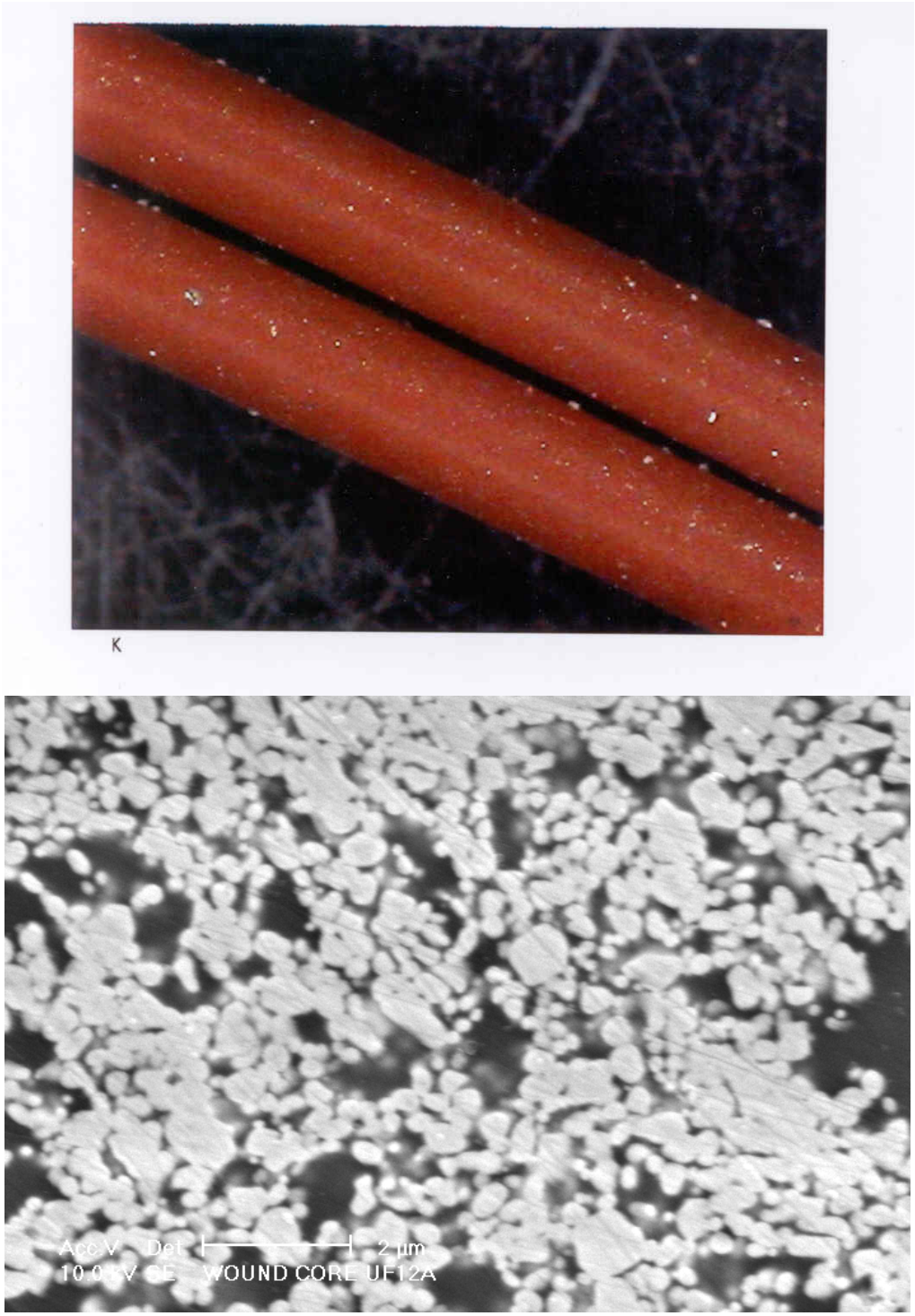

Figure 46: Sintered Sensor Core Materials Under Magnification

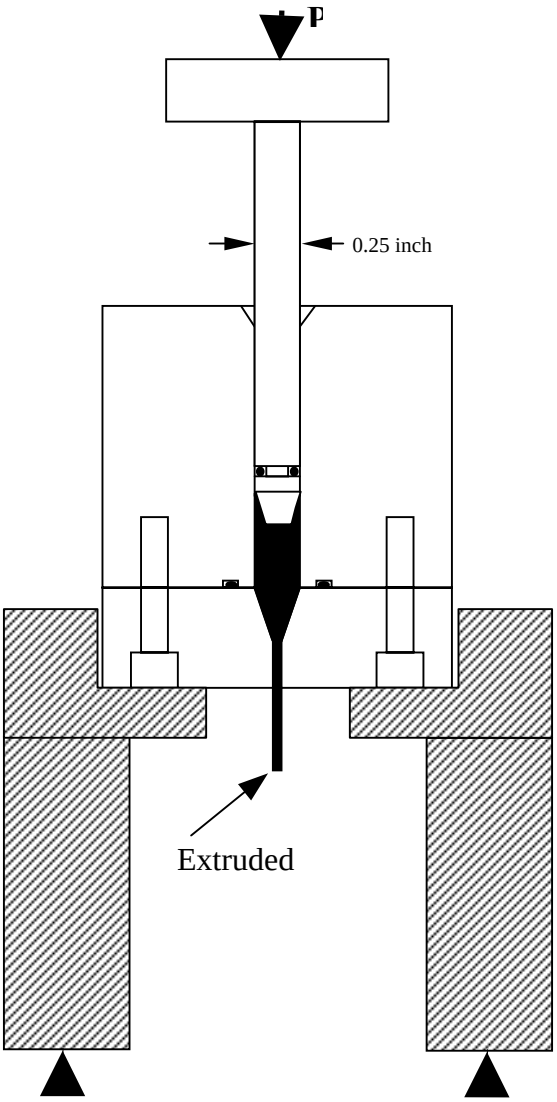

Figure 47: Miniature Extruder Used To Make The Cores Of The Cylindrical Sensors

It consists of a piston and cylinder arrangement with a small hole at one end through which the extruded body flows. The piston and cylinder are mounted on a stand in a Carver laboratory press and pressure is applied through the hydraulically driven rams of the press. The material to be extruded was loaded into the die. Inserting the piston closed the die, and a vacuum was pulled on the open orifice. This is necessary to eliminate air pockets within the batch that, if not removed, will lead to formation of voids in the extruded body. After evacuation for one minute the body was compacted by driving the piston into it at relatively low pressure. The vacuum hose was removed, the loaded extruder was placed in the Carver press and the body was extruded. A long rod of

extruded material is produced which can be cut to the desired lengths with a razor blade. Since all ceramics shrink when they are fired, it was necessary to make the parts oversize. The extrusion orifice is therefore 0.8mm in diameter and the rods are cut to a length of 13.2mm to produce fired cores 0.7mm dia. x 12.0mm long. The linear firing shrinkage of the UF body is 9.8%.

Successful extrusion requires that the feed material or "paste" used in a ceramic extrusion process have a carefully controlled consistency. The paste must flow through the extrusion die but not be so soft that the extruded parts deform when handled. The paste consists of finely divided particles of the ceramic components mixed with a suitable binder. The binder chosen for extrusion of the UF body was CW540, a polyethylene glycol polymer manufactured by Union Carbide Co. and marketed as "Carbowax Sentry." The CW540 binder has the consistency of heavy grease and can be mixed with the ceramic powders to obtain a suitable extrusion paste. Parts made with CW 540 remain soft and pliable after extrusion, but with care they can be handled without excessive deformation. The binder was prepared by weighing a known amount of CW 540 into a clean beaker. The polymer was dissolved with a small amount of methyl alcohol (MeOH). This solution was carefully transferred into a 50 ml volumetric flask, and additional alcohol was added to bring the total volume of the solution to exactly 50 ml. The binder solution was measured out in a 2.0 ml hypodermic syringe and dispensed into the UF powder from the syringe.

The powder and binder were mixed by hand in a small alumina mortar and pestle until the methanol had completely evaporated. The consistency of the resulting paste depended upon the relative amounts of CW 540 and ceramic powder used. The desirable feature of this binder system is that once the alcohol has evaporated the paste maintains a consistent viscosity during all handling operations, including evacuation of entrapped air from the paste. CW 540 has a low vapor pressure and does not evaporate under vacuum at room temperature. The consistency of the UF bodies was controlled, by using enough CW 540 binder to fill the void space in the dry compacted powder.

After extrusion, the rods were dried at 105-110°C for about 2 hours. They were then loaded into a rectangular alumina tray and fired in a flowing atmosphere of forming gas (95% N_2 and 5% H_2). There was a plateau at 500°C to allow time for complete removal of the CW 540 binder. The final firing temperature was 1315-1325°C and the hold time at this temperature was 4-6 hours. The hold (or soak) time was not critical so long as it was above 3 hours. In early firings, the UF cores were supported on a bed of zirconia powder. This was, however, unsatisfactory because grains of the zirconia powder became fused to the surface the rods and they could not be removed in later cleaning steps. The embedded particles gave the cores a rough surface, which could lead to difficulty in subsequent stages of sensor construction. To eliminate this problem, the alumina trays were lined with Grafoil (a graphite paper) and the zirconia bed was eliminated. The UF cores did not stick to the graphite paper and clean smooth surfaces resulted.

As noted earlier, care must be taken to exclude oxygen during the firing of any ceramic containing UO_2. If oxygen is present the UO_2 oxidizes in two stages to give a final product of U_3O_8. Oxidation cannot be tolerated because U_3O_8 is volatile at high temperatures and does not produce a dense strong body. Furthermore, sintered parts containing UO_2 are destroyed by a large volume expansion upon conversion of UO_2 into U_3O_8. Oxidation of the UF body is delayed in comparison to that of a pure UO_2 powder (Figure 47). This is because the UF body has low porosity and at low temperatures oxygen cannot penetrate into it and cause oxidation of the UO_2. At about 720°C penetration of oxygen into the UF body becomes rapid and destructive oxidation occurs.

After firing, the UF rods were ultrasonically cleaned in distilled water, containing a small amount of detergent. They were then rinsed several times with distilled water and ultrasonically cleaned a second time in methyl alcohol. After air-drying the UF rods were ready to be made into sensors.

A small device shown in Figure 48 was constructed to wind the 2.0 mil platinum wire onto the uranium cores. The cores were chucked in a pin vise which, when turned,

advanced the UF core past a fixed wire guide. The pitch of the wire winding was controlled by a set of gears connecting the drive shaft to the shaft on which the pin vise was mounted. In essence the wire winder is a miniature screw-fed lathe. Routine production of tightly wound coils on 0.7mm cores, such as those shown in Figures 49 and 50, was attained with experience and practice.

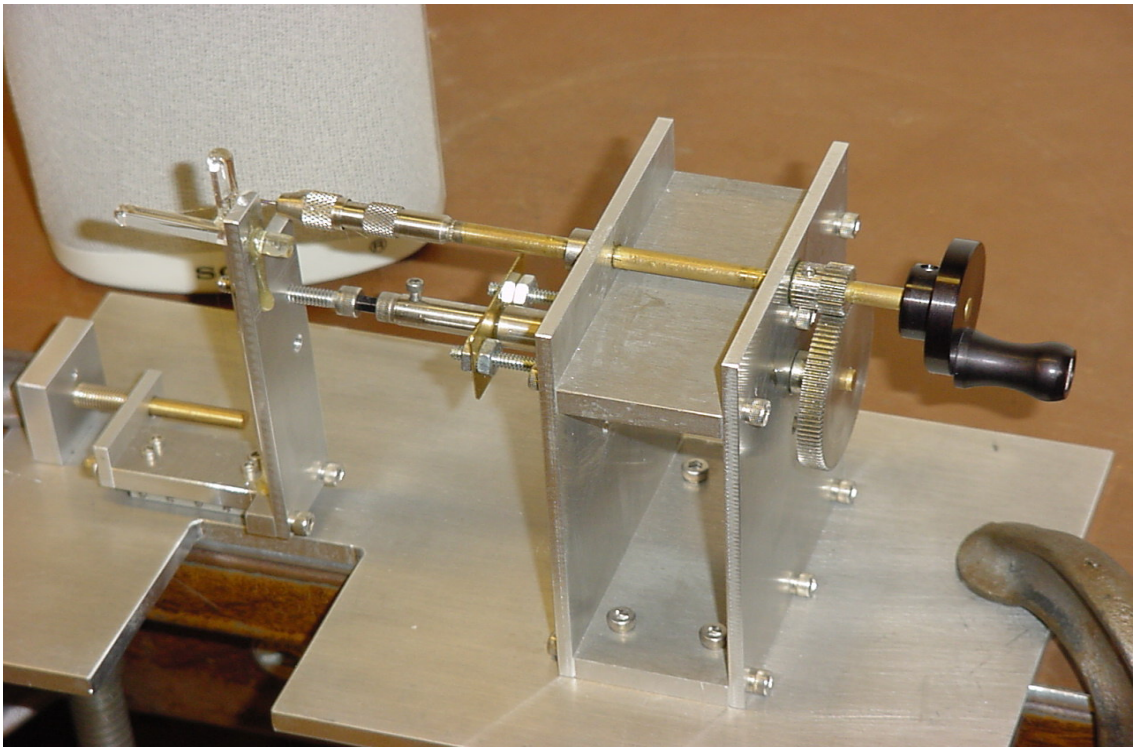

Figure 48: CTPS Core Wire Winding Apparatus

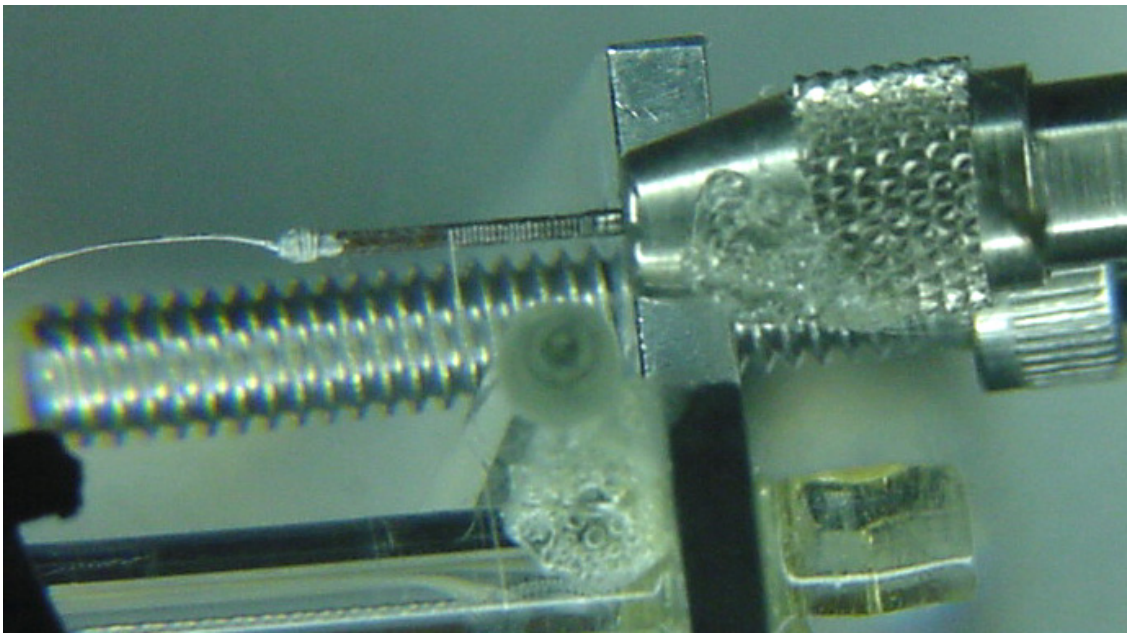

Figure 49: Wire Winding At 10x Magnification

Figure 50: Core At 60x Magnification

After winding the coil, a small spot of platinum paste was placed over the outer most turns of the coil. This kept the coils in place by "gluing" the platinum wire to the UF core. The remainder of the coil was coated with a mixture of beryllium oxide and feldspar using a small brush. Beryllium oxide is an excellent electrical insulator while

also providing thermal conduction properties roughly equivalent to those of nickel. After the BeO had dried for several hours, the ends of the cores were coated with additional platinum to serve as contact pads for the electrical leads. After removing the cores from the pin vise, the platinum contact pads and the BeO layer were densified by sintering at 1250°C for one hour in forming gas.

To produce one of the electrical sensor terminals (center terminal), a short length of 6 mil platinum wire was attached to the platinum pad (note this in Figure 49). Platinum paste was used as the glue, and required a heating cycle at 1250 °C for one hour in forming gas to sinter the material. After this operation the core was ready to be inserted into the platinum socket, which served as one of the electrical leads. These sockets were produced by Edison Welding Institute using small machining tools, and then laser welded to the stainless steel end cap. The sockets were produced with a center hole very slightly larger in diameter than the core. This allowed the core to be snugly fitted into the socket. To do this, a small syringe was used to fill the socket with platinum paste, and the core was inserted. The core was inserted by carefully gripping and twisting it (very lightly) into the socket. Extreme care had to be taken to avoid breaking the cores. This operation was followed by a heating cycle at 1250 °C for one hour in forming gas to sinter the material. The sintered material provides both electrical conductance, and mechanical support. The next operation was to coat the core with a thicker uniform layer of BeO. The BeO plus feldspar mixture was painted on and each time was dried in an oven. After three coatings, the layer was sufficiently thick, and another heating cycle at 1250 °C for one hour in forming gas was used. The final operation to be performed required that a thicker 15 mil platinum lead wire be attached to the thin 6-mil wire. This was necessary because testing had shown the thin 6-mil wire to be too fragile to survive testing. To join these wires, the thinner wire was carefully wrapped by hand around the thicker wire in a tight spiral. This wrap was then coated with a thin layer of platinum paste. After the paste had dried in an oven (100 °C) overnight, a final heating cycle at 1250 °C for one hour in forming gas was used. It should be noted that argon was tried as the shielding gas in the tube furnace, but after cycling at 1250 °C, the stainless steel showed marked oxidation. The argon should have

been sufficient to prevent this, but to be safe, forming gas will be used for these operations in the future.

The cores were taken to Edison Welding Institute (EWI) and laser welded into cylindrical stainless steel cans. This operation is simple. The can is held vertically in a chuck and the end cap with the mounted core is set on top of it Figure 51 shows a view of this arrangement.

A YAG laser was focused on a point toward the outer circumference of the end cap, and cycled on and off. Each time the laser was cycled, a small amount of material was melted from the end cap and joined to the can. The preferred method of doing this was to superglue the end cap onto the can before welding to ensure the correct alignment (core centered in can). Figure 52 shows the view presented through the laser aiming system.

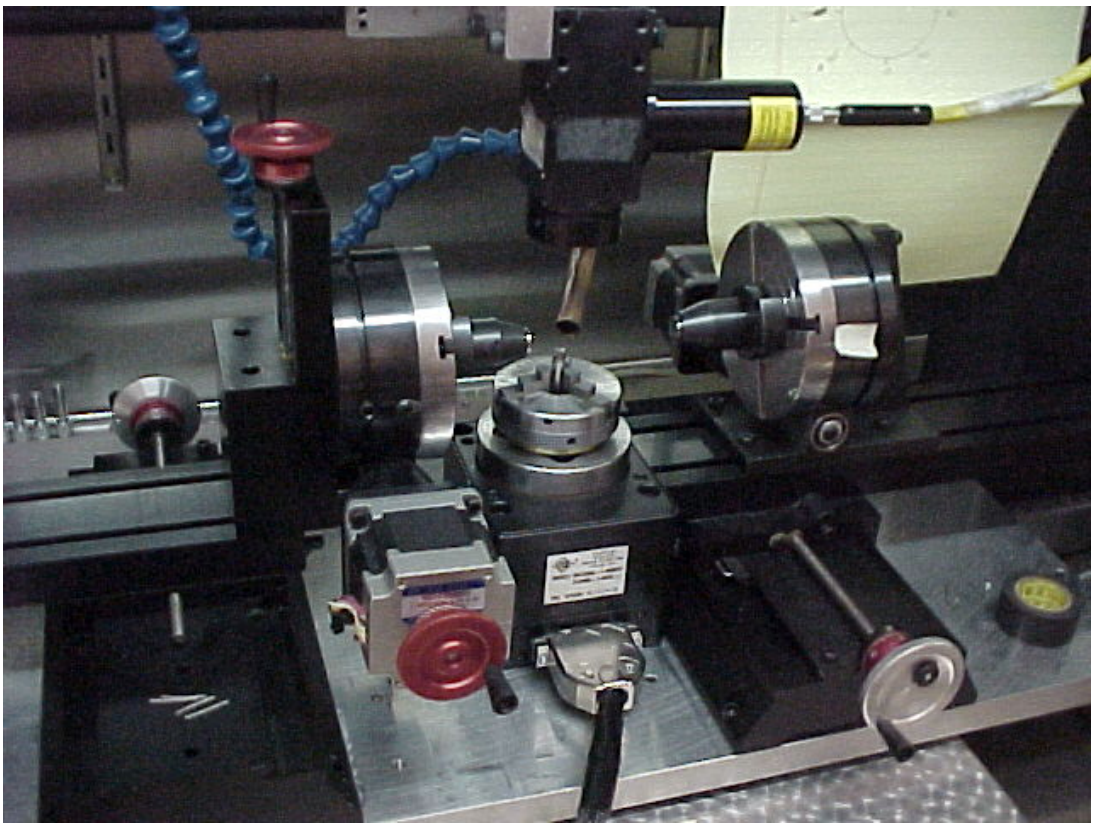

Figure 51: Welding Jig (EWI)

The second electrical lead was a length of 15 mil platinum wire resistance welded to the outside of the can (Figure 53). This weld may need to be shielded from oxidation by coating it with glass, but several test specimens showed that the strength of the platinum-stainless steel weld was greater than the wire itself. Before removing the sensors from EWI, the can was filled with alumina powder to ensure no vibration damage was done to the core.

The only remaining step is to seal the top end of the can with an alumina disk and sealing glass. Tests are in progress to determine the type of seal glass most likely to be successful. Tests have been run with seal glasses sourced from commercial vendors, as well as feldspar glass. The latest testing has shown that running the commercial seal glasses under vacuum is not an option, since they became foamy due to out-gassing of volatile components. However, feldspar can withstand this environment. The glasses have been tested under heating schedules in pure hydrogen, forming gas (95% nitrogen 5% hydrogen), pure argon, and air. Feldspar is compatible with any of these environments, while the commercial seal glasses are incompatible with hydrogen. Therefore, heating cycles with these glasses will take place in argon.

We will now discuss progress made in Year 2 concerning fabrication of sensors of the planar geometry. The planar sensor has an overall diameter of 13mm, which means that the heater must fit within a circular area 10 mm in diameter. To match the instrumentation used to drive the sensor, the room temperature resistance of the heater should be about 10Ω. The resistance of the Heraeus ink, which is used to make the heater, has a resistance of ~ 35 milliohms per square at 10 micron fired film thickness. Therefore 286 squares are needed to make a 10Ω resistor. The problem is then to pack 286 squares into a 10mm circle, in a configuration which will result a total resistance of ~10Ω.

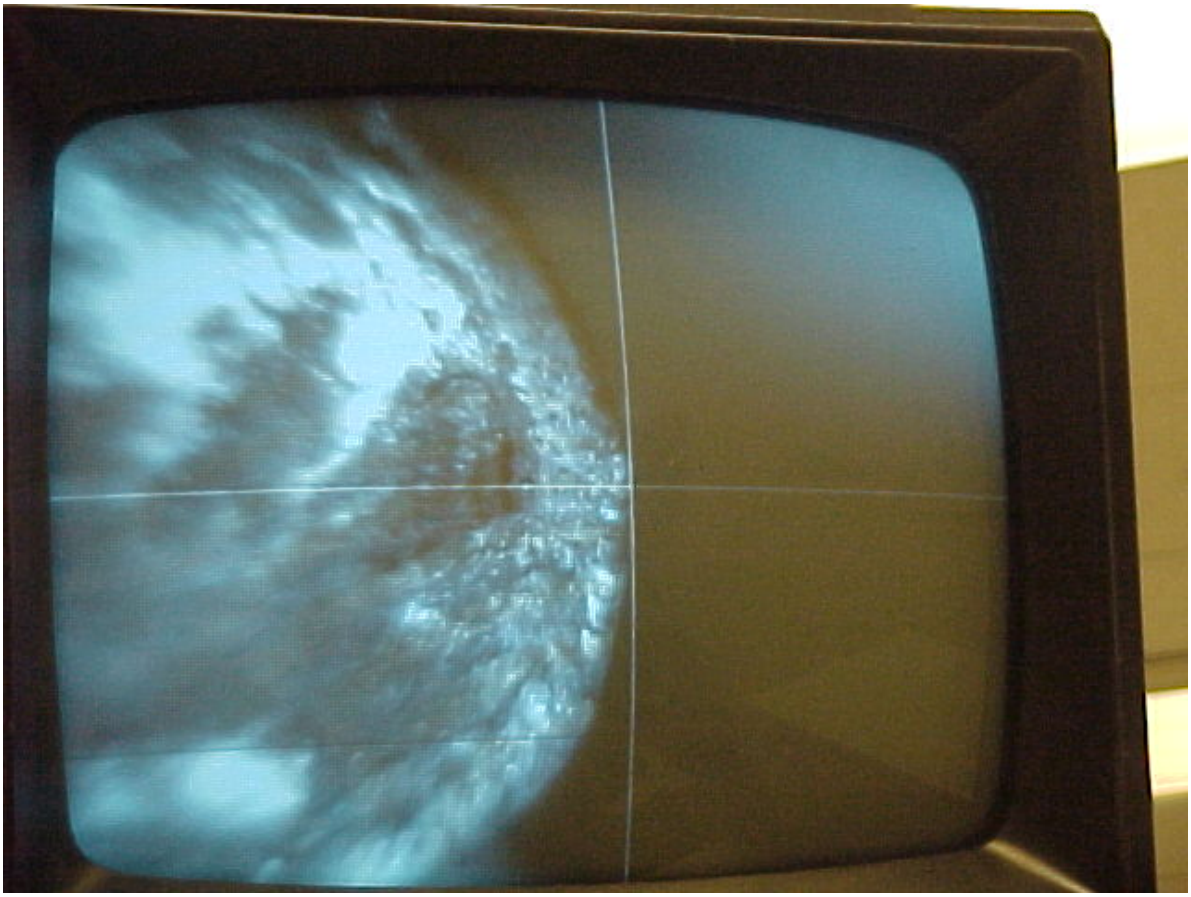

Figure 52: View Of The Laser Aiming Screen

The approach taken was to assume a geometry for the heater Let n = the number of platinum bands; and n-1 is the number of gaps between the bands. If we assume that the bands and gaps are equal in width, the width of the bands (W_b) can be calculated from

$$W_b = \frac{R_h}{n + n - 1}$$

where R_h is the outside radius of the largest heater band. By assuming a value of n, one can then calculate the total length of the heater band and its resistance. To achieve a 10Ω resistor with the Heraeus ink will require a heater with 7 bands. The width of these bands (i.e., the size of the squares) is then 0.385mm. The length of the heater is 110.1 mm (or 286 squares) and its room temperature resistance is 10.0Ω. The heaters were supported on alumina substrates, which were 20 mil thick and contained two 10 mil vias to accept the platinum leads. They were purchased from Laser Tech Inc.

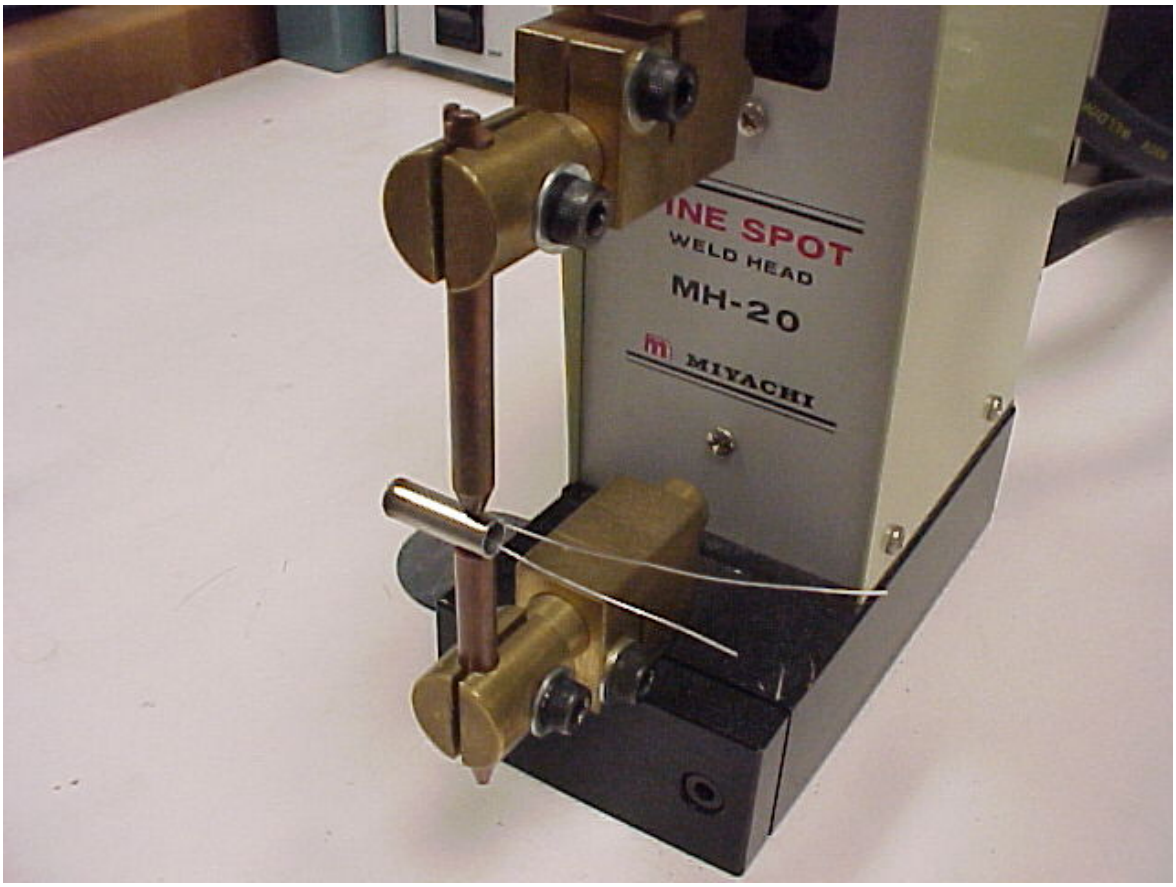

Figure 53: Resistance Welding Platinum Terminal To The Stainless Steel Can

The design of the planar sensor is shown in Figure 54. This sensor is intended for use at high temperatures, that is, temperatures up to ~1200°C. These sensors have been constructed using screen printing techniques. The design of the planar sensors calls for screen printing of several layers onto alumina substrates. Before screen printing the platinum heater onto the substrate, the two 6 mil sensor leads were threaded through the vias and sealed with feldspar glass. The sealing operation was done at 1325°C in air. After inserting and sealing the leads, the platinum heater was screen printed onto the substrate. This is done by placing the substrate under a patterned stainless steel screen and forcing platinum ink (Heraeus OS2 CL11-5100) through the openings in the screen and onto the substrate (Figure 55).

This operation builds up a consistent layer of platinum on the substrate. The printed heater was dried and then fired at 1325°C in air. During the heating, the platinum

ink sinters onto the platinum leads and establishes electrical connections to the heater. Although the connection appears to be quite tenuous, the contact resistance between the wire and the sintered ink was measured to be only 0.2Ω. Other screen printing steps follow after the heater is in place. The next step for the basic sensor was to print the UO_2-feldspar (UF) layer on top of the platinum heater using a circular pattern.

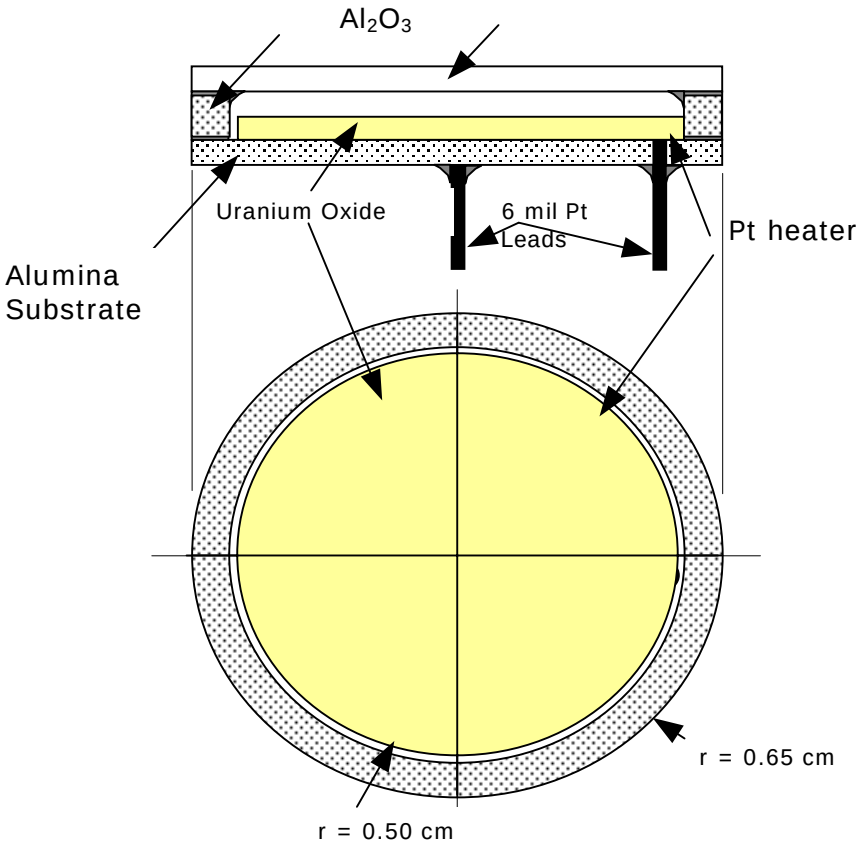

Figure 54: Planar Sensor

This operation needs to be done three times, each time allowing the ink to dry under a hot air gun for ten minute before the next layer is printed. After firing this coating, a band of feldspar was screen-printed onto both the substrate and the sapphire or alumina cover. Organic materials in the feldspar ink were burned out at 350°C in air. The printed substrate, alumina ring, and cover were stacked in the proper sequence, placed in a vacuum furnace and fired at 1325°C to seal the entire structure. Beside the basic sensor with the uranium layer directly on top of the platinum heater, there are several variations. One requires that a layer of alumina be printed on the heater to act as

a fission fragment shield between the heater and uranium. Either version of the sensor can have either no insulation or alumina insulation on top of the uranium layer. After all screen printings were completed, the cap was glued to the substrate. This cap is made of a substrate with no holes, and a circular alumina washer. Feldspar glass was used in all operations, and the firing was done in a vacuum furnace. Figures 56-57 show the results of these subsequent fabrication steps.

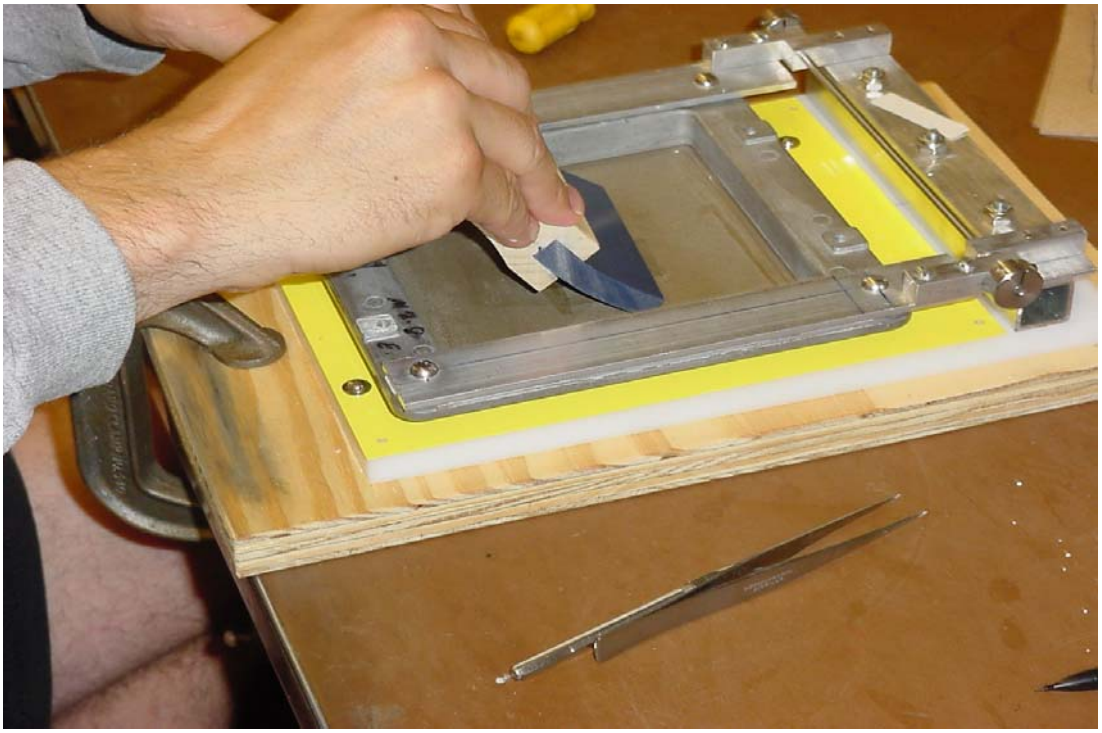

Figure 55: Screen Printing Operation

Figure 56: Screen Printed Platinum After The Sintering Operation

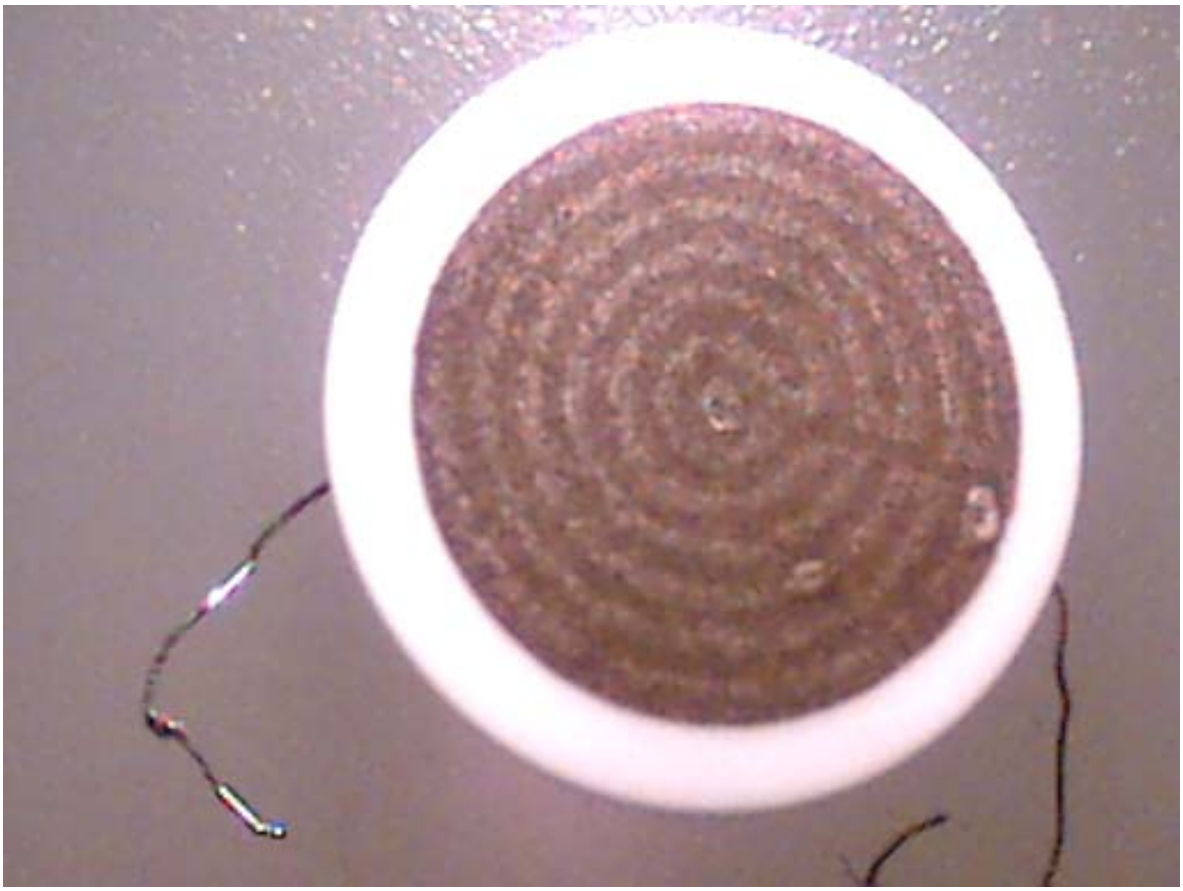

Figure 57: Screen Printed Uranium Layer

To date we have six competed sensors, each a different combination (i.e. one with an insulating alumina layer, one with no alumina layer, etc). These sensors are not currently undergoing testing because the 6-mil lead wires are too fragile to put in the test facility. Previous testing experience has showed that these leads will break, destroying the sensor. To correct this problem, short 15 mil platinum leads will be attached to the sensor leads and glued to the sensor substrate. To join the leads, the small sensor lead will be wrapped around the thicker wire. This will be coated with platinum paste and fired (the same process already used successfully on the cylindrical sensors). Feldspar glass will be used to glue the new leads to the substrate, providing mechanical support and strain relief.

3 SENSOR TESTING PROCESS

3.1 TESTING METHODOLOGY

Experimental testing of the second generation CTPS prototypes is designed with three main objectives for each sensor: 1) to establish linearity of response, which is whether the sensor will respond to changes in reactor power linearly (i.e. a change in reactor power will result in a linearly related change in sensor signal); 2) to determine sensitivity which is a measure of how much the sensor output changes in response to a given change in the quantity being measured (reactor power); 3) to determine the practical bandwidth (the highest frequency the detector can respond to). The OSU nuclear reactor and LVEC facility afford an experimental setup to address these objectives. The OSU nuclear reactor is designed and instrumented to raise power and maintain a very consistent power output. Because of this, linearity of response is easily tested by varying the reactor power from zero watts to 450 kW and matching the sensor response to each power change. Sensitivity is determined from this process as well. The neutron oscillator facility allows a deterministic measurement of the sensor bandwidth. This is done by taking ten second measurements of the sensor output while the oscillator runs at varying speeds to above 10 Hz. The use of noise analysis has not proved successful due to the use of unshielded cabling and lack of an anti-aliasing filter on the sensor data acquisition channel. This was a problem endemic to the first generation CTPS prototype sensor testing and it was attributed to the large noise signal[4]. That earlier experiment used the same controller and a very similar digital data acquisition system which lends more weight to the results determined for this round of testing. The results and analysis of noise analysis for the CTPS were discussed at more length in the findings of the earlier experiment.

3.2 SENSOR CALIBRATION

The first step required to test the CTPS sensor is a calibration to determine that the resistance is linearly related to temperature and to define that relationship. The linearity is important because the controller uses the resistance value to alter compensation power. A non-linear resistance change with temperature could prove a

serious control problem, though due to the complex nature of the materials interactions, a perfectly linear relationship is not expected at very high temperatures.

The calibration testing is done on the bench top utilizing a PID controlled oven capable of maintaining high temperatures (1000 ^{o}C), and a calibrated ohm meter. The sensor to be calibrated is inserted into the oven with high temperature wire insulation electrically isolating the terminals. Resistance measurements are taken at temperatures ranging from room (about 25^{o}C) to 800^{o}C. At each temperature, several readings must be taken over a span of several minutes once the oven temperature has stabilized. This ensures the internal sensor temperature has come to equilibrium. From these data, a resistance versus temperature calibration curve can be plotted. This curve allows the correct choice of set point as well as easy determination of actual sensor temperature (based on the real time resistance measurement available) during testing.

3.3 LVEC FACILITY SETUP AND REACTOR POWER TESTING

The LVEC, as previously covered, was designed specifically to test the CTPS sensors. The setup process including the CTPS operations checklist is included in the appendix. Working with the sensor in the facility and the electronics hooked up then requires that the controller be tuned in semi-operational conditions (blower loop running at correct temperature with the reactor shut down). To tune either controller, a choice of set point must be made before tuning, as the controller tune is slightly dependent on the sensor power demands. Tests of several set points showed that control was considerably better at a high set point, most likely due to faster thermal dynamics. To preclude testing at non realistic conditions (i.e. setting the sensor to run at a delta T much higher than it could in practice), a maximum set point equivalent to 250^{o}C above bulk temperature was chosen.

The PID digital controller must be tuned manually, for this process the well known Zeigler-Nichols tuning routine was chosen. The process requires setting the integral and derivative actions to. Once this is done, increase the proportional gain until the signal oscillates with constant amplitude (i.e. not settling out or going unstable). Between gain adjustments, the set point may have to be changed slightly to unsettle the

signal and start it into an oscillation. Record the period of oscillation and reduce gain by one third. Use the period of oscillation to find integral (I) and derivative (D) constants where I = period/2 and D = period/8. From observation, it is clear that this process should be repeated for any significant change in the set point.

To tune either the analog proportional controller (APC) or digital proportional controller DPC the idea is to assign the correct gain for the system. Too much gain causes the system to become unstable and the signal is obscured in noise. Too little gain, the system is too slow to follow fast transients and the offset error is very large. To do this effectively, no easy way was found other than testing several gain settings and assessing which allowed the system to perform best. To test gains the controller was adjusted to the set point to be used for reactor testing. The system was run at steady state (i.e. zero reactor power), increasing the gain by a set amount every 500 seconds. To illustrate the process the following figure shows the resistance values of the sensor for several gains as tested with the APC.

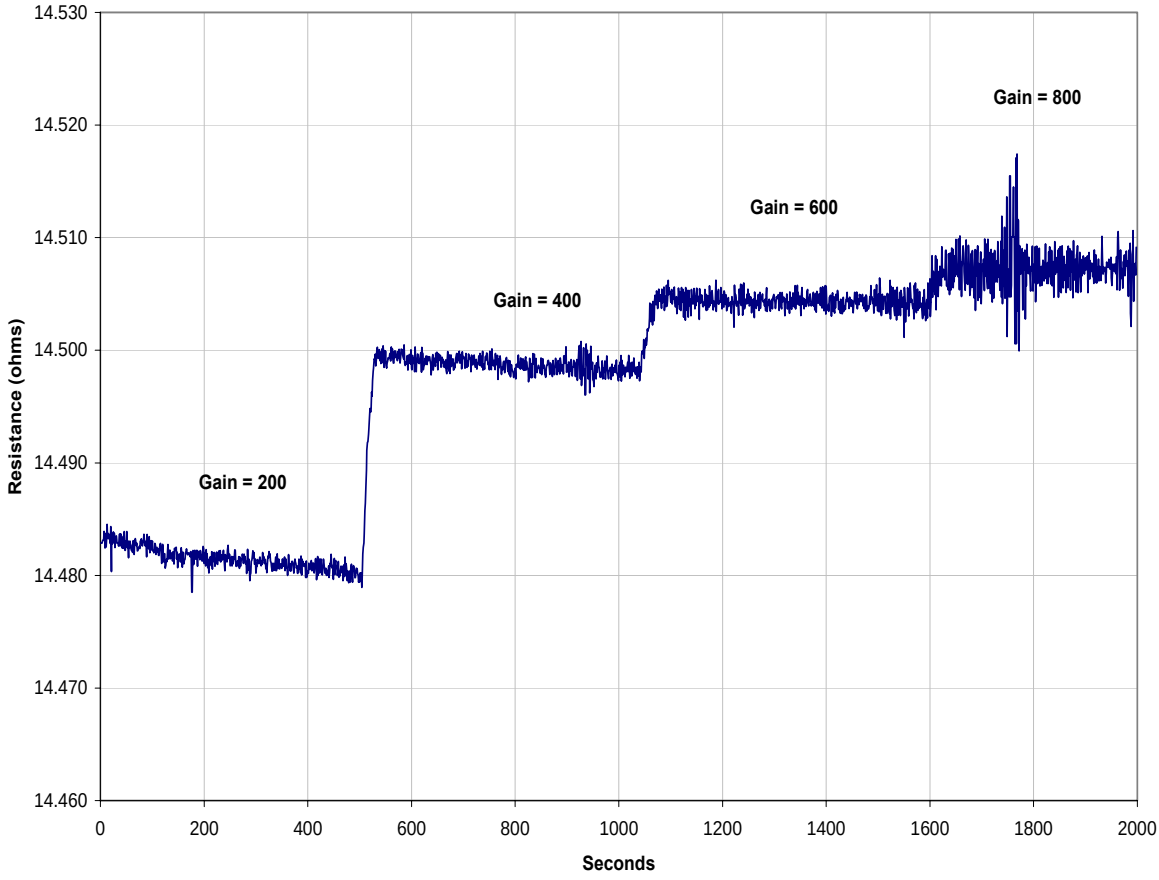

Figure 58: Testing set point stability for several APC gains

As can be seen from the plot, as the gain is increased in steps of two hundred (units of gain for the APC using the front panel potentiometer gain adjust), the offset error is minimized with diminishing returns as the gain increases. Also apparent is the increase in signal noise amplitude. As is seen, a gain of two hundred shows relatively low noise but great offset error, while the gain of eight hundred (one thousand is maximum gain) shows little offset error but large noise. A gain of six hundred is clearly the best gain evaluated here because the offset error is relatively low, while noise is also low. Additional tests evaluating additional gain settings were done to converge on an ideal gain for the APC, and like tests were run for the DPC. Because the APC became the primary controller, fully instrumented reactor power tests were run at several gain settings to further evaluate the correct gain. The gain settings used for most tests were

either four hundred or six hundred. These settings are known to be close to the gain setting range most useful for first generation in reactor CTPS testing[1].

The test method was very similar for both types of sensor regardless of the controller used. Before reactor start up, the controller was powered up to the correct set point and gain settings, and allowed to settle out for several minutes before starting the data capture. To determine that the controller was functioning correctly in real time, Labview DAQ program pctrltest.vi was used because it is programmed to display the sensor power graphically similar to an oscilloscope. Once the controller was operating, the main labview vi was loaded and data capture began. This VI allows the user to switch between fast stream capture for oscillator testing, and normal data capture mode. In order to establish a representative data sample, the data capture continued through the entire reactor run. A typical run consisted of ramping reactor power up to one kilowatt from zero power and holding for ten minutes. The reactor power was then increased to three kilowatts, then to ten kilowatts, up through 30 kilowatts, 100 kilowatts, 300 kilowatts, and finally to 450 kilowatts (full reactor power). Each of these power levels were maintained for at least ten minutes, though longer runs of up to two hours were made at the higher powers to test various sensor capabilities including bandwidth. The bandwidth measurement was done at full power with the flux oscillator operating at several speeds. Data was taken utilizing the streaming data capture capability of the data acquisition system at flux oscillation frequencies of 1.5 Hz through 15 Hz. Each of these measurements was taken after manually setting the oscillator motor speed as close as possible to intended speed. The measurements were taken for ten second intervals for each measurement. Several measurements were taken of sensor response to both dropping one rod, and full reactor SCRAM. Each data set was then analyzed using a combination of Microsoft Excel and Matlab 6.5.

3.4 TESTING OF THE CTPS PLANAR SENSORS

As previously presented, the planar sensor design allowed the construction of more than forty completed sensors. Of these, bench testing was completed on about half, while fully instrumented testing was accomplished for two. Bench tests were run on each

sensor to determine the resistance/temperature calibration, and to determine that each was controllable as expected. These tests led to the discovery that the uranium oxide layer was electrically conductive at higher temperatures. An example of one such sensor, planar #16, is shown in the following figure.

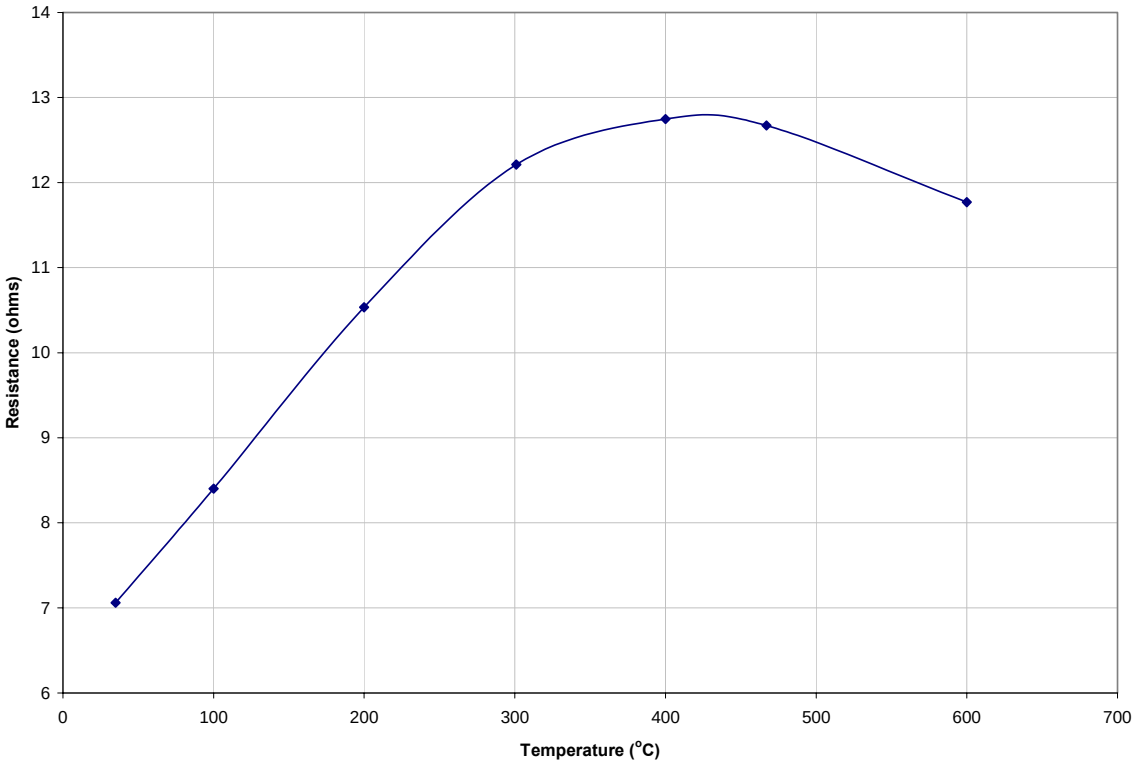

Figure 59: Calibration curve for planar CTPS #16

As can be seen from this figure, sensor resistance increase is linear until some point between two hundred and three hundred degrees Celsius. These results were repeatable, and forced testing to focus only on the sensors that include the alumina layer between the platinum and uranium. The two sensors that were fully tested included one unloaded sensor designed to gauge the gamma sensitivity, and planar #28. The calibration curves for both were very linear at all temperatures. Shown for example is the graph of planar #28 in the following figure. The linearity of resistance change is very good with excel calculating the R-squared (a measure of fit of the straight line) value as .9999. The slope

is 0.0225, so for each degree increase in temperature, there is a corresponding 0.0225 ohm increase in resistance.

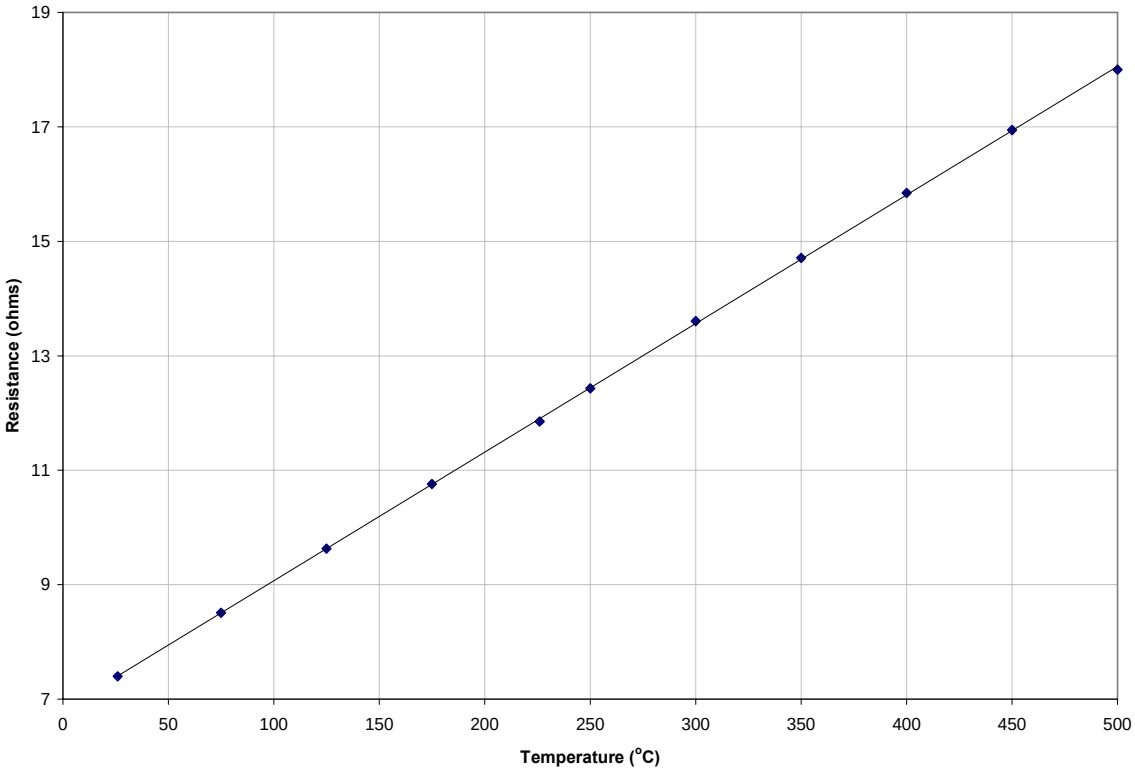

Figure 60: Resistance calibration for planar #28

Once a calibration curve is generated, the sensor is tested on the bench top with the controller operating, to preclude the possibility of any unforeseen performance problems.

3.5 IN REACTOR TESTING OF PLANAR # 28

Initial testing of planar sensor #28 was accomplished using the Labview PID control system. The use of this controller is important to achieving the ultimate goals of CTPS development as was previously discussed. Extensive testing effort was invested in pulling information from the PID controller data, but its performance was disappointing. Instead of providing a noise free signal, with a fast settling time and no steady state error, the controller delivered a very noisy signal that had to be processed to glean any useful

information. Processing of the signal by way of moving average gives a cleaner signal, but effectively slows the response. An example of CTPS response using the PID controller is shown in the following figure with the dark line being the moving average of the sensor data.

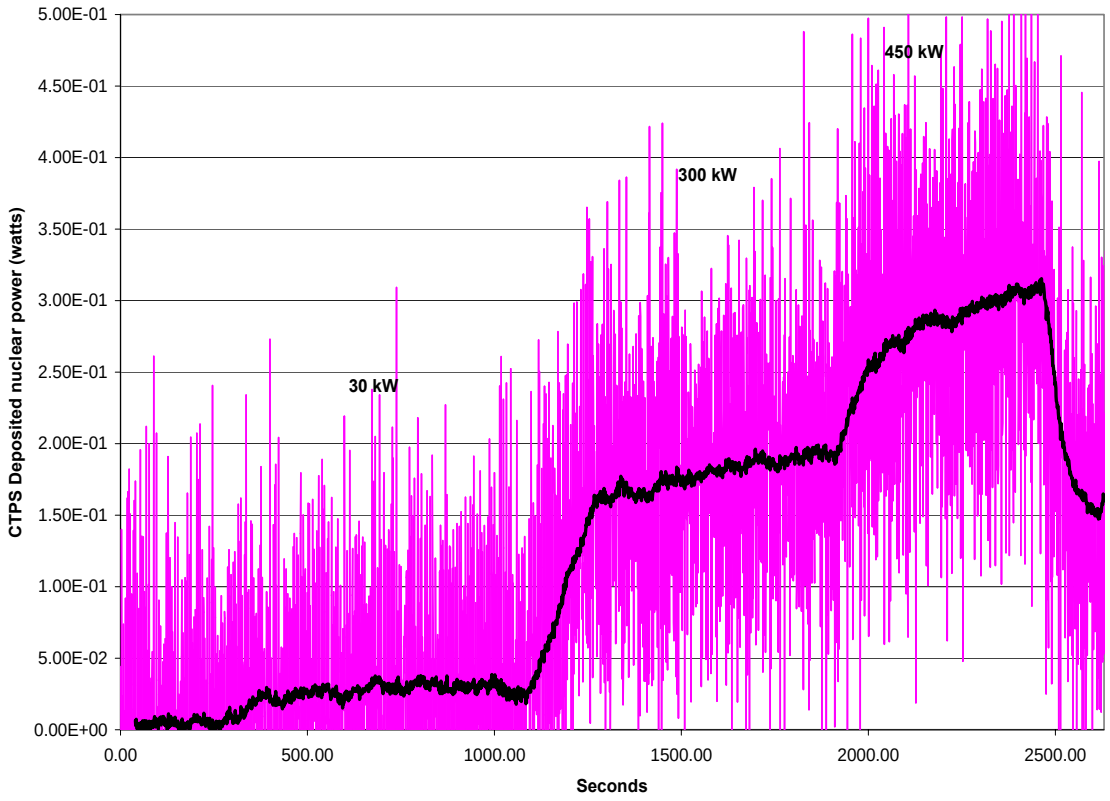

Figure 61: Planar #28 response with PID control

In any event, the noisy oscillations were present in the control signal, and were of sufficient amplitude to prevent the successful higher frequency testing of the sensor. This eliminated the chance of getting useful information from the oscillator tests because control actions were not of sufficient amplitude to detect even with extensive processing. Multiple attempts were made to tune the PID using the Ziegler-Nichols process, but only small improvements were shown in controller performance. Even with these controller issues, it is apparent from the figure that the sensor responds to reactor power changes

and is in fact controllable. The DPC was tested and found to work, but it was not as stable as the APC. In addition, the DPC was a stand alone controller written in Labview, and mode two operation would not have been tested even using the DPC it as primary control.

Once the decision was made to use the APC, testing of the labview controller mode two was necessarily abandoned. Mode two has been shown to work as designed, but the absence of effective digital control precludes instrumented testing at this time. The APC was tuned using the previously mentioned procedure, and shown to control well enough to allow a full evaluation of sensor performance. For each run, the system recorded data for several minutes before a reactor startup was initiated so that good baseline data was available. Power was typically ramped up with roughly a thirty second period (with period defined as the amount of time necessary for the reactor power to double). Raw data for the CTPS is a measure of change in electrical power, so at highest reactor power the CTPS reads its lowest level. To convert this to a measure of deposited nuclear power, data was subtracted from the baseline, so that the baseline became equivalent to zero deposited power. An example of the power curve is given in the following figure, which is based on data from the APC.

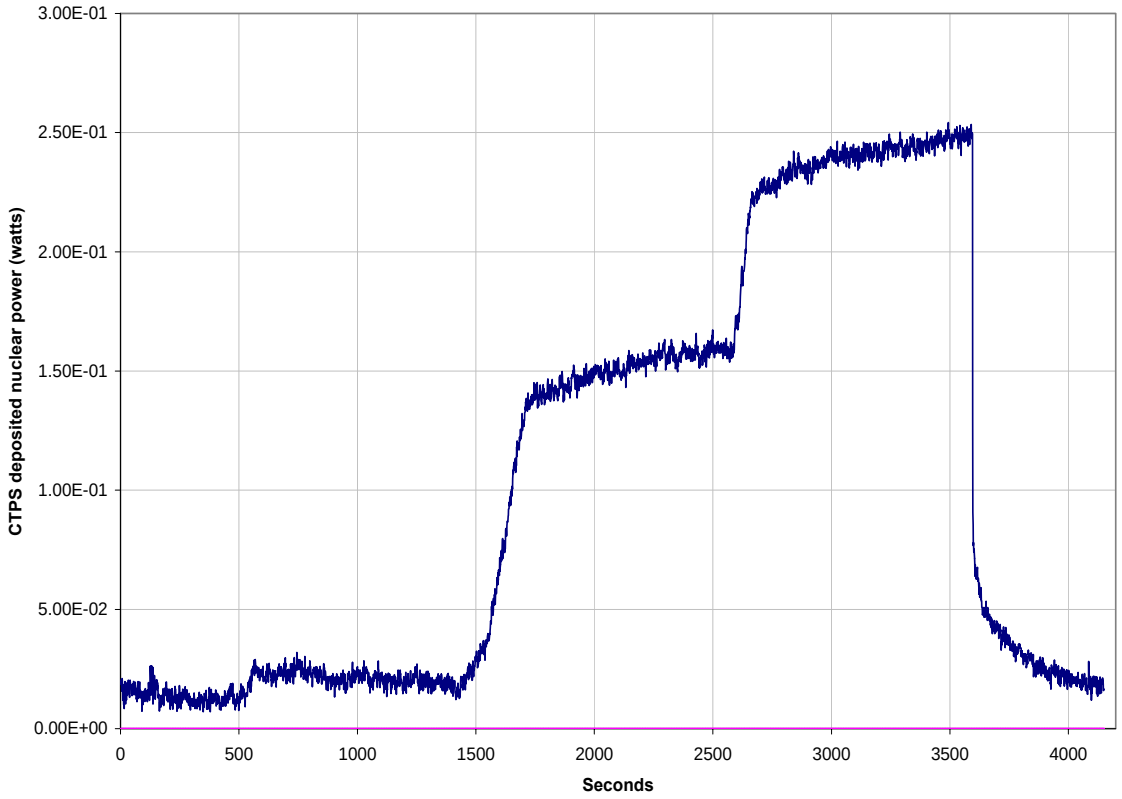

Figure 62: Reactor power curve (APC) planar #28

Comparing this curve to figure four shows the obvious difference made by using the APC versus the PID system.

The other major component of testing was the measurement of bandwidth using the neutron oscillator. The Labview VI written to allow data stream capture is programmed to take ten second data captures, which at the one thousand Hz sampling rate, is ten thousand data points. Oscillator settings ranged from two to ten Hz in increments of 1 Hz, and fifteen Hz. This data was processed similarly to the previous data to show a plot as in the following figure.

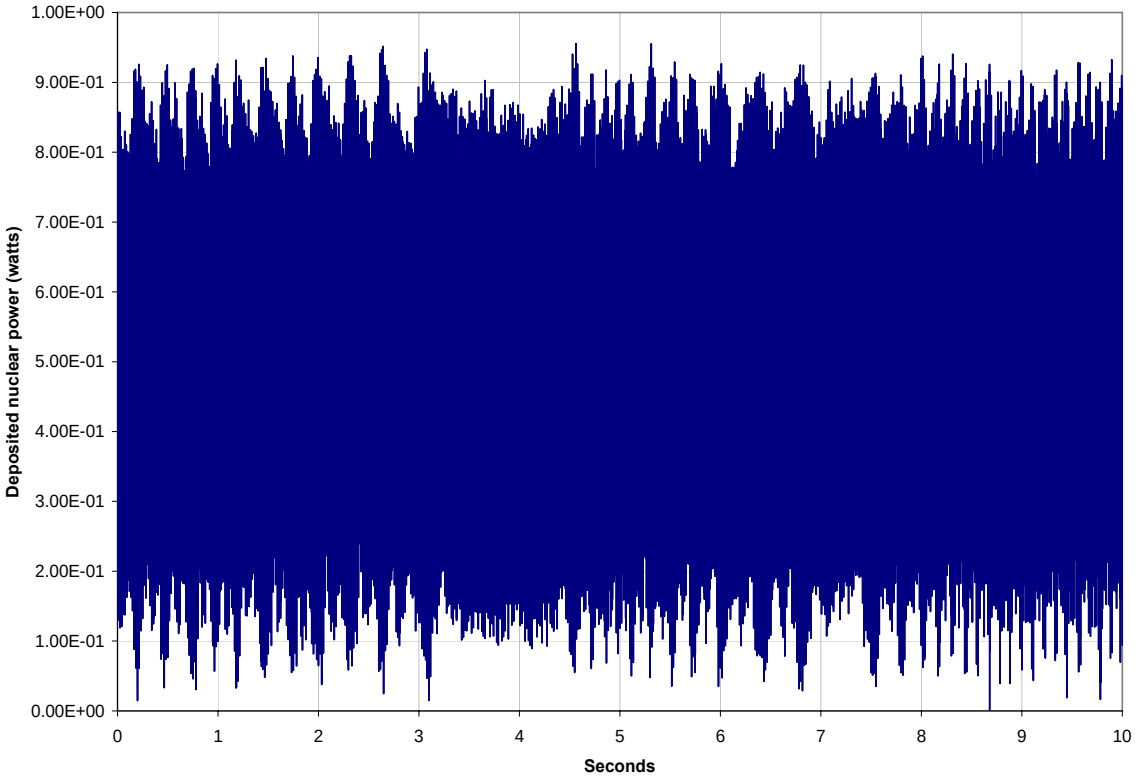

Figure 63: Three Hz flux oscillation

It is obvious that there is a periodic signal, but the noise is sufficient to obscure much of the information. This is a problem that will be addressed in the following chapter.

3.6 TESTING OF CTPS CYLINDRICAL SENSOR #1

As for the planar sensor, testing of cylindrical sensor #1 required bench testing that included plotting a calibration curve. The cylindrical sensors do not have an electrically insulative layer between the platinum heater and the uranium, so there was concern that they may show the same non linear resistance and temperature relationship

as had non-insulated planar sensors. The following plot is the calibration curve for cylindrical #1.

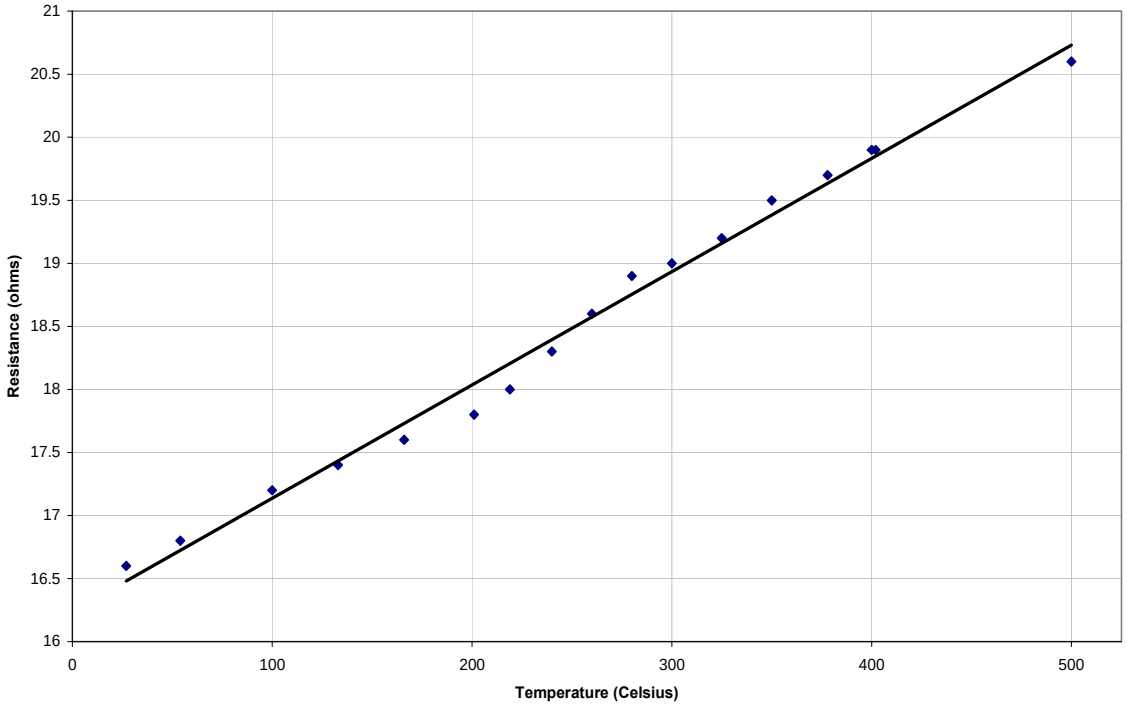

Figure 64: Resistance calibration for Cylindrical #1

As can be seen, the points do not fall perfectly in line, but they are reasonably close to the line. The effect seen with the defective planar sensors points to a highly non-linear resistance change as the temperature rises. In this plot the higher temperature behavior looks linear, and the five data points falling slightly away from the trend line do not seem to indicate nonlinearity. Instead these could be due to bad measurements, possibly taken before the sensor had reached equilibrium. The fact that non-linearity was not observed points to the difference in construction between the two sensors. The planar sensor electrical element has much surface contact with the uranium, as they are rough surfaces composed of very small particles. The cylindrical heat element is a wire that has only

edge contact with the uranium, and may in some places be separated from the uranium by the BeO coating.

3.7 In reactor testing of Cylindrical #1

Reactor testing was accomplished using only the APC, as the PID controller did no better with the cylindrical sensor than it had with the planar. An effort was made to tune the PID and digital proportional controllers, and test with in hopes that the different geometry and materials would enable better performance. Once it was determined there was no improvement, digital control was abandoned for this round of testing. The tests were run in the same way as for the planar sensor, with similar results as in the following figure.

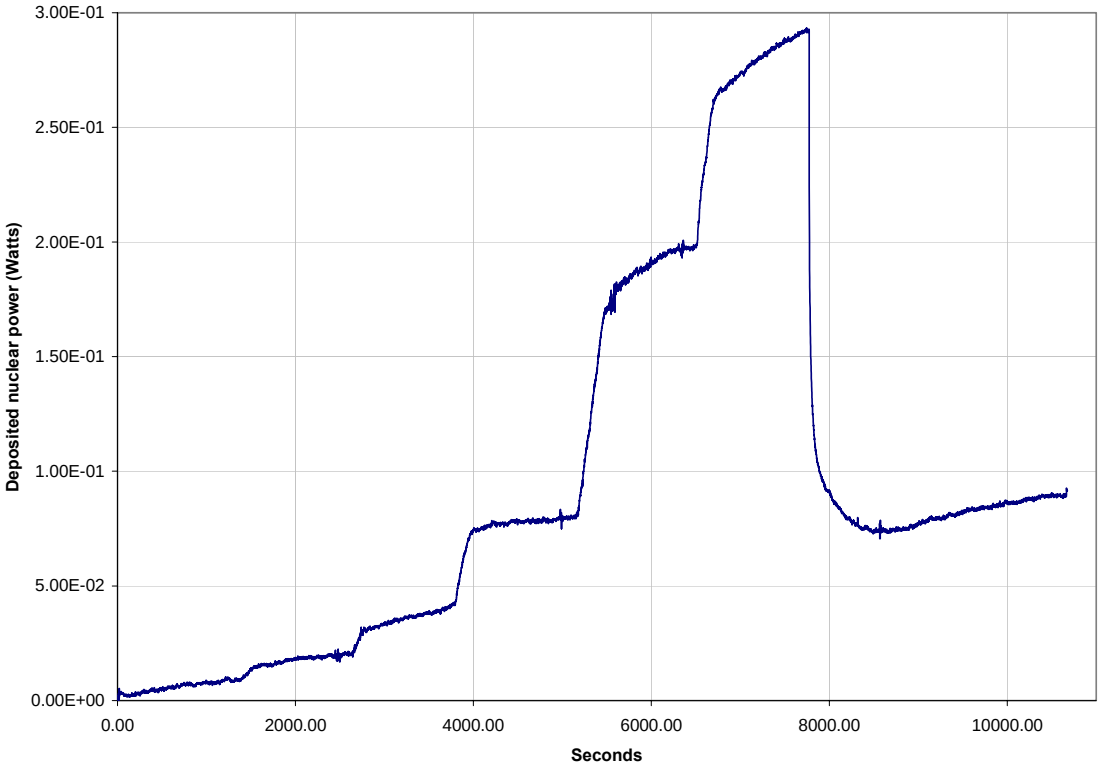

Figure 65: Reactor power curve (APC) Cylindrical #1

Oscillator testing of the cylindrical sensor showed the same problems with noise. The same tests were run at increments of one Hz from two to ten Hz. An example of a cylindrical sensor oscillator test is shown in the following figure. As in planar sensor testing, there is a significant amount of noise that obscures the CTPS response to the neutron oscillation. Again, this will be addressed in the following chapter.

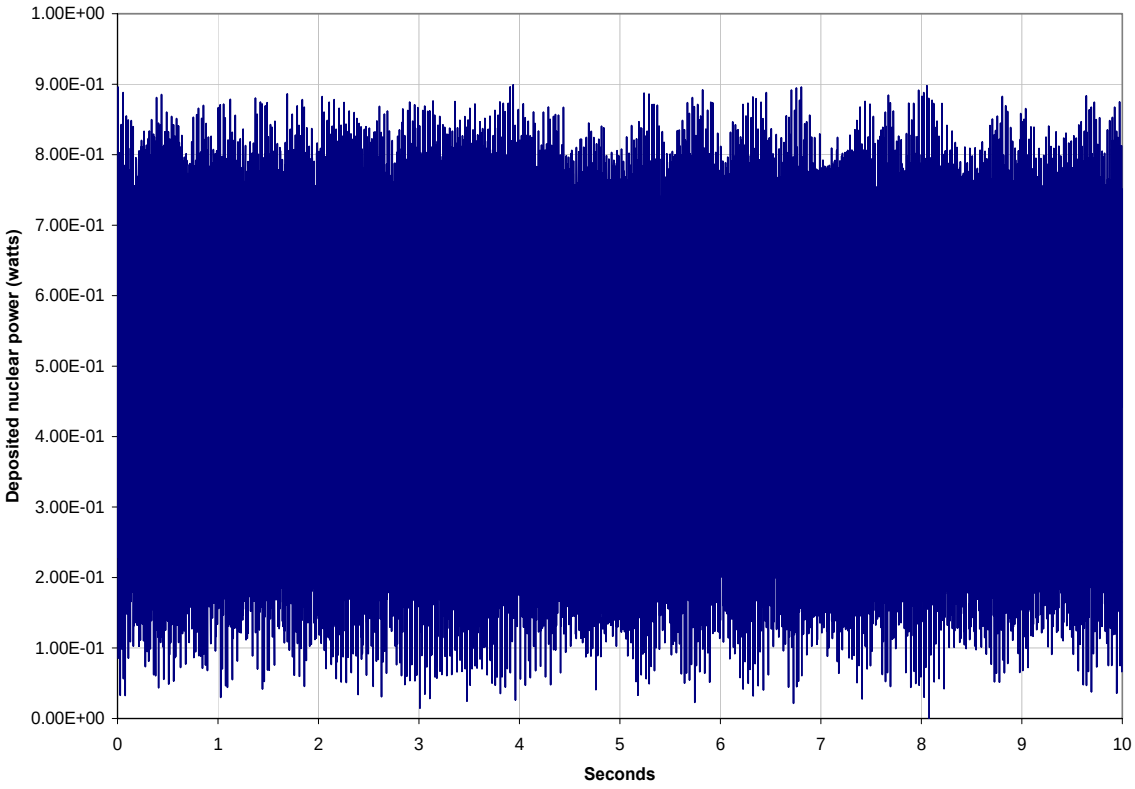

Figure 66: Nine Hz flux oscillation

4 EVALUATION OF SENSOR PERFORMANCE

4.1 EXPERIMENTAL RESULTS AND ANALYSIS

As presented earlier, the objectives of these experiments are to determine whether the sensors respond linearly, to find the sensitivity of the detectors, and to determine the practical bandwidth. Analysis of experimental results is broken up for each sensor into sections dedicated to determination of linearity and sensitivity, and investigation of sensor bandwidth. An additional section is dedicated to using this experimental data to compare to data from the computer models.

4.2 PLANAR SENSOR #28 EXPERIMENTAL EVALUATION

As was discussed previously, the PID control system was very noisy and as such, was not used for most of the testing. However, the initial planar sensor testing was done with PID control, and there are several things that can be gleaned even given the amount of noise. Figures 4.1 and 4.2 are from a test using the PID controller. For this test, the reactor power was increased to 30 kW and held for ten minutes, then increased to 300 kW and held for ten minutes, and finally increased to 450 kW for eight minutes before being shut down. From this graph of CTPS power versus time, it is clear that the sensor followed these power increases but the amount of uncertainty due to noise makes the data very difficult to examine, even so, it is possible to calculate the linearity of response of the sensor.

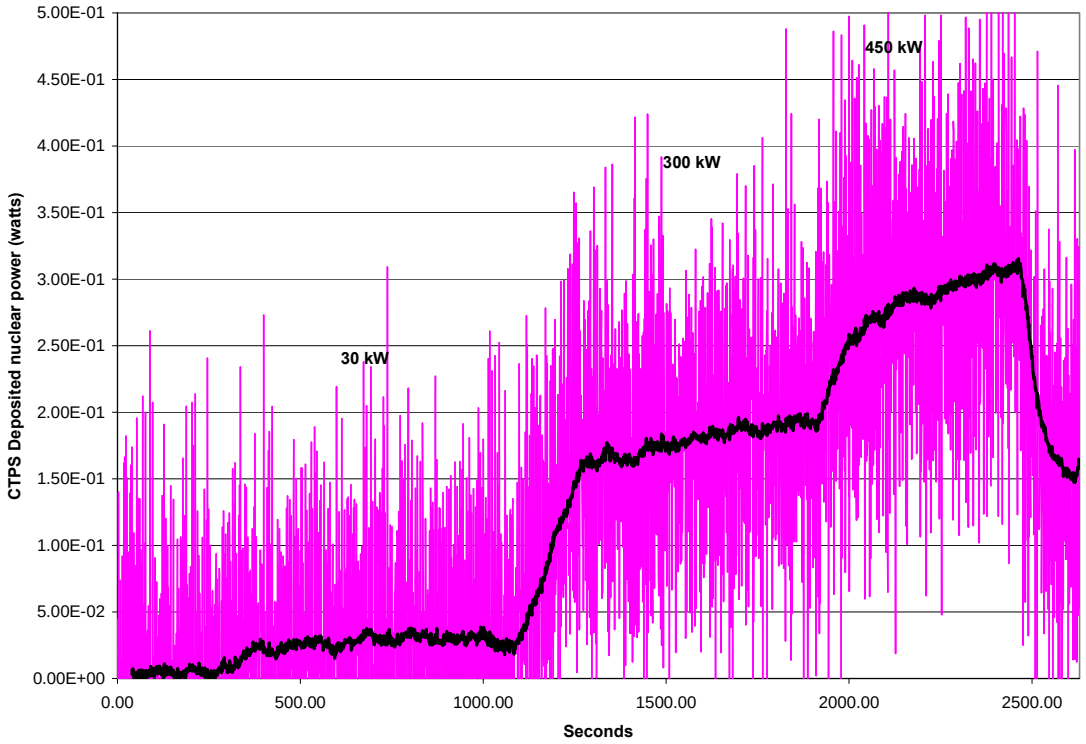

Figure 67: Planar #28 PID controlled

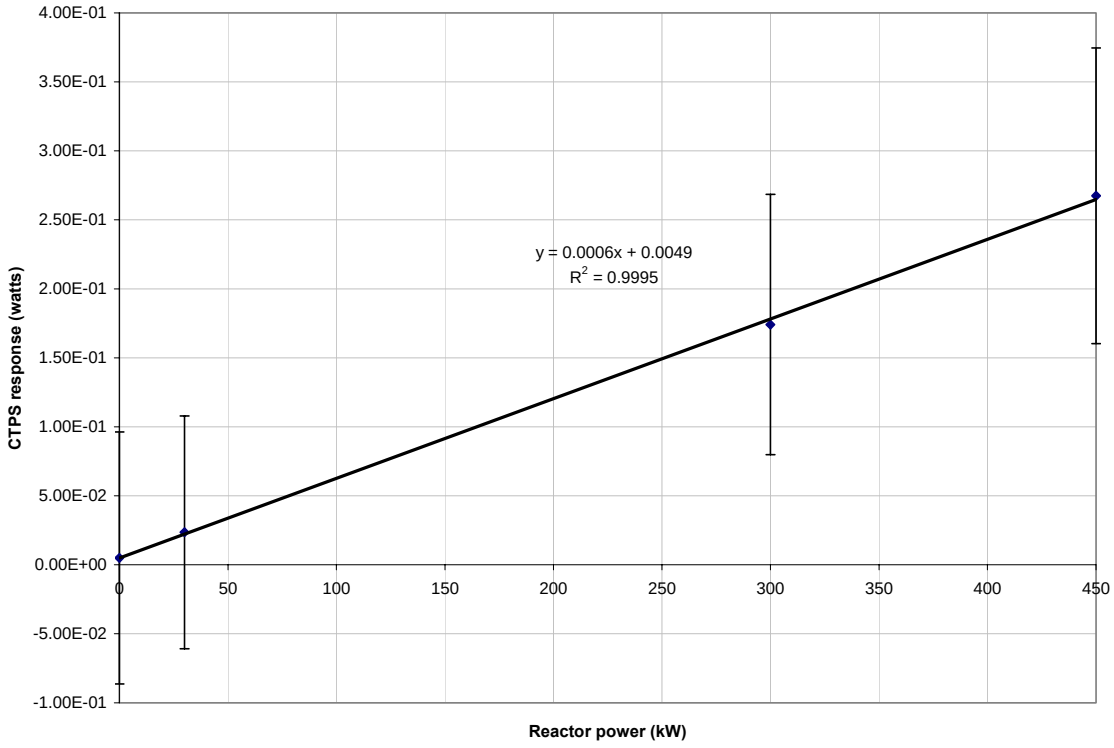

Figure 68: linearity of response for planar sensor #28

For the linearity plot, the CTPS response is needed at each power, but because the response doesn't stay very constant, these values are difficult to determine. The best solution that could be found was to average a large number of data points at each power level (200 points). Doing this for each of the four power levels and graphing it in excel gives figure 4.2, the linearity of response plot. Error bars showing the standard deviation at each point illustrate how much the PID controller oscillates around the correct value. Excel can fit a straight line to the average points through linear regression and calculate the R^2 value which is in this case essentially a measure of linearity. The R^2 value is 0.9995, which for this purpose is a nearly perfect fit, meaning the sensor response is linear for this test. Excel also provides an equation for the line where the slope of this line should closely approximate the sensitivity of the CTPS sensor. The slope gives the power detected by the CPTS for every unit power increase of the reactor. In this case the sensitivity is very close to 0.0006 watts of CTPS detector power per kilowatt reactor

power. Using this sensitivity, it would be expected that the CTPS would be seeing a deposited power of 0.27 watts at 450 kW reactor power, which is very close to what the raw data gives as the actual number.

The remainder of the planar #28 testing was run using the APC set to a gain of 590 and a set point of 439 corresponding to a resistance of 14.5 (which works out to a temperature of roughly 335 ^{o}C). Figures 4.3 to 4.7 show the results of the first test, which was designed to examine how sensor linearity would be affected by cycling the reactor power up and down with large power changes. To do this the reactor was stepped up from 0 kW to 30kW for 20 minutes, to 300kW for 15 minutes, then to 450 kW for 15 minutes. At that point the control rods were driven in (a large negative reactivity insertion) which quickly lowered the reactor output. As power reached 100kW the control rods were quickly withdrawn to raise power back to 300 kW and finally back to 450 kW.

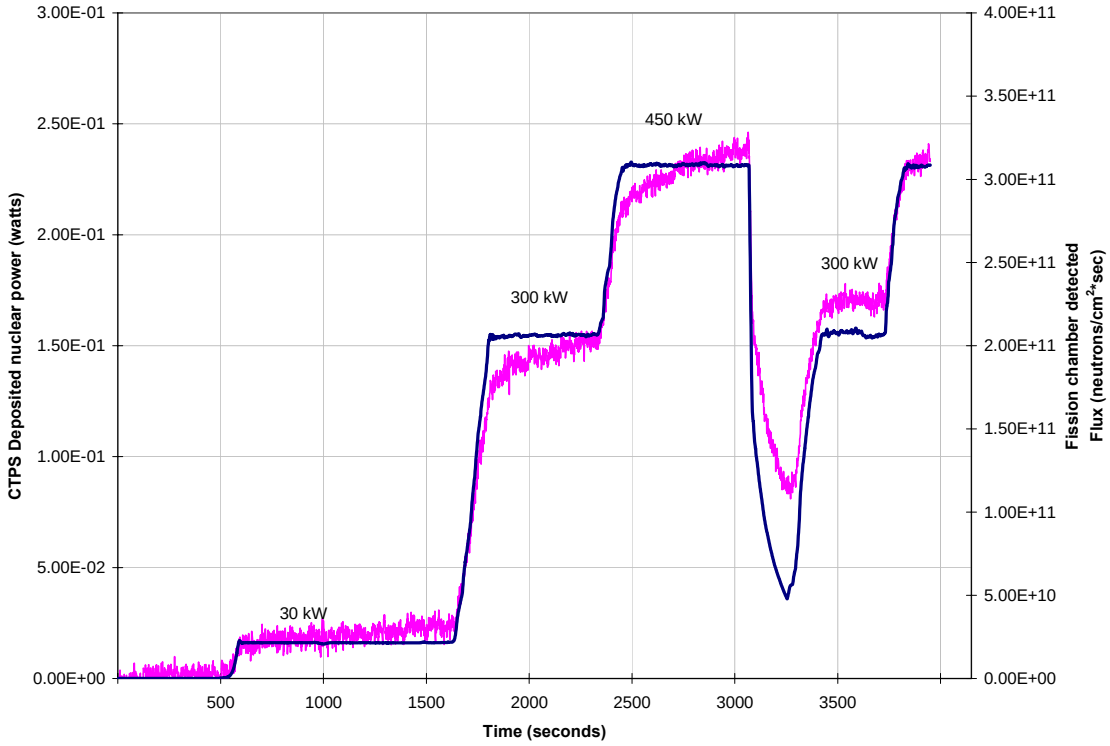

Figure 69: Planar CTPS and fission chamber response

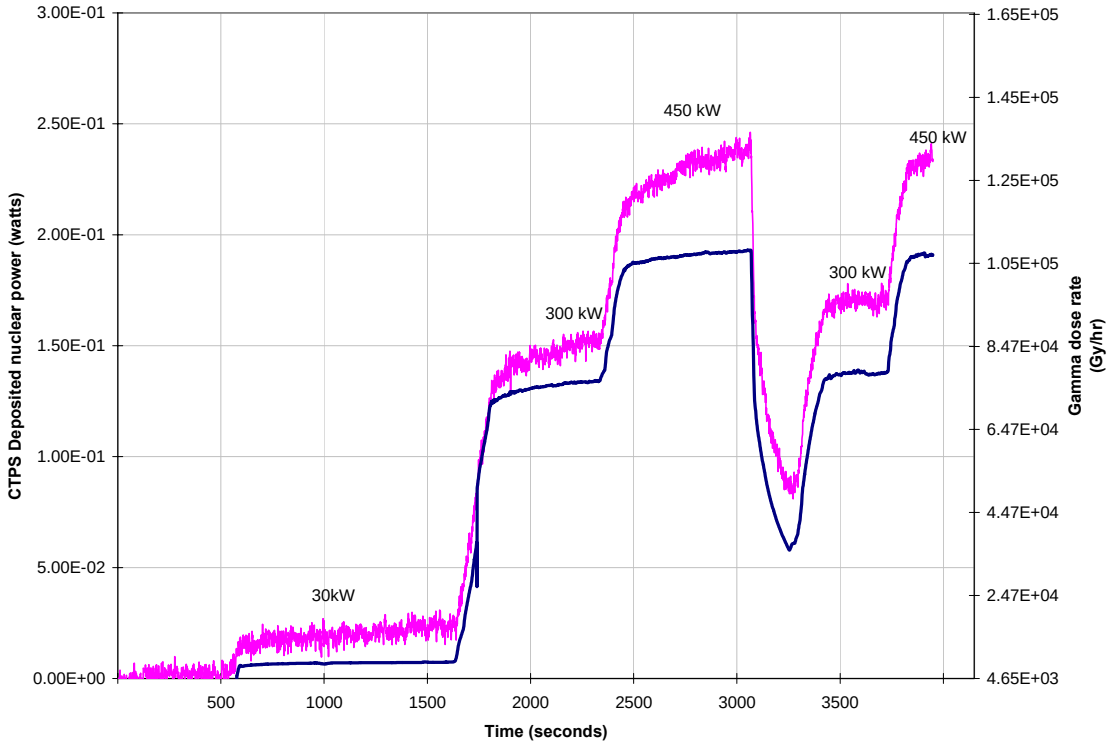

Figure 70: Planar CTPS and gamma sensor response

Figure 4.3 shows the CTPS and fission chamber response plotted together where the CTPS is plotted in watts, and the fission chamber signal is converted to units of flux (flux is the term for the number of neutrons incident on a square centimeter in a second). This conversion is accomplished using a conversion factor determined through testing of the fission chamber at the OSU NRL. Figure 4.4 is a plot of CTPS and gamma dose rate given in grays per hour. This conversion is done using manufacturer supplied calibration data for the gamma sensor. These plots give some very interesting information about the CTPS signal. The CTPS seems to respond nearly as fast as these other two sensors, but it shows a drift even at a constant reactor power. Taking this data and comparing the linearity of the CTPS to the fission chamber is interesting, as the fission chamber is reasonably well known to be linear.

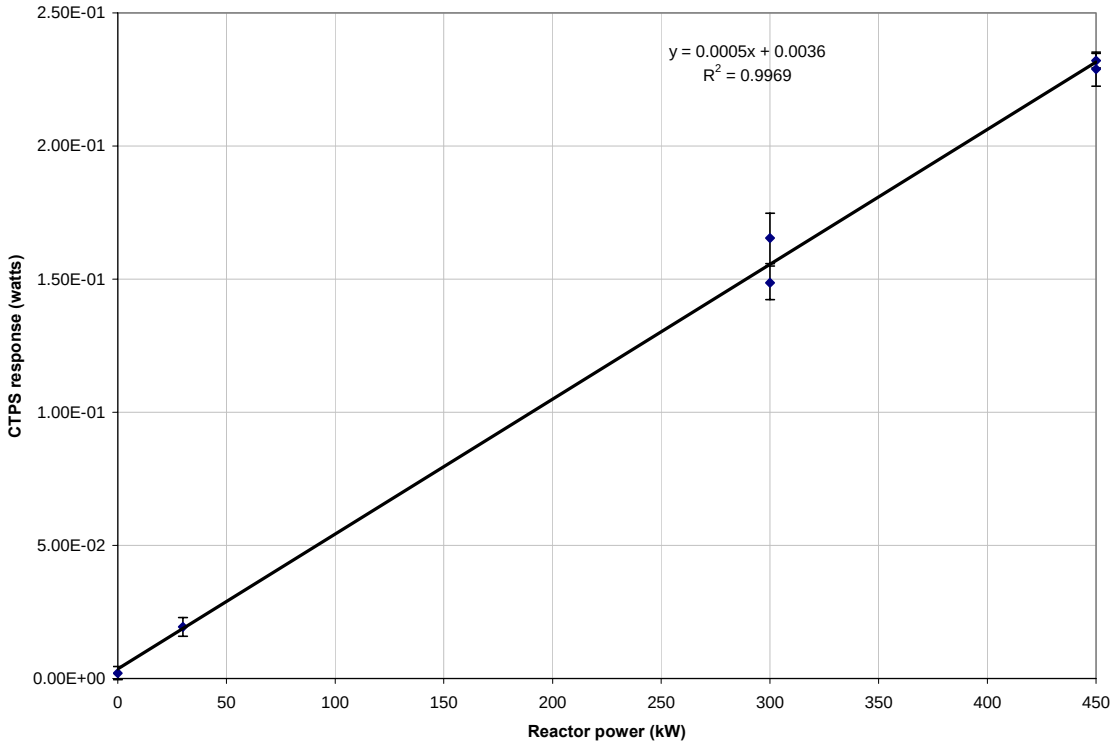

Figure 71: linearity plot for CTPS #28

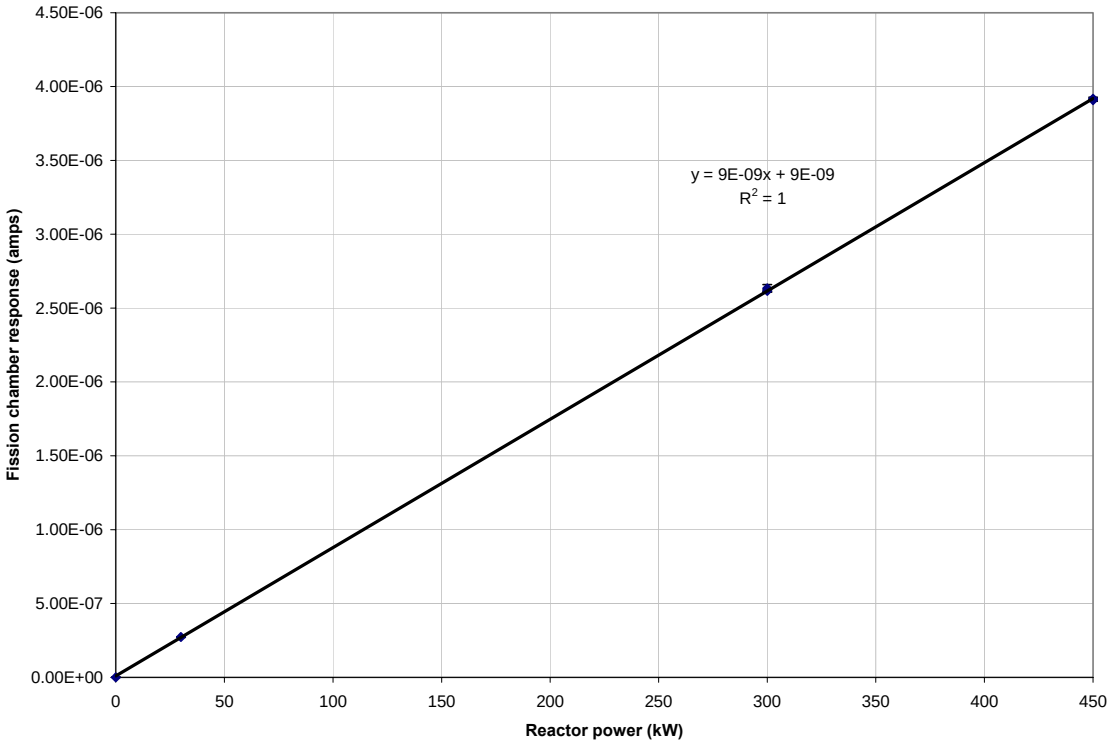

Figure 72: linearity of fission chamber

In figures 4.5 and 4.6, the CTPS and fission chamber responses are seen to be very linear, with the straight trend line a good fit to the data. Also, the sensitivity of the CTPS sensor is 0.0005 watts response per kW reactor power, which is inline with the previous number but slightly lower. This change is due to the use of a different controller with a different set point. In figure 4.5, CTPS shows somewhat strange behavior at 300 kW, with very different measurements at the first and second runs at that power. This is explained by the drift, as the second measurement at 300 kW is higher than the first. To attempt to explain this drift, it is useful to examine data from the thermocouples placed in the test loop. Figure 4.7 shows the change in temperature with time for all thermocouple positions in the sensor test loop. The top two graphs, which are the thermocouples located at the top and bottom of the sensor, show that temperature changes in a way that is consistent with the CTPS signal drift.

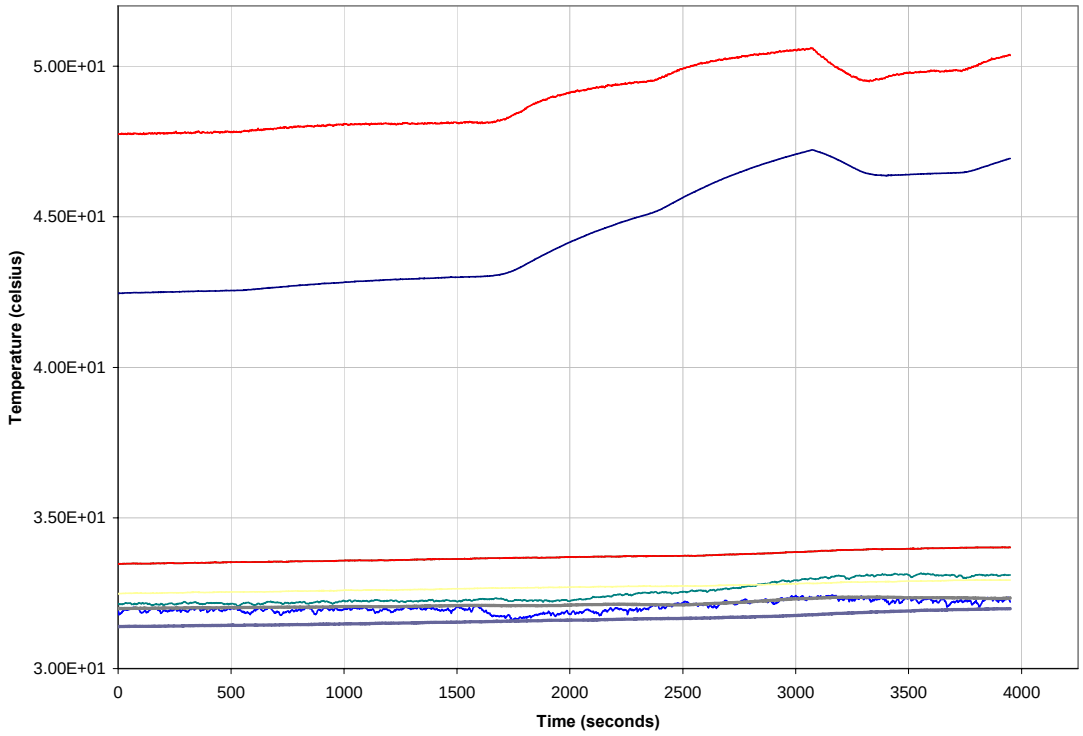

Figure 73: Test loop temperature data

A follow up to this run included the jumps from zero to 30 kW to 300 kW to 450 kW, to attempt to replicate the successful linearity test. Shown in figures 4.8 and 4.9 are the CTPS response plotted with fission chamber and gamma sensor respectively. Using this data, and excel to determine the R^2 value and sensitivity, effectively backs up the data from the previous run. The R^2 value is 0.9997, and the sensitivity is identical. An interesting feature of this set of curves is that the CTPS indicated power signal at 30 kW falls with time. As neither the gamma nor the fission chamber show a change in reading to explain this, it should not be related to either gamma sensitivity or neutron signal. Using the thermocouple readings at the sensor in figure 4.10, it is fairly obvious that the CTPS is tracking ambient temperature.

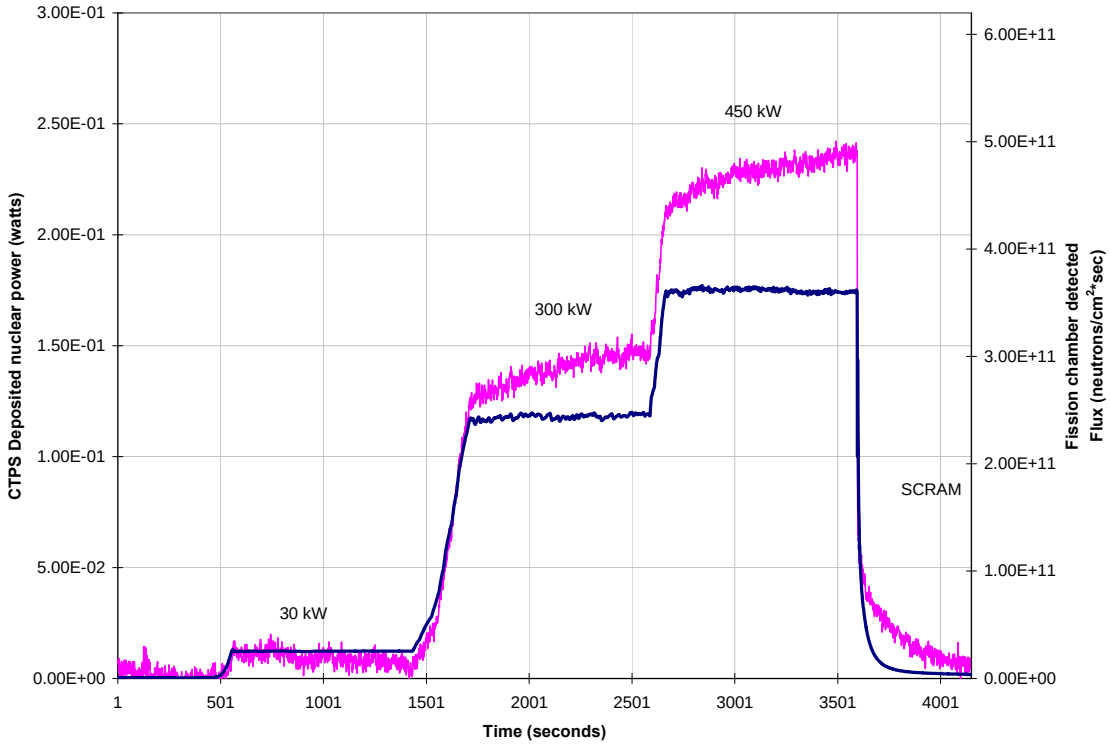

Figure 74: CTPS and fission chamber response

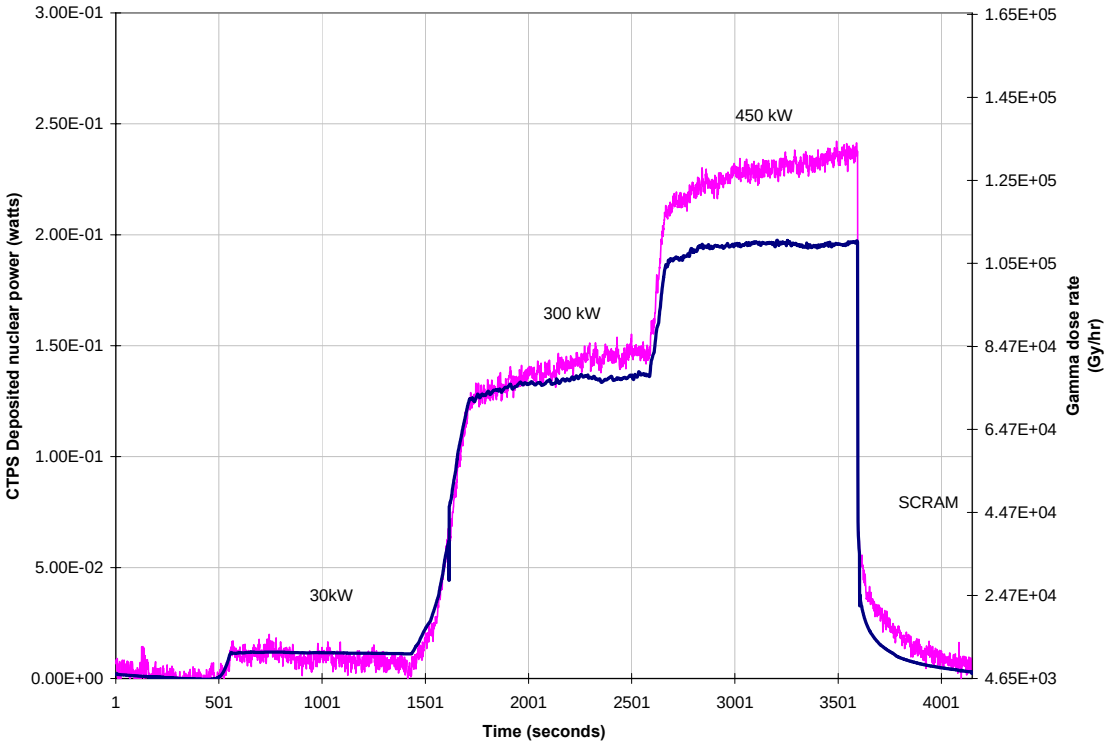

Figure 75: CTPS and gamma sensor response

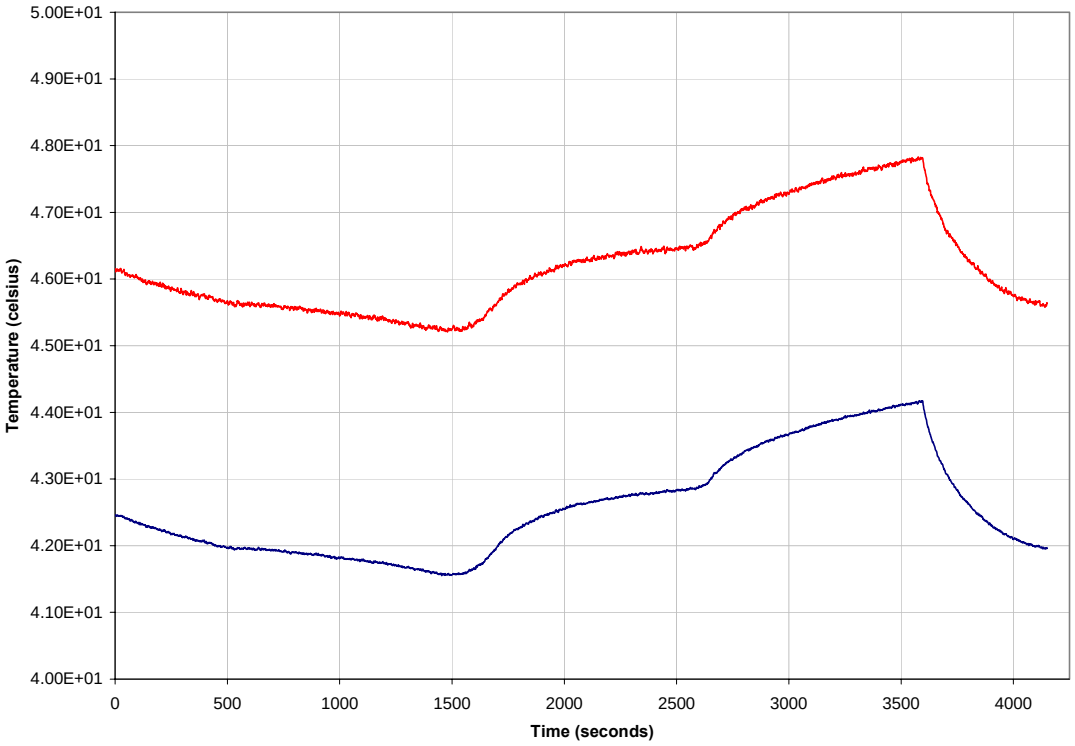

Figure 76: Sensor loop temperatures

That the sensor is changing with temperature is expected, and in fact desired, as the faster the thermal behavior of the sensor, the greater its bandwidth. Mode two operation was designed to continuously adjust for this drift so this indicates how important the digital controller would be to actual use of this sensor.

An additional run was made with planar sensor #28 for a lengthy period of time at high power to see if the sensor would reach equilibrium. This was done to rule out the possibility that a component of the drift is CTPS gamma sensitivity. Shown in figures 4.11 and 4.12 are the CTPS with fission chamber and gamma sensor. From this test it does not appear that the sensor is approaching equilibrium very quickly. If the drift were due in large part to direct gamma sensitivity, it would be expected that the sensor would show an approach to equilibrium well within the run time which was on the order of two hours at 450 kW.

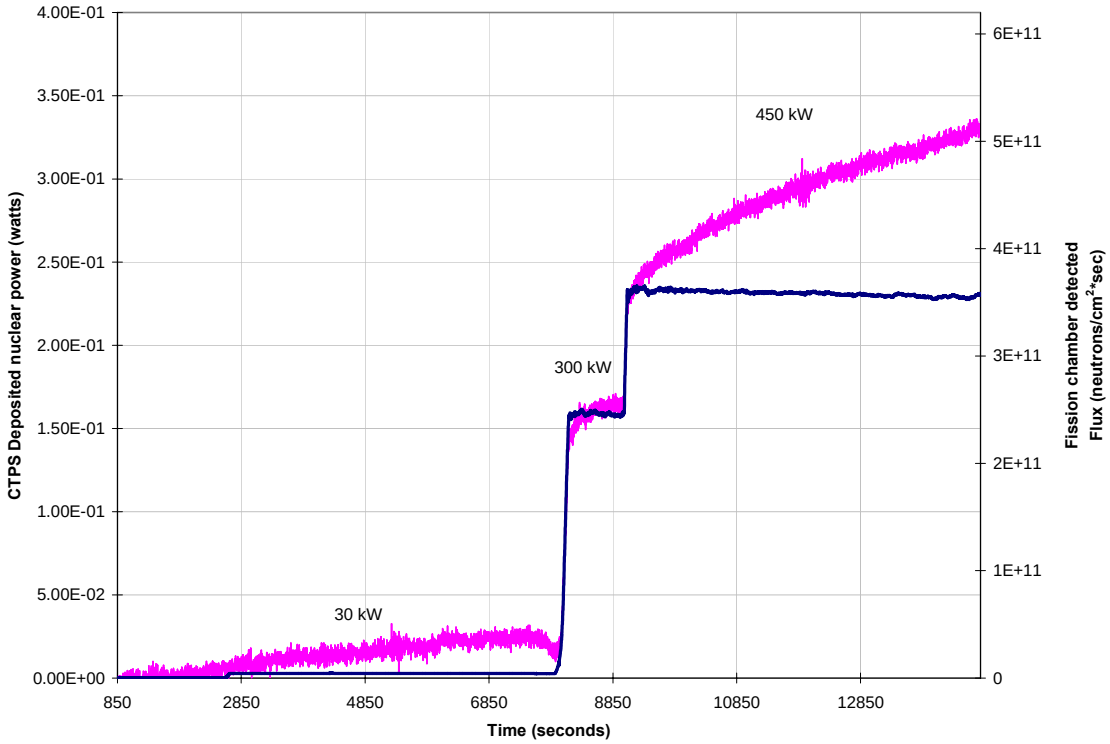

Figure 77: CTPS and fission chamber response

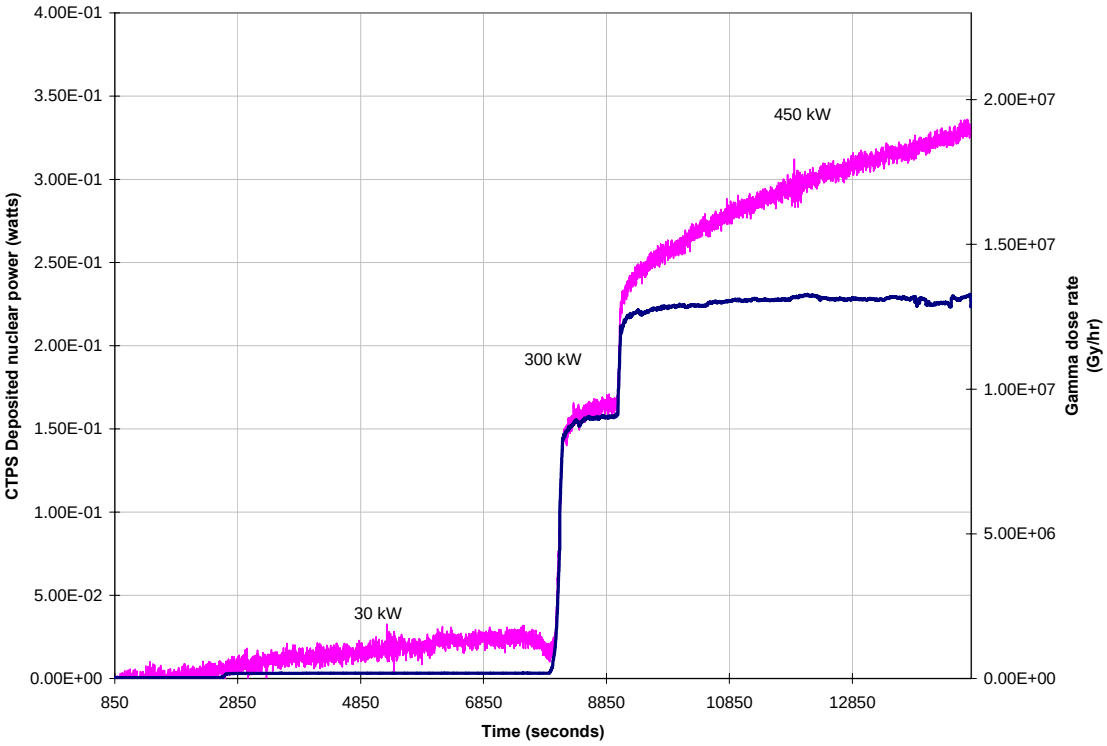

Figure 78: CTPS and gamma response

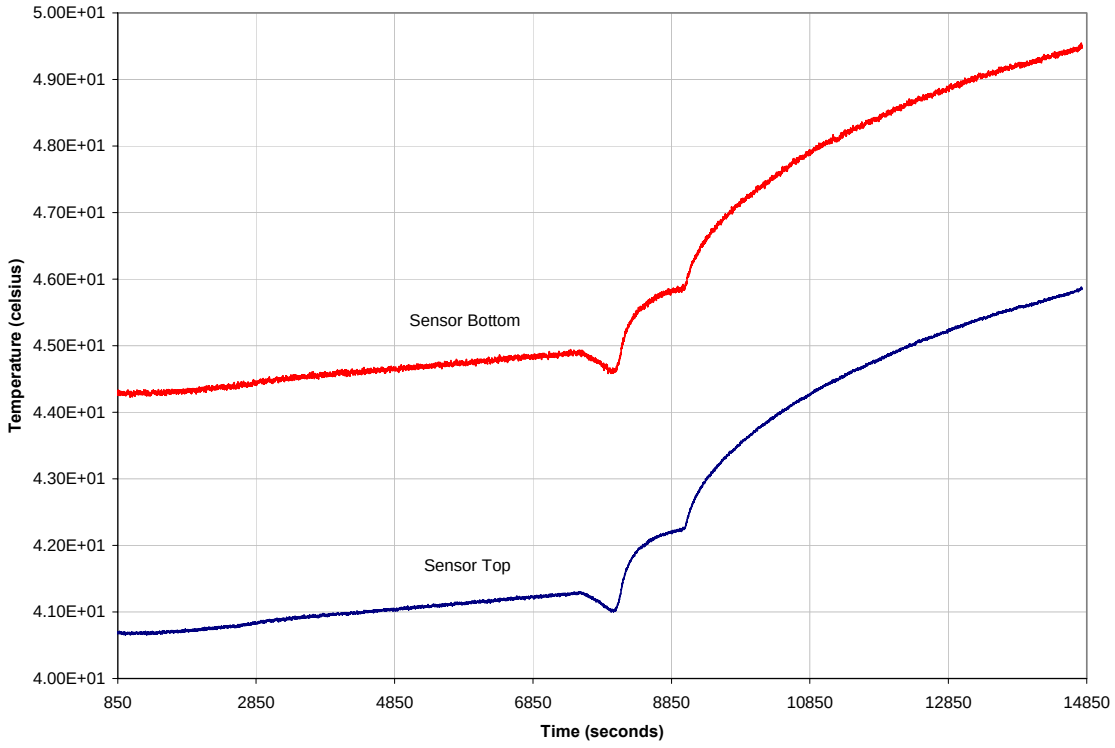

Figure 79: thermocouple temperature data

A look at figure 4.13, the thermocouple measurements, shows that they indicate temperature increase for the entire test. This run also shows good linearity on the order of the other tests, and sensitivity that exactly matches the earlier APC tests.

It is clear from the data presented here that planar #28 has linear characteristics that compare favorably with the fission chamber. The sensitivity at .0005 watts per kilowatt reactor power is a solid number based on the fact that it has been backed up by each test run with the sensor. The drift is a problem that was apparent in earlier testing, but it was expected that the mode two capability of the digital controller would automatically correct for it when this round of testing was being planned. This testing reinforces the hypothesis that the drift is a direct function of loop temperature increase, and is not due to non linear gamma sensitivity.

4.3 PLANAR SENSOR #28 BANDWIDTH

The evaluation of the sensor bandwidth was a more complicated task than was originally thought. The data was captured at 1 kHz for ten seconds, and though the oscillator was never run at more than 15 Hz there was a very large higher frequency noise component that obscured the data. This is not a problem for normal measurements because the normal data capture mode averages each second (1000 data points) and effectively cancels the high frequency component out. With the streaming data capture, there is no averaging. The figure 4.14 is the raw data for an oscillation at 2 Hz plotted as deposited nuclear power.

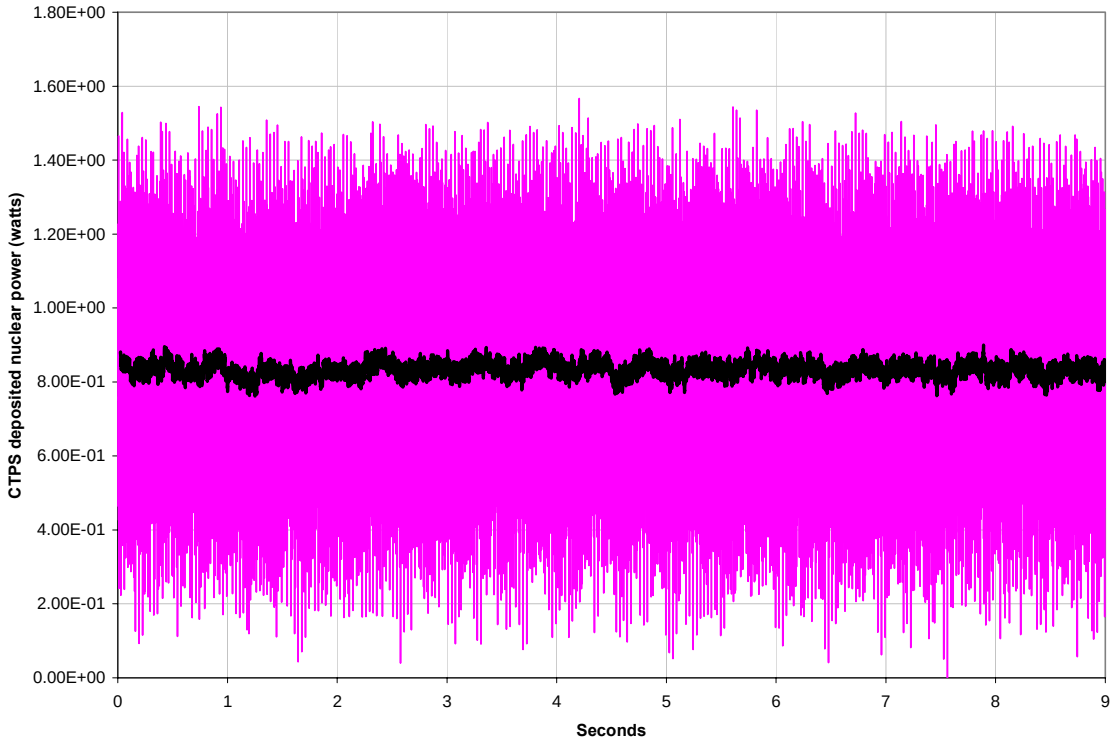

Figure 80: Planar #28 2 Hz oscillation

It is seen that the data is very noisy, but the moving average trend line shows that there is a hidden low frequency component that could be at 2 Hz. To look at the frequency components of a signal such as this it is normally converted from the time domain to the frequency domain. When this is done the frequencies that exist in this signal will show as peaks at the frequency corresponding to where they oscillate. To convert a signal such as this to the frequency domain, it possible to calculate the Fourier transform using a fast fourier transform calculation or FFT. An FFT makes the calculation of a fourier transform a far less calculation intensive task than it otherwise would be. To do this, the software Matlab was used because of its ability to deal with very large matrices. Matlab scripts were written first to plot the FFT of the CTPS signal, which gave plots like the following at one Hz. In figure 4.15, the one Hz peak is completely obscured by the large noise signals at sixty Hz and its higher order harmonics. It is clear why the signal in the time domain was obscured, being hidden among the higher amplitude noise. Figure 4.16 shows a close up of the one Hz peak; note that the sixty Hz peak is several orders of magnitude larger. Of special significance is that very little noise is present between the one and sixty Hz peaks. Since the data is easily manipulated in Matlab, the most useful step is to low pass filter the data to remove the higher frequency signals. This accomplished using another Matlab script (all Matlab scripts are included in appendix A), and the resulting FFT plot is shown in figure 4.17. This plot shows that all of the higher frequency components have been removed, even though there is still some noise near the one Hz signal, it is possible to plot the original CTPS response to the oscillation. This plot is shown in figure 4.18 with a perfect sine superimposed on the noisy CTPS signal. The CTPS signal is noisy looking because the slightly higher frequency components are combining with the sensor signal. The clean sine wave is based on the RMS value of the CTPS signal, and should very nearly approximate what the CTPS would look like without any noise. Calculating the RMS value of the CTPS signal is also important because it allows a comparison of relative signal strength across the test frequency range. By calculating the RMS value of the filtered CTPS signal for each oscillator test frequency, it is possible to determine the maximum bandwidth of the sensor. This is because as the frequency of oscillation passes the frequency at which the sensor responds,

the magnitude of response decreases rapidly. So determining at what frequency the sensor response begins to drop in magnitude is key.

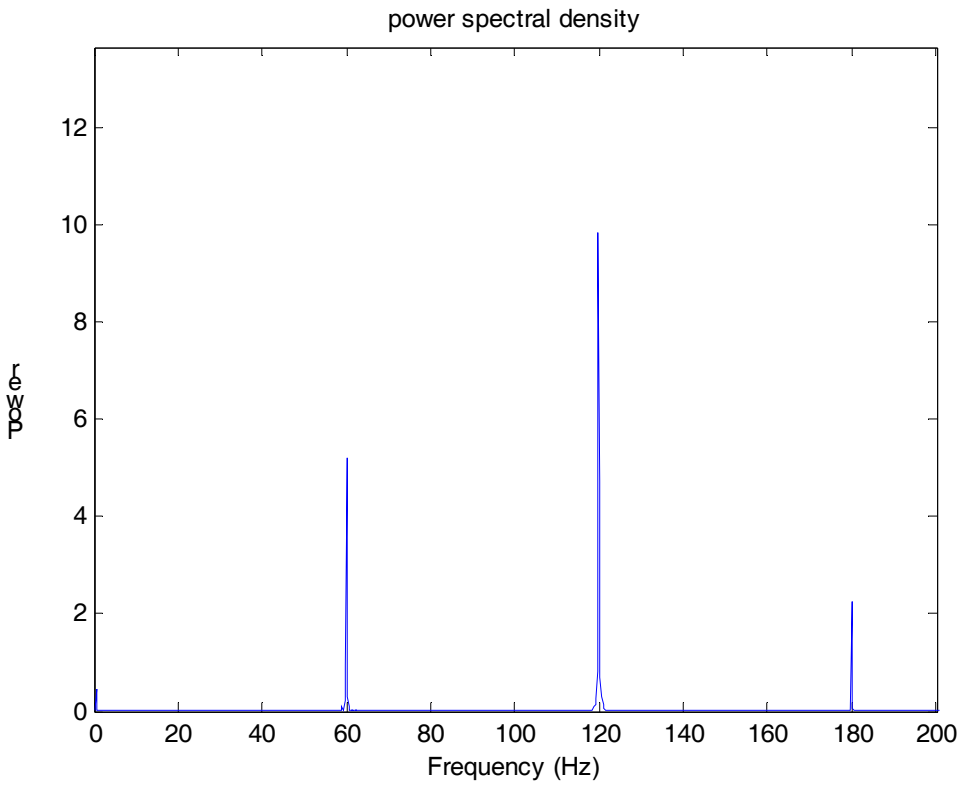

Figure 81: PSD plot of oscillator at 1 Hz

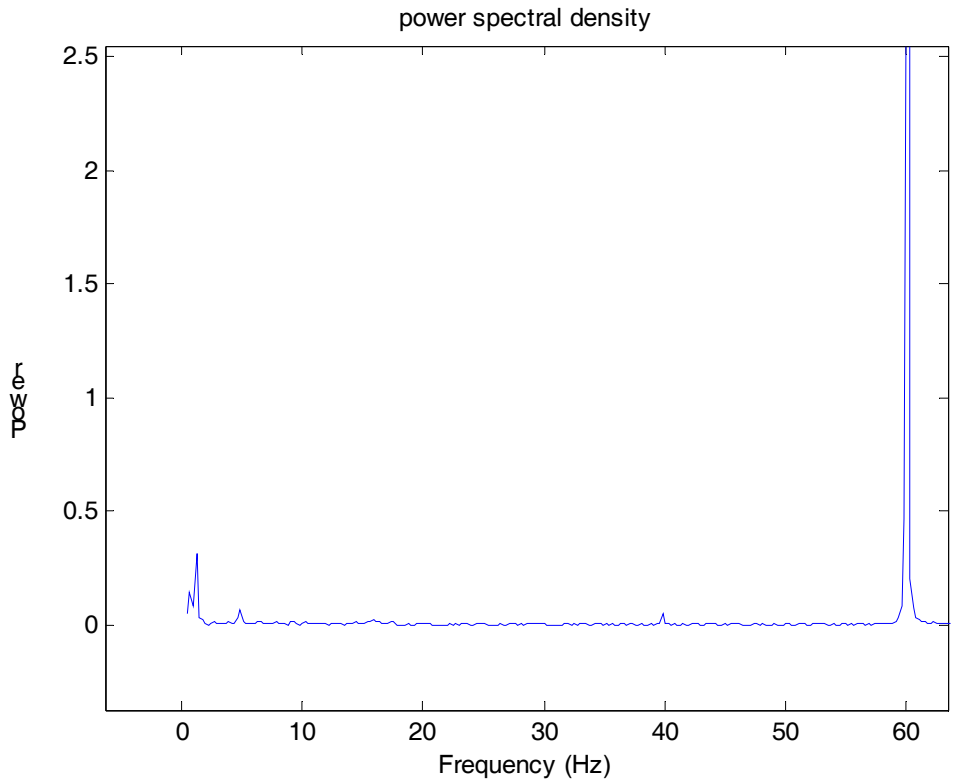

Figure 82: closer view of 1Hz peak

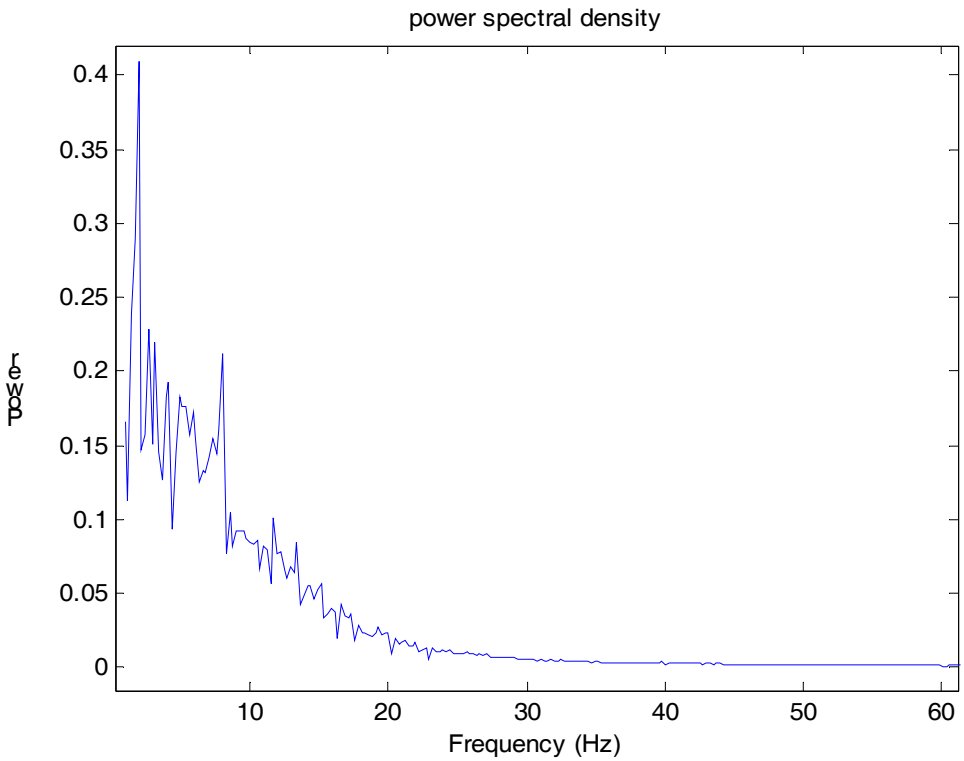

Figure 83: FFT of filtered signal showing drop off

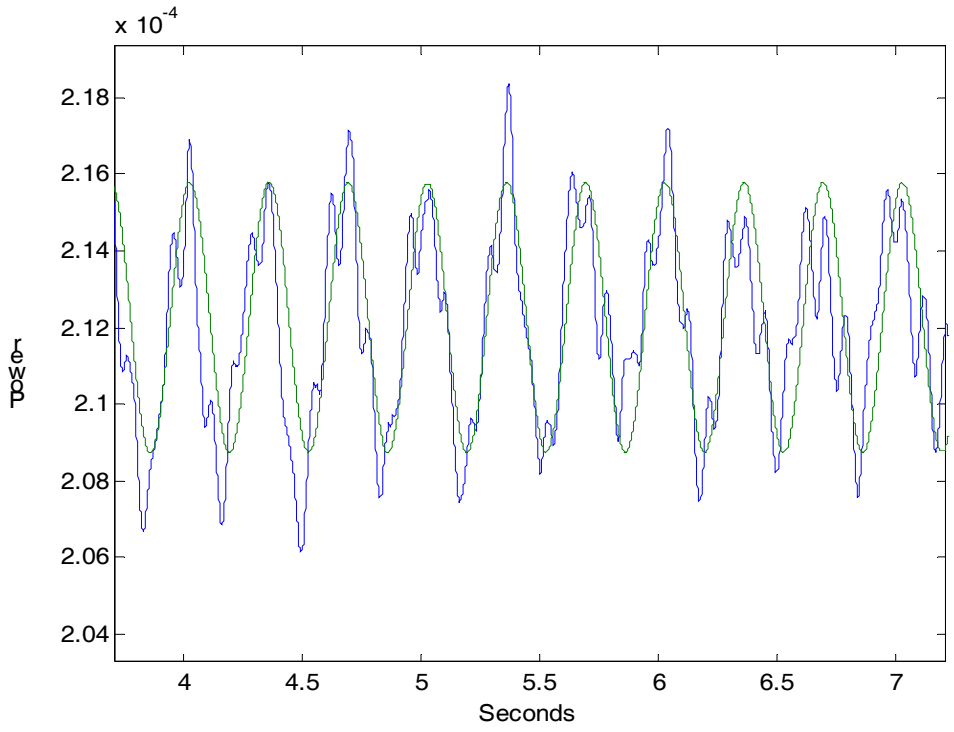

Figure 84: filtered CTPS response (blue) with sine wave superimposed (green)

The RMS calculation is used, the units of magnitude are converted to dB by use of the equation $dB = 20\log_{10}(\sqrt{P})$ where P is power normalized to the initial value for the lowest oscillation frequencies (this allows the plot to start from the origin). If these values are then graphed versus the frequency of oscillation, it is possible to plot the frequency response and determine the maximum bandwidth. Maximum bandwidth is defined here as the frequency at which the magnitude falls off three dB, this plot is shown in figure 4.19. As can be determined from this figure, the maximum bandwidth has been calculated as 3.6 Hz, although the twenty dB per decade fall off is indicative of a first order system, so the useable bandwidth may be higher.

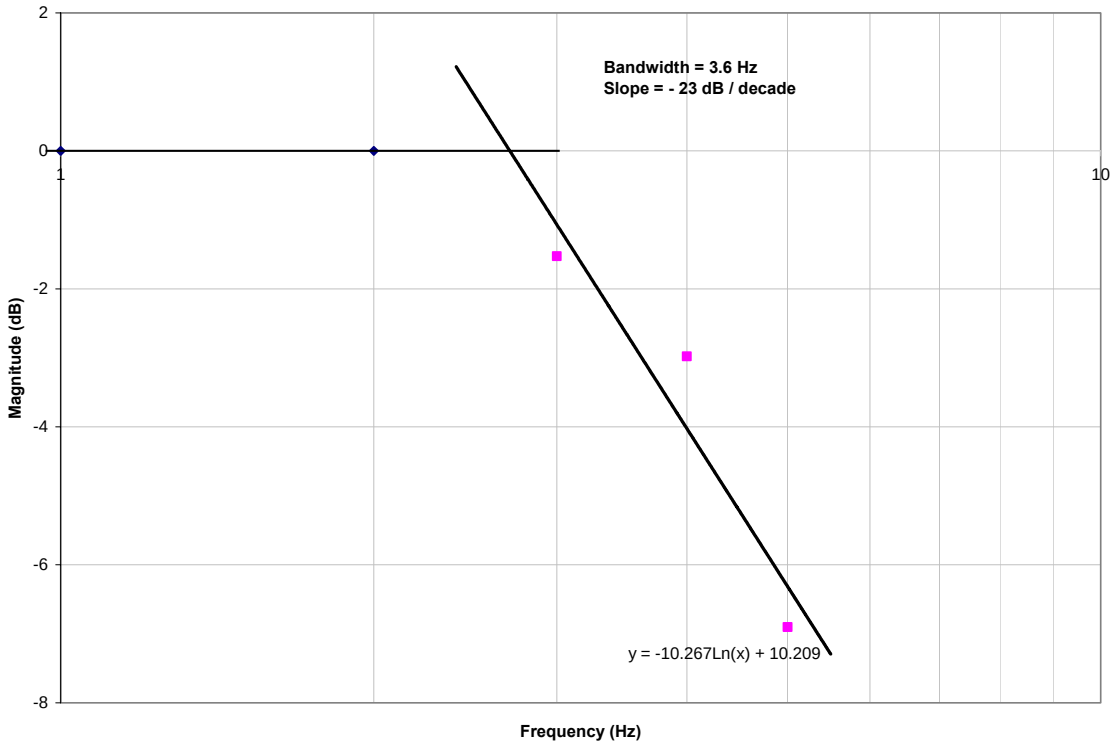

Figure 85: Frequency response of planar #28

4.4 CYLINDRICAL SENSOR #1 EXPERIMENTAL EVALUATIUON

The cylindrical CTPS sensors are designed to have completely different thermal dynamics, so the PID control was tried to see if there was any improvement in its function, there was not. The APC was therefore used exclusively, and tuned for a gain of 600 and a set point of 695 which corresponds to a resistance of 20 ohms. The first run to be examined was a test similar to those for the planar sensor #28 in that linearity was tested with measurements at 0 kW, 1 kW, 10 kW, 30 kW, 100 kW, 300 kW, 450 kW with each being held for about fifteen minutes. This test differed from the tests of the planar sensor because the blower was allowed to run for approximately twelve hours (overnight). The blower adds a significant amount of heat that causes the loop temperature to rise with a time constant of several hours. By running the loop overnight it was thought the temperature drift seen in the earlier tests might be avoided by

eliminating the possible cause of the temperature drift. Indeed, the zero power drift seen in earlier tests (for which loop heating was the only explanation) was eliminated. But as can be seen in the following figures, the drift at power was not eliminated. In fact the cylindrical sensor seems to be more affected by a change in heat transfer coefficient. This makes sense knowing that the cylindrical CTPS has been shown in simulations to have a greater bandwidth than the planar sensor due in part to its faster thermal dynamics. It is clear from the plots of CTPS with both fission chamber and gamma sensor that the drift is not due to reactor power drift, and it is also not likely due to change in gamma signal.

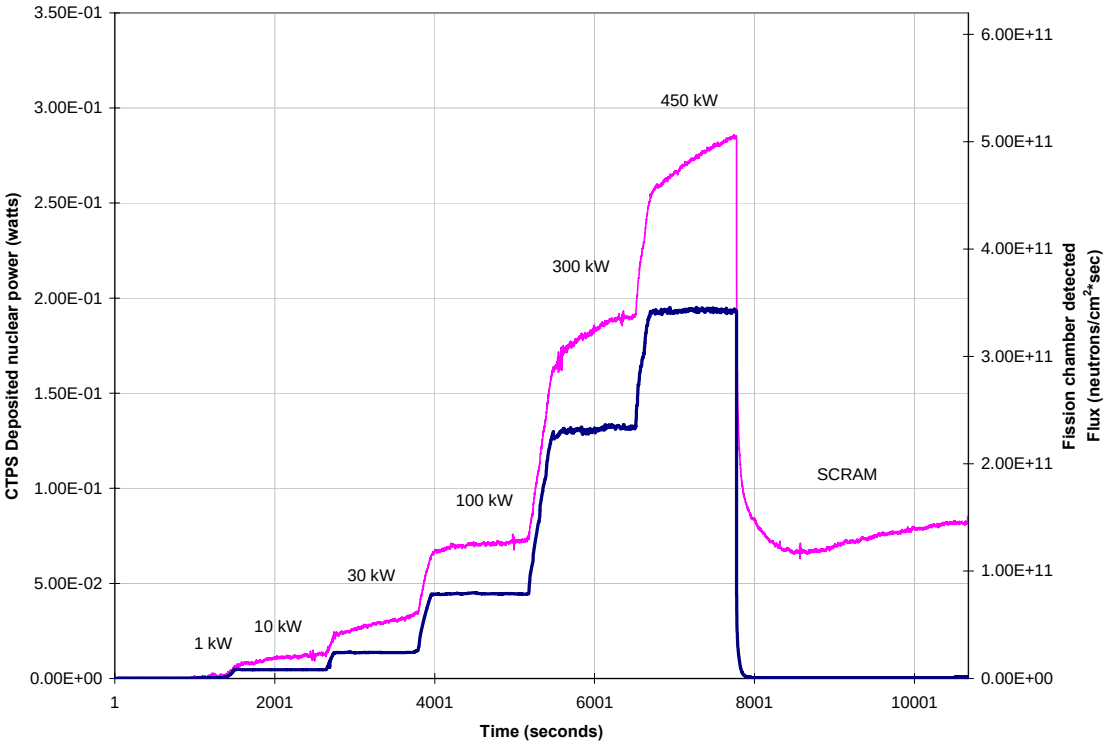

Figure 86: Cylindrical #1 response with fission chamber

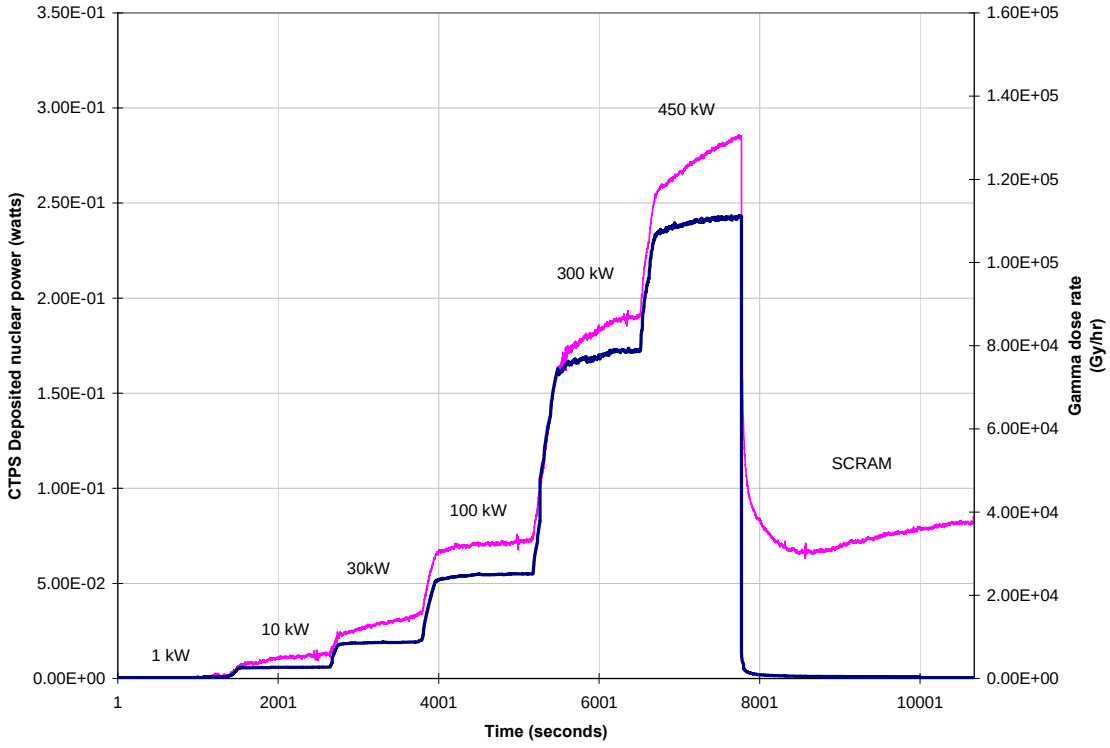

Figure 87: CTPS response with gamma sensor

The plot of linearity for the cylindrical CTPS shows it to be linear with a R^2 value of .9964 which is comparable to that of the planar sensors. The sensitivity of 0.0006 watts per kW reactor power is comparable to the planar sensor. Comparable sensitivity is expected due to the fact that uranium loading is roughly the same for both types of sensor.

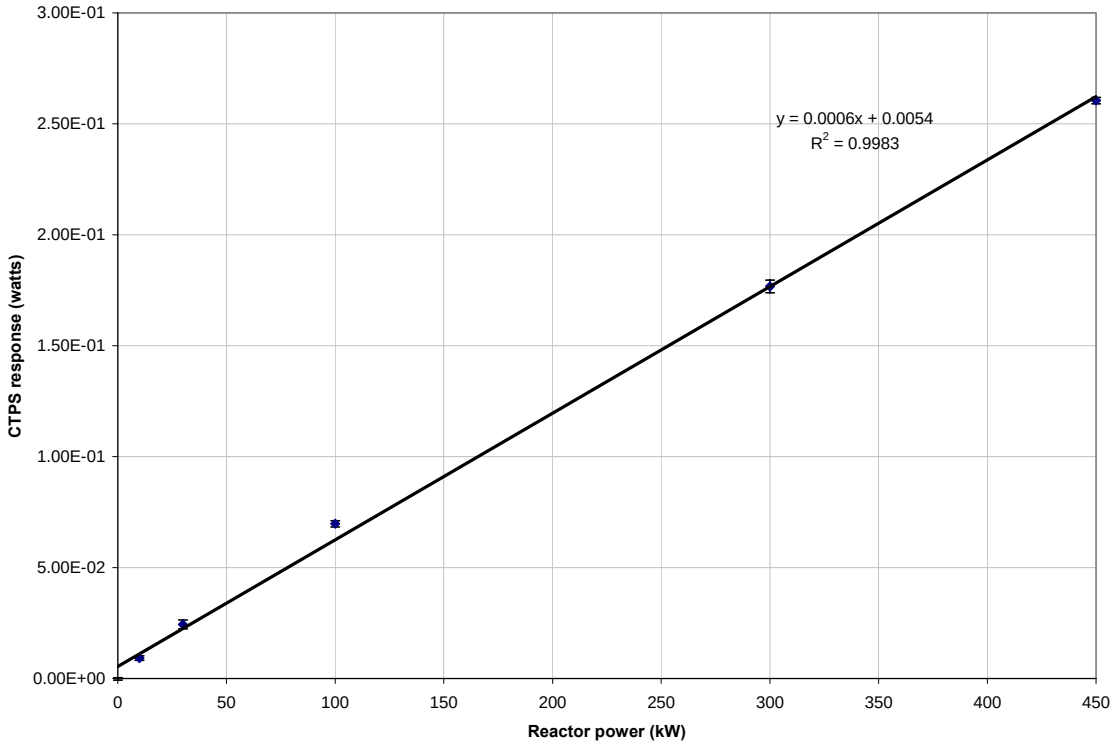

Figure 88: linearity and sensitivity for the cylindrical CTPS

Looking at figure 4.23 it is even more apparent that the CTPS drift is caused by some combination of factors, most likely dependent on the loop temperature. The odd behavior at 100 kW where the CTPS drifts less than at 30 kW is also explained by looking at the thermocouple data.

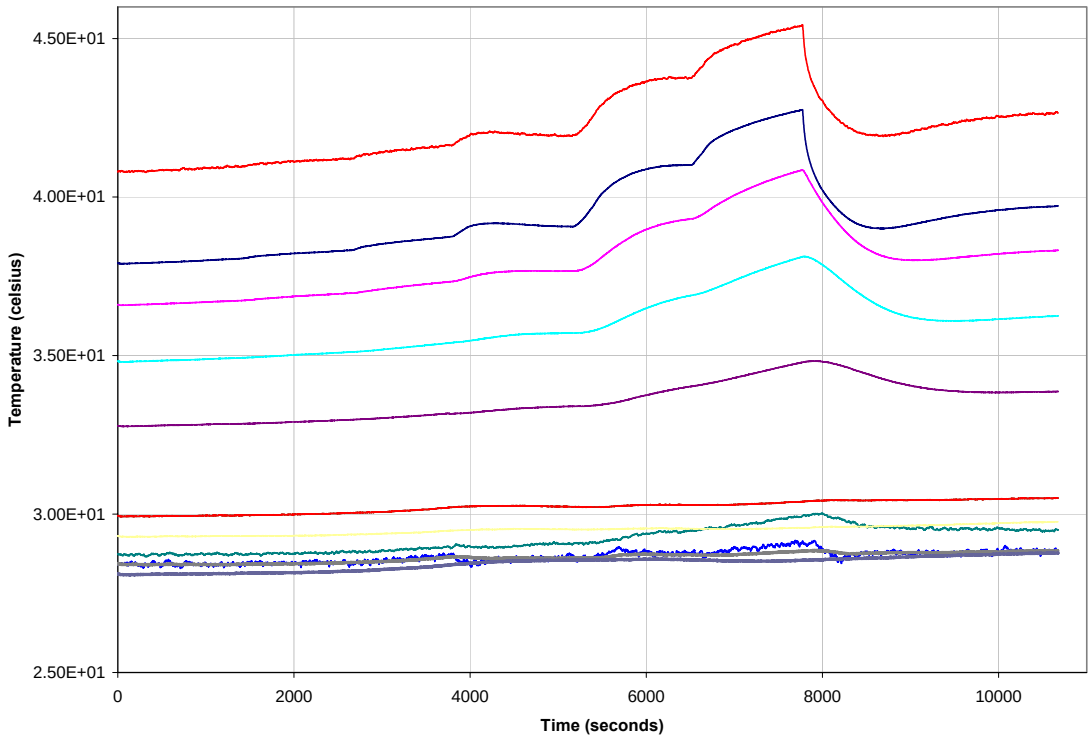

Figure 89: Thermocouple readings for cylindrical CTPS #1

The possible explanation for the loop temperature drift is that it is caused by gamma heating in the loop heat element, which was not running for the previous runs, but does contain a large amount of nichrome wire through which the air must flow. Even though the heater was not energized, it could have been heated sufficiently by the intense gamma field to increase the loop temperature.

Based on this theory for the temperature drift, it was decided to use the loop heater to raise the loop temperature above what it could possibly reach even at high power. A person would then lower heater power based on the temperature of the thermocouple closest to the sensor (TC 9). In this way it is possible to maintain the loop temperature constant. As the loop began to rise in temperature, the heater was dialed back slightly to offset the change. The thermocouple data in the following figure demonstrates

how successful this was in practice as the thermocouples closest to the sensor did not drift significantly.

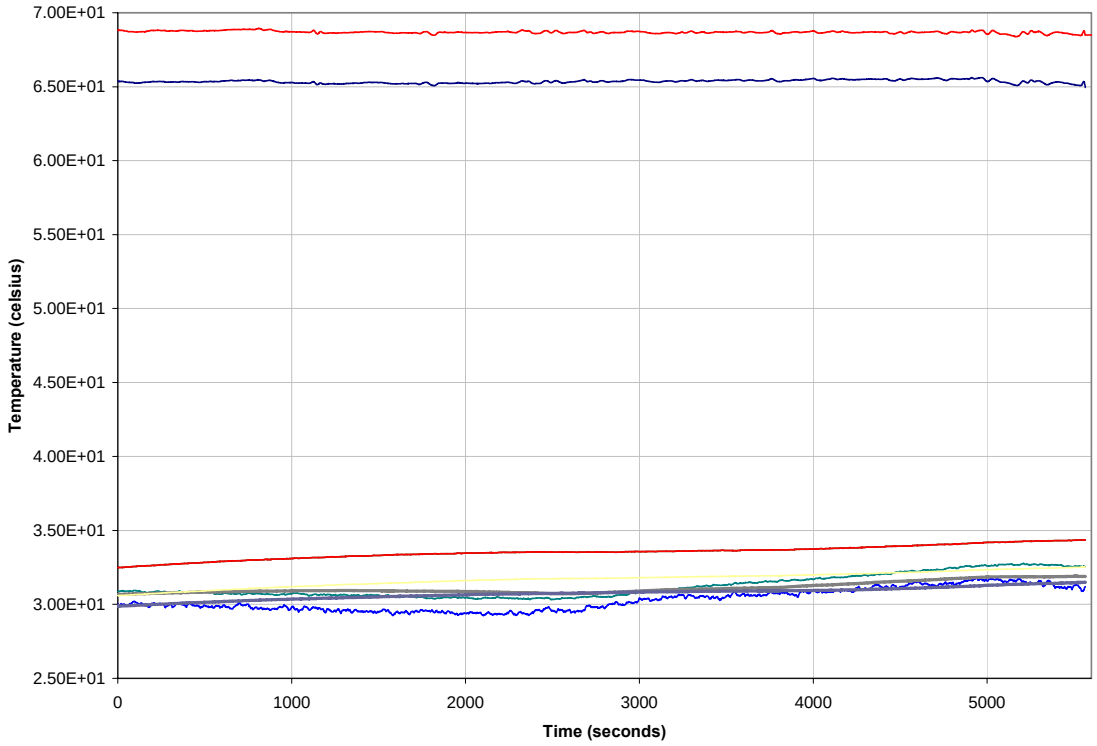

Figure 90: thermocouple reading for controlled temperature test

And as can be seen in the following figures, the CTPS seems not to have drifted with loop temperature remaining constant. The response is very close to that of the fission chamber, and instead of seeing the CTPS react to a reduction of power by settling to an indicated power greater than the initial, it is clear that the CTPS responds quite correctly. This is the type of operation envisioned with the digital controller running with mode two operation enabled. The mode two component was designed to adjust sensor response to counter a change in heat transfer coefficient. The net effect is the same here except the heat transfer coefficient is controlled, instead of having sensor compensation adjust for a changing coefficient.

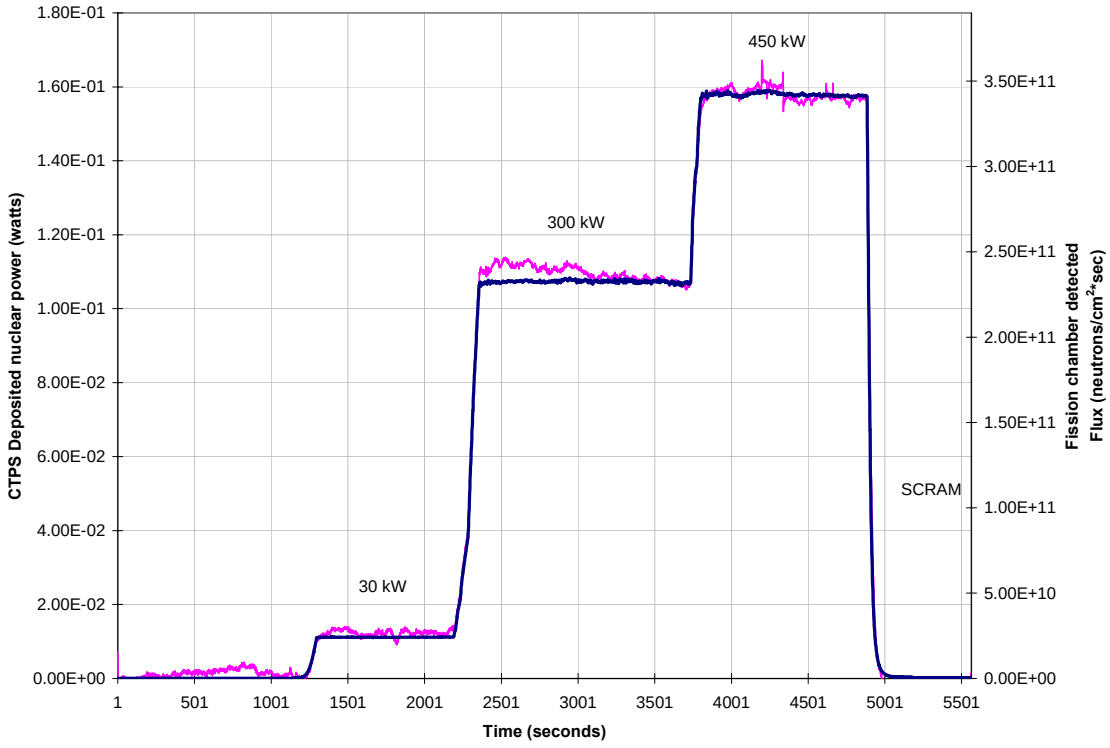

Figure 91: CTPS constant heat transfer coefficient with fission chamber

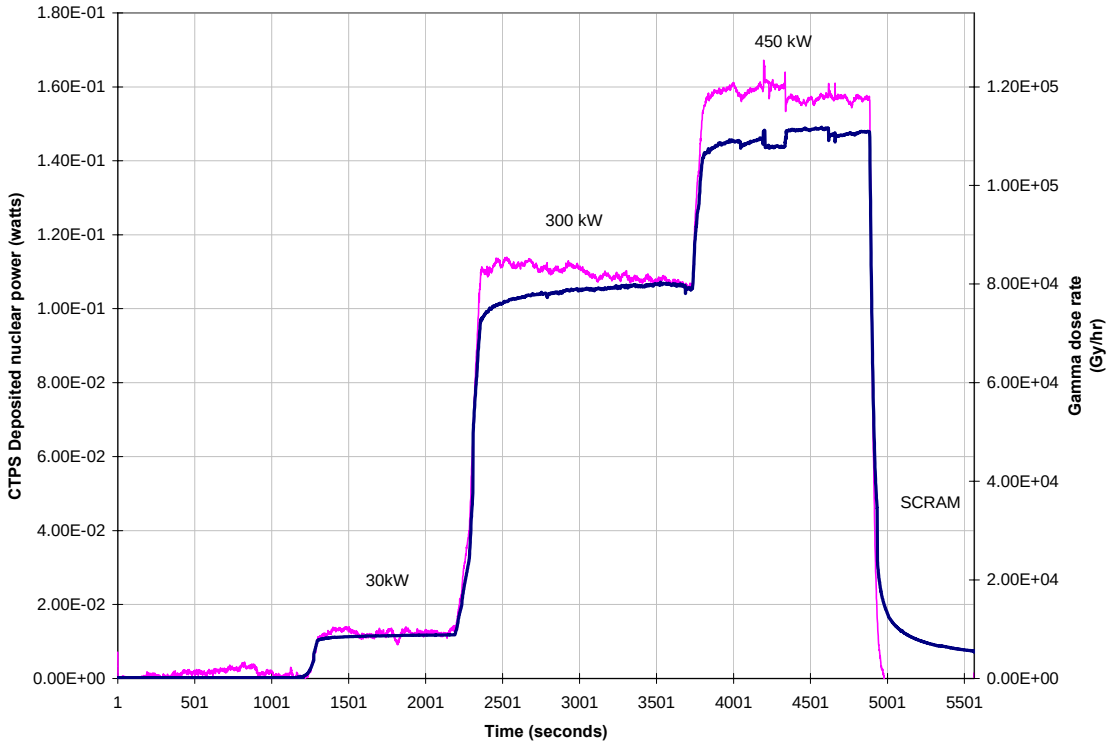

Figure 92: CTPS constant heat transfer coefficient with gamma

This performance is as expected, and again indicates that the CTPS drift is due to a change in heat transfer coefficient. The drift is the only serious issue facing this generation of sensor, so if the digital control could be used to allow active compensation for the change in heat transfer coefficient the sensor should be fully functional. The plot of CTPS response has two interesting features, the first is that indicated power drops at 300 kW, the second is the noisy signal at 450 kW. The first is difficult to explain, the temperature does decrease, in that time range, but not much. The noise is consistent with noise experience when the overhead hoist is used during measurements. This was experienced several times and tested in an experiment designed to identify sources of noise in an attempt to make the PID controller useable.

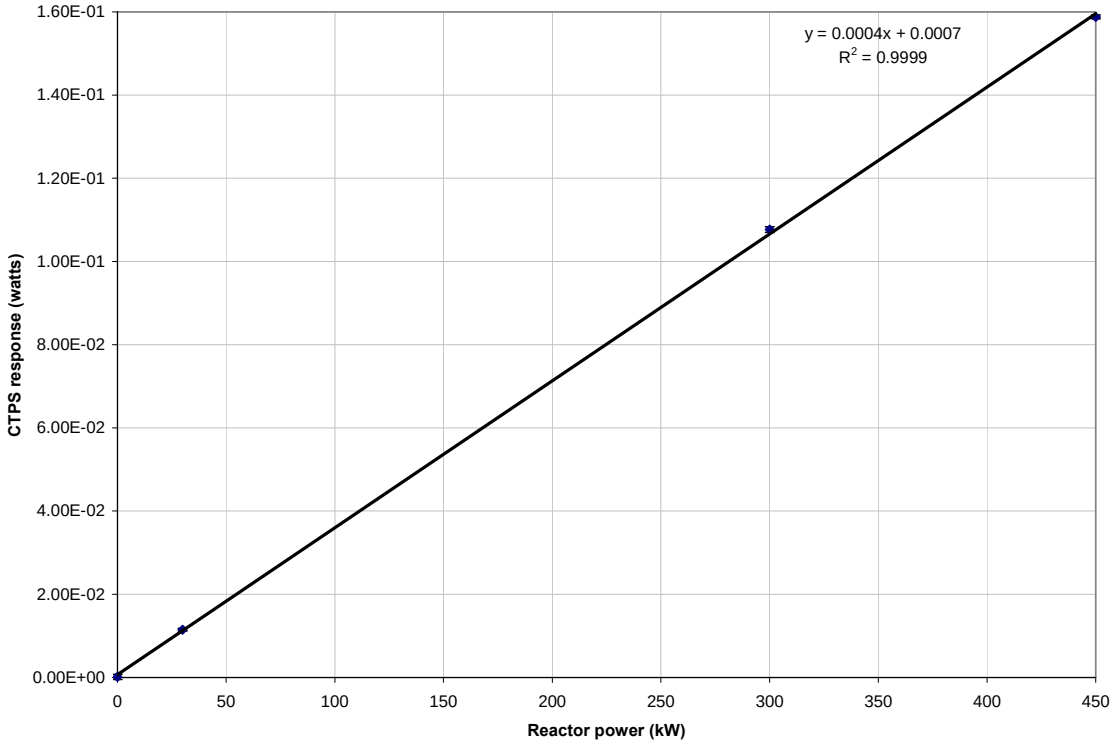

Figure 93: CTPS linearity curve for constant heat transfer coefficient

The linearity is extremely good for the sensor during this test as the R2 value is 0.9999 or almost a perfectly linear fit. The sensitivity is lower than in previous tests at 0.0004

which is a loss of about 20% of sensitivity. Neither of these are a surprise though, as the reduced heat transfer as a result of the increased loop temperature masqueraded as deposited nuclear power.

4.5 Cylindrical sensor #1 bandwidth

Using the oscillator to determine bandwidth for the cylindrical sensor required the same procedure as for the planar sensor. The raw data was similarly noisy for the cylindrical sensor as seen in figure 4.27. The moving average trend line once again suggests that there is good frequency information hidden in noise. The process for getting the filtered data is the same as previously used for the planar sensor.

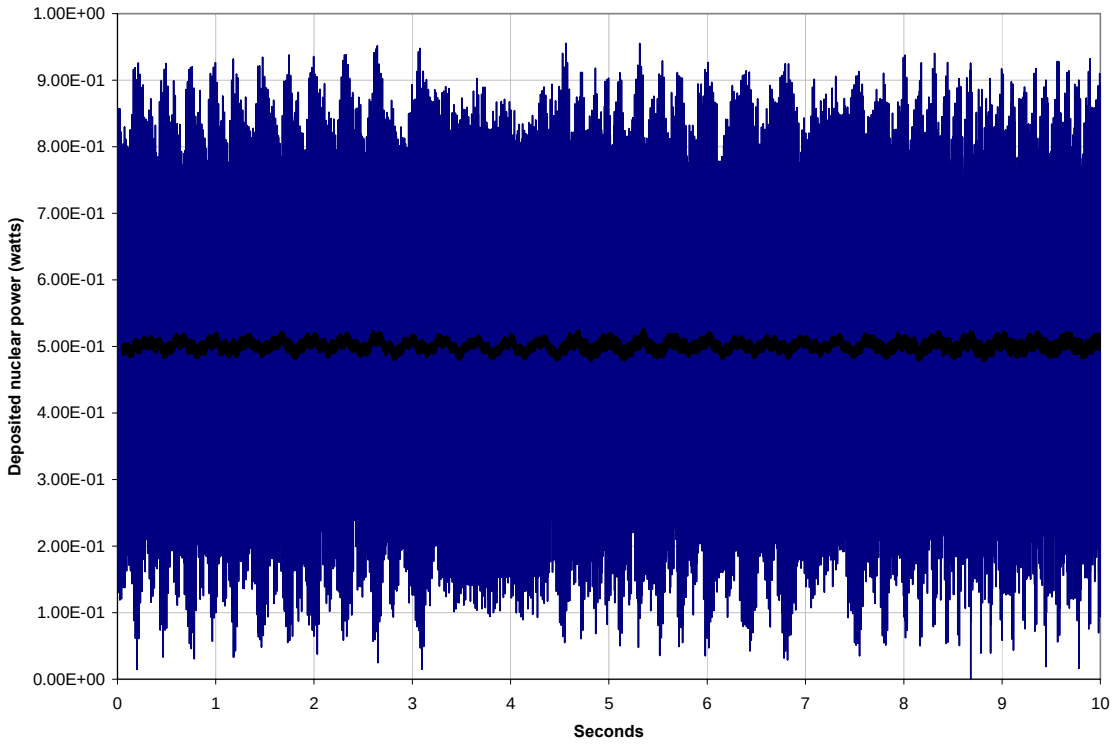

Figure 94: Cylindrical #1 oscillator response

In this figure it is easy to see the three Hz signal once a moving average is plotted. Taking the FFT and plotting it as before gives figure 4.28, the power spectral density plot. This figure shows again that there is extensive noise at sixty Hz and the peak at its harmonics. Filtering the data gives the plot shown in figure twenty eight, and graphing that filtered data gives figure twenty nine, which also has the same overlaid sine wave

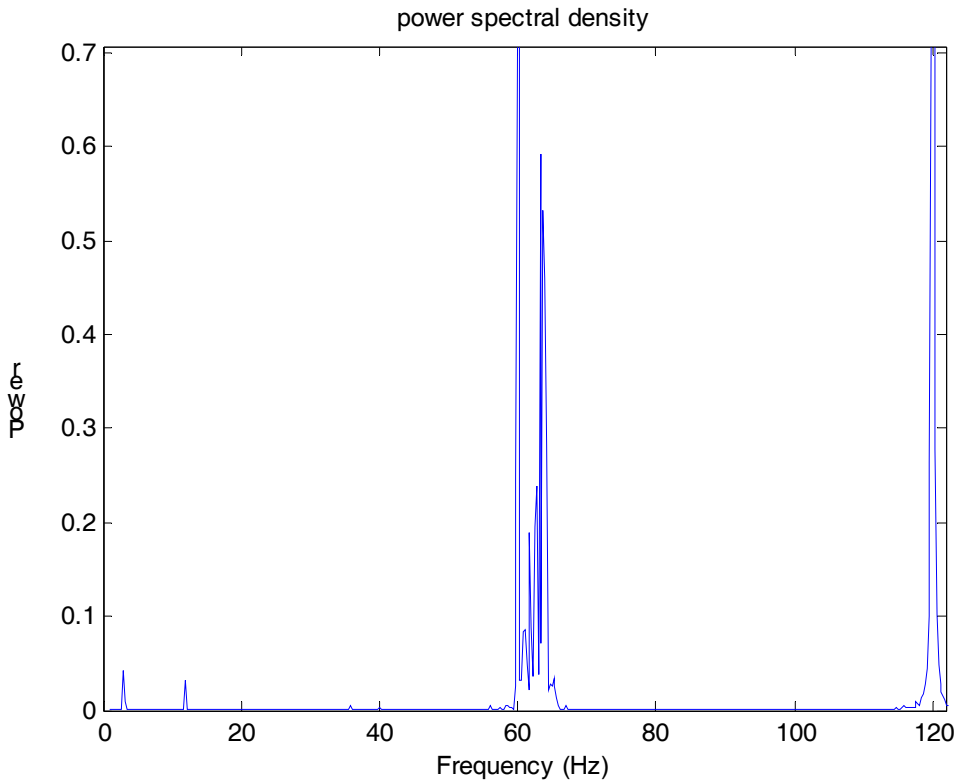

Figure 95: FFT plot of three Hz oscillator for cylindrical CTPS #1

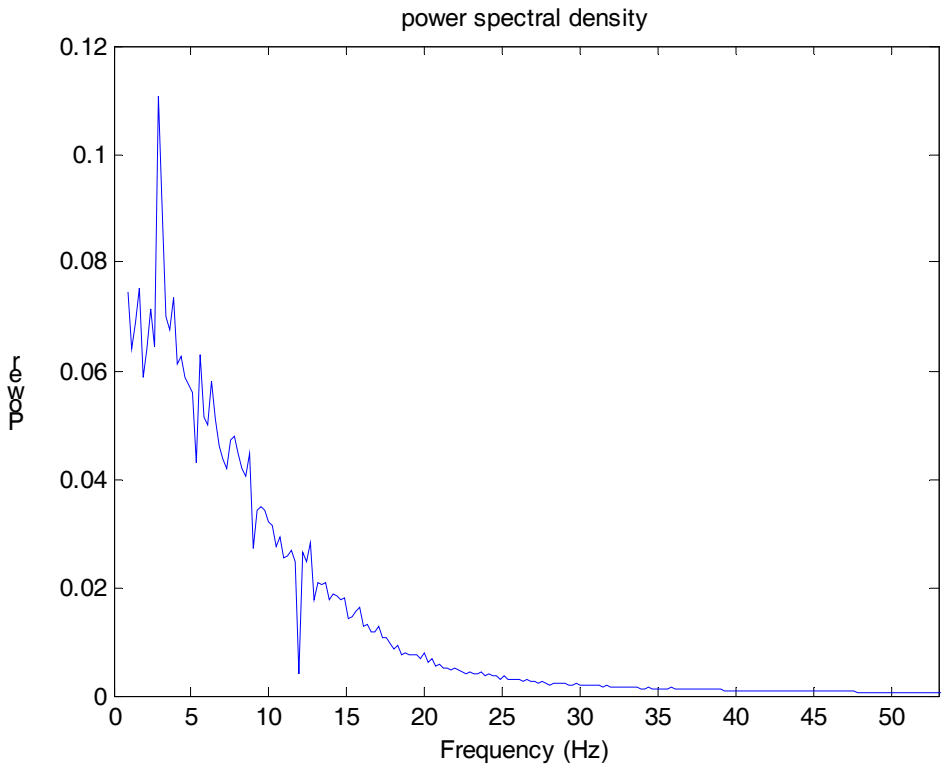

Figure 96: filtered three Hz oscillation

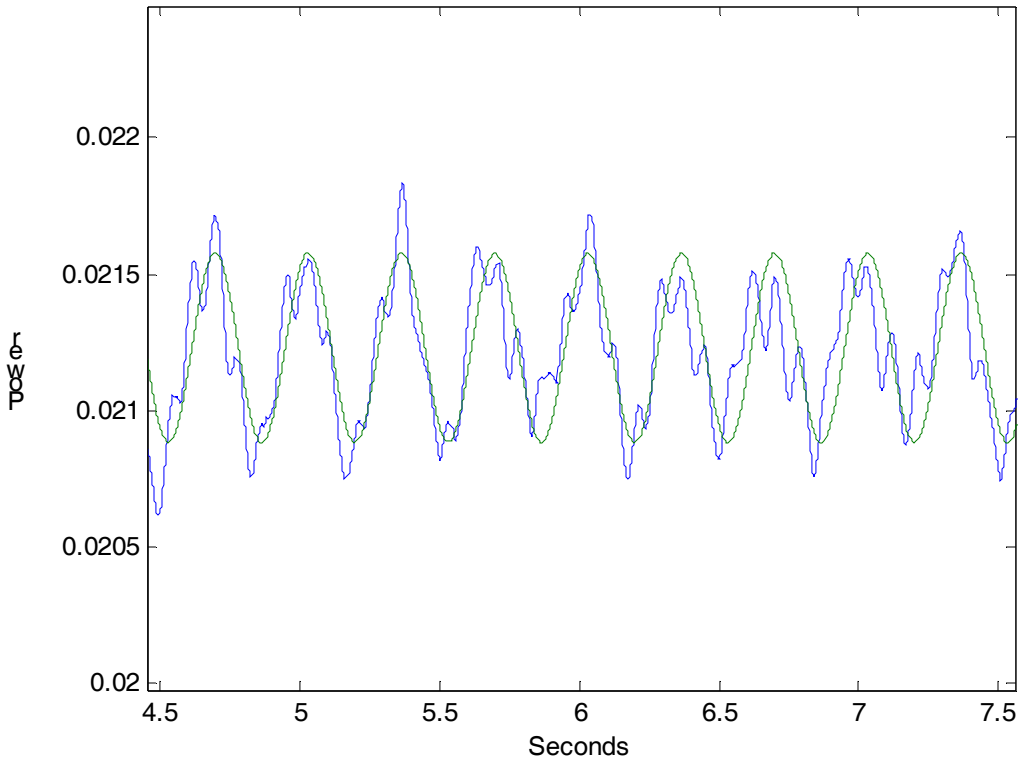

Figure 97: filtered sine wave with overlaid clean sine wave

From these graphs of the filtered data, it is once again possible to take the RMS value of the sine wave and determine the relative magnitudes for each oscillator frequency. This can in turn be converted to magnitude (dB) and used to plot the frequency response curve. This curve is shown in the following figure from which bandwidth and the drop off are calculated. The band width is 6.2 Hz and the slope is -17.4 dB per decade which means it is a first order system, and because of that useful bandwidth may be higher (i.e. the drop off is not so sudden that frequencies just above 4 Hz are lost).

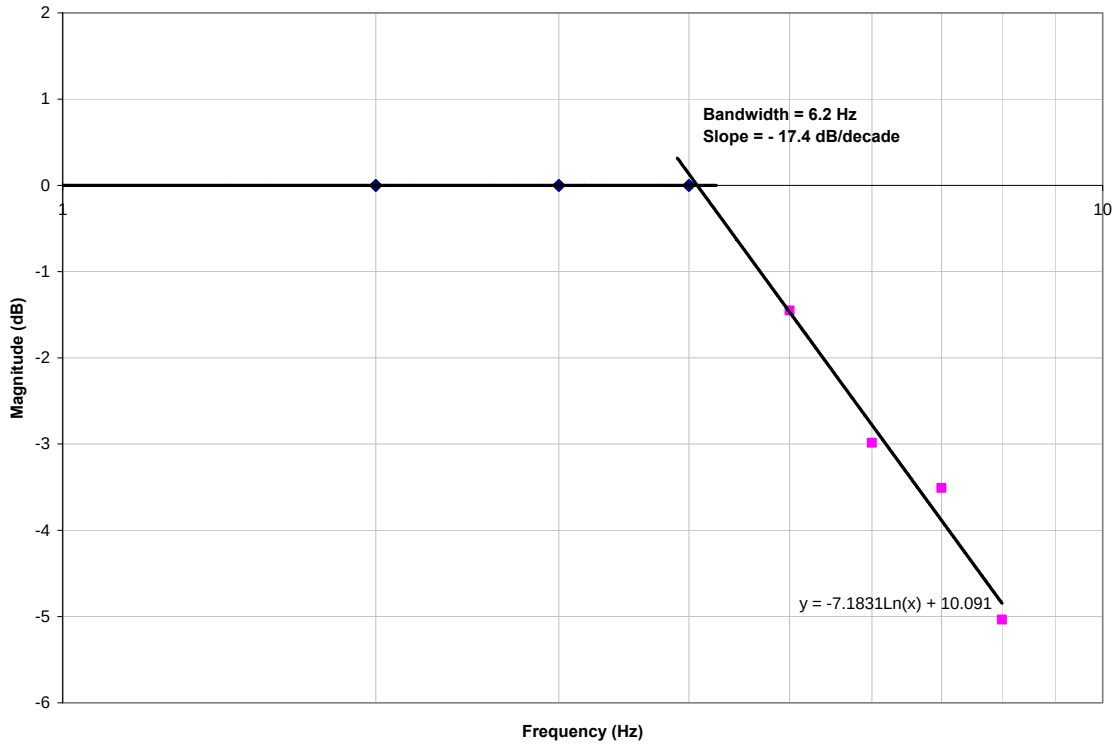

Figure 98: frequency response for cylindrical CTPS #1

4.6 NUMERICAL MODEL COMPARISON AND VALIDATION

As previously described, significant amounts of work were devoted to modeling each type of sensor in hopes of creating reliable engineering tools. The Planar CTPS sensor was not modeled as such, but a variant called the CHFPS was modeled, and it is believed a comparison between that model and the experimental results for the CTPS is a reasonable one. Table seven shows a comparison of modeled characteristics to an average of the experimental data.

	Planar		Cylindrical	
	Bandwidth	Sensitivity	Bandwidth	Sensitivity
Modeled	3 Hz	$2.9x10^{-13}$ #/cm^2*sec	10 Hz	3.5x10-13 #/cm^2*sec
Experimental	3.6 Hz	6.2x10-13 #/cm^2*sec	6.2 Hz	4.5x10-13 #/cm^2*sec

Table 7: Comparison of Modeled and experimental characteristics

Comparison of the modeled to experimental sensitivity of the planar sensor shows a significant difference in favor of the actual sensor. It is likely that a larger quantity of uranium was included on the sensor than was modeled, which would be an easy thing to remedy. The most important comparison is that of bandwidth, with the model[17] predicting a bandwidth of three Hz for a sensor of similar construction as planar sensor #28. This study has shown the CTPS sensor to be capable of 3.6 Hz, but the fact that the model is not perfectly correct is not necessarily bad. That the measured bandwidth is that close to the model indicates the model is not far from reality, and the difference is likely explained by the fact that the model was written for the CHFPS. This indicates that the model is useful for designing and specifying future planar sensor designs once it is rewritten for the CTPS application.

The cylindrical CTPS sensor model was most recently updated in a thesis by Liu, and in the thesis, calculations were made of the bandwidth of a cylindrical sensor very much like the sensor that has been detailed in this work. The modeled sensor was said to have a bandwidth of twenty Hz. Clearly this far better than was found in practice (6.2 Hz), but that model did rely on perfect assembly and thermal contact. In #1 that may not have been the case. This model also reflects better thermal contact between the platinum heater wire and the uranium core which directly impacts the bandwidth by reducing the time necessary for the core power changes to be detected by the control system. The sensitivity predicted by this model is reasonably close to that of the actual sensor, and as with the planar sensor, the quantity of uranium modeled may not be exactly the same as used in the sensor.

5.1 FURTHER TESTING

The results from these tests are encouraging for the future of this technology. There is certainly room for additional work to be performed on this generation of sensors to characterize them fully. The main concern is to get mode two operational and test the sensors with a digital controller utilizing mode two. This would alleviate the problems experienced with the sensor drift and would validate much of the work that has been invested into the digital system. The Labview VI written for mode two would be very expensive to either duplicate or rewrite, but bench testing has shown that all capabilities are functional, except for smooth PID control. The PID VI is a very small component of the overall system, and it is very likely that it can either be debugged or rewritten without a Herculean effort. If the current PID VI is found to be unworkable or too difficult to debug, the system could easily accommodate a simpler proportional control vi such as the DPC, without much additional effort.

Another obvious suggestion is that more sensors be tested in the LVEC facility. Several complete sensors of each type exist and are ready to be tested, and at this time, the capabilities exist to quickly produce many more. The capability of testing two sensors simultaneously exists, and should be used in further testing to streamline the testing process. Additionally, designs utilizing arrays of CTPS devices have been modeled and can be tested in the LVEC facility. It is also very possible to test a planar sensor and cylindrical sensor simultaneously to directly compare response. Until Mode two is fully functional, it is advisable to test with the LVEC heater running to maintain a constant temperature, as has been done here.

5.2 NUMERICAL MODELING

The Models currently written for analysis of the CTPS can be looked at as very useful tools for the continued development of this type detector system. The validation presented in chapter 4 shows that they will require additional investment to more closely follow the experimental results. This is not a large hurdle though, as each of the models is very clearly written and fully commented. Once these models have been modified, the current generation CTPS detector can be refined. As part of the development process,

ideas for modifications to the current design have been prepared. Once the models are modified, it will be possible to examine these designs and possibly refine the CTPS further.

Appendix A

Neutron Transport Studies to Identify Effects of Power Sensors on the Core Neutronic Environment

Vefa Kucukboyaci
Bojan Petrović

Westinghouse Electric Company LLC
Science and Technology Department
1344 Beulah Road
Pittsburgh, PA 15235

Prepared under DOE Grant No. DE-PS03-00SF22016
NERI Project "An In-Core Power Deposition and Fuel Thermal Environment Monitor for Long-lived Reactor Cores"
Task 1d

April 2003

Neutron Transport Studies to Identify Effects of Power Sensors on the Core Neutronic Environment

Introduction

This report summarizes the transport theory calculations that were performed to identify effects of in-core power monitors (sensors) on the core neutronic environment as part of the second year program tasks. IRIS is an Advanced LWR and its fuel assembly has been chosen as a representative Generation IV sensor environment. Monte Carlo models for two prototype sensor designs, cylindrical and planar sensors, have been developed and incorporated into the IRIS fuel assembly model. For the perturbation studies, we have chosen bounding numerical test cases with sensors containing high- (97%) and low- (4.5%) enriched uranium and with small and large axial sizes for the cylindrical sensor design. For these different cases, we have performed Monte Carlo simulations using the MCNP *[1]* code to compute the assembly multiplication factor, thermal and fast fluxes and pin power distributions and thereby to identify effects of the sensors on the core neutronics environment.

Computational Models

Geometry

Figure A1 shows the reference 17x17 IRIS fuel assembly considered for the perturbation studies. A quarter of the assembly, as marked on Figure A1, is modeled by prescribing reflective boundary conditions on the right, left, in, and out boundaries. The model spans 30.48 cm (1ft.) axially with reflective top and bottom surfaces. The sensors are placed inside the instrumentation tube, at axial mid-plane of the model. Reflective boundary conditions essentially render the model into an infinite array of sensors repeated axially at every 30.48 cm.

Figures A2a and A2b show the assembly radial and axial configurations. The close-up depiction of the instrumentation tube shows different layers of material of the cylindrical sensor, for which the circled numbers correspond to different material regions described below. Similarly, Figures A3a and A3b show the fuel assembly with the planar sensor.

Radial dimensions of the cylindrical sensor design (Figure A2b) are assumed to be:

1. UO_2+$KAlSi_3O_8$ Core *R = 3.5E-02 cm*
2. Heater Wire *IR = 3.5E-02 cm, OR = 3.5941317E-02 cm*
3. BeO Conductor *IR = 3.5941317E-02 cm , OR = 7.5E-02 cm*
4. Thermal Insulation *IR = 7.5E-02 cm, OR= 2.75E-01 cm*
5. Outer metal can *IR = 2.75E-01 cm, OR= 3.0E-01 cm*
6. Platinum socket *R = 1.3108600E-01 cm*

Note that the heater wire is assumed to be a solid shell, for which the equivalent *IR* and *OR* are calculated based on the weight and the density of Pt.

Axial dimensions of the cylindrical sensor design are assumed as:

1. UO_2+$KAlSi_3O_8$ Core *H = 1.166852 cm*
2. Heater Wire *H = 1.166852 cm*
3. BeO Conductor *H = 1.139 cm*
4. Thermal Insulation *H = 1.26096 cm*
5. Outer metal can *H = 1.7018 cm*
6. Platinum socket *H = 6.105E-02 cm*

For the planar sensor design (Fig. 3b), we have the following radial dimensions:

1. Alumina substrate *R = 0.6 cm*
2. Alumina Ring *IR = 0.55 cm, OR = 0.6 cm*
3. UO_2+$KAlSi_3O_8$ Core *R = 0.519 cm*
4. Pt heater rings, outermost ring *OR = 0.5 cm, Δt=0.0385 cm* and total of 7 rings
5. Sapphire Cover *R = 0.6 cm*

Note that the radius of the planar sensor has been reduced form its design value of 0.65 cm to 0.6 cm to fit in the IRIS instrumentation tube.

The axial dimensions of the sensor design are assumed as follows:

1. Alumina substrate *H = 0.0508 cm*
2. Alumina Ring *H = 0.1278 cm*
3. UO_2+$KAlSi_3O_8$ core *R = 5.32315E-03 cm*
4. Pt heater rings *H = 1.E-03 cm*
5. Sapphire Cover *H =5.E-02 cm*

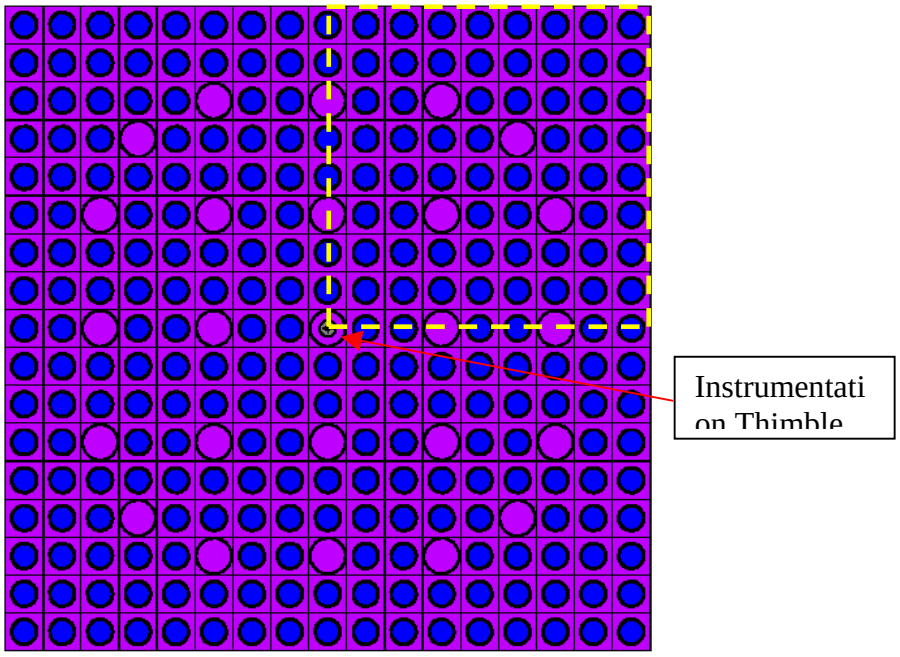

Figure A1. Reference 17x17 IRIS Fuel assembly. Dashed lines represent the Monte Carlo model boundaries.

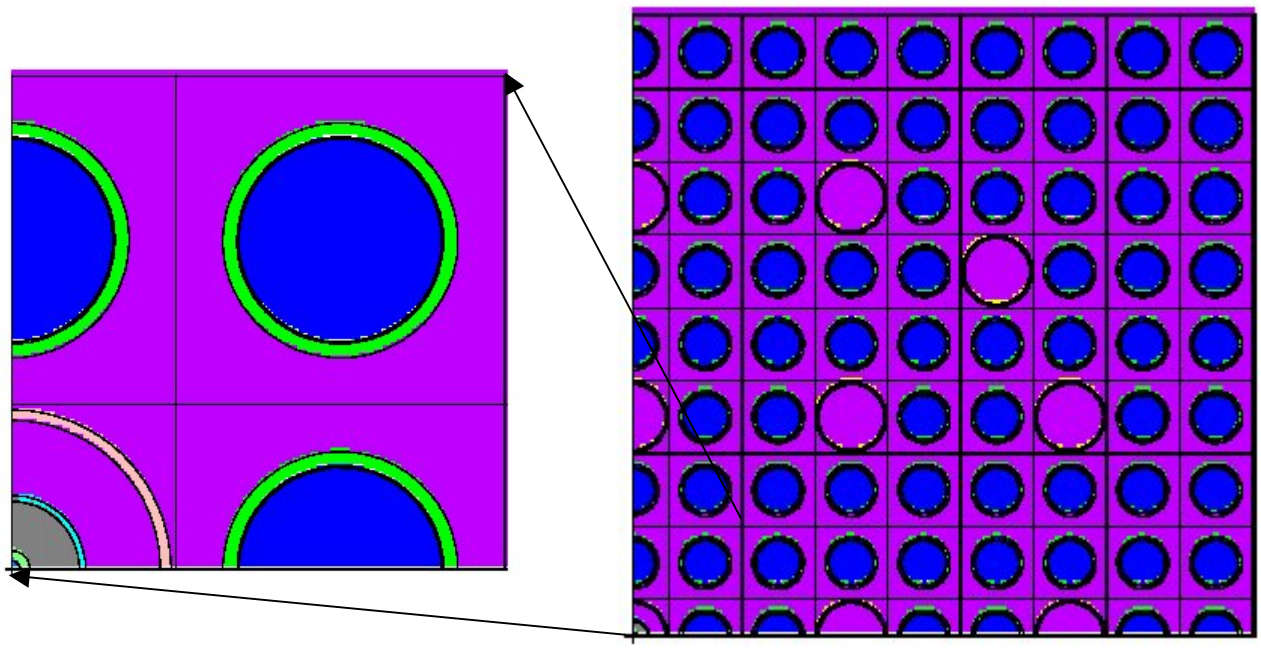

Figure A2a: Radial configuration of the quarter 17x17 IRIS assembly shown with close-up of the instrumentation tube and the cylindrical sensor.

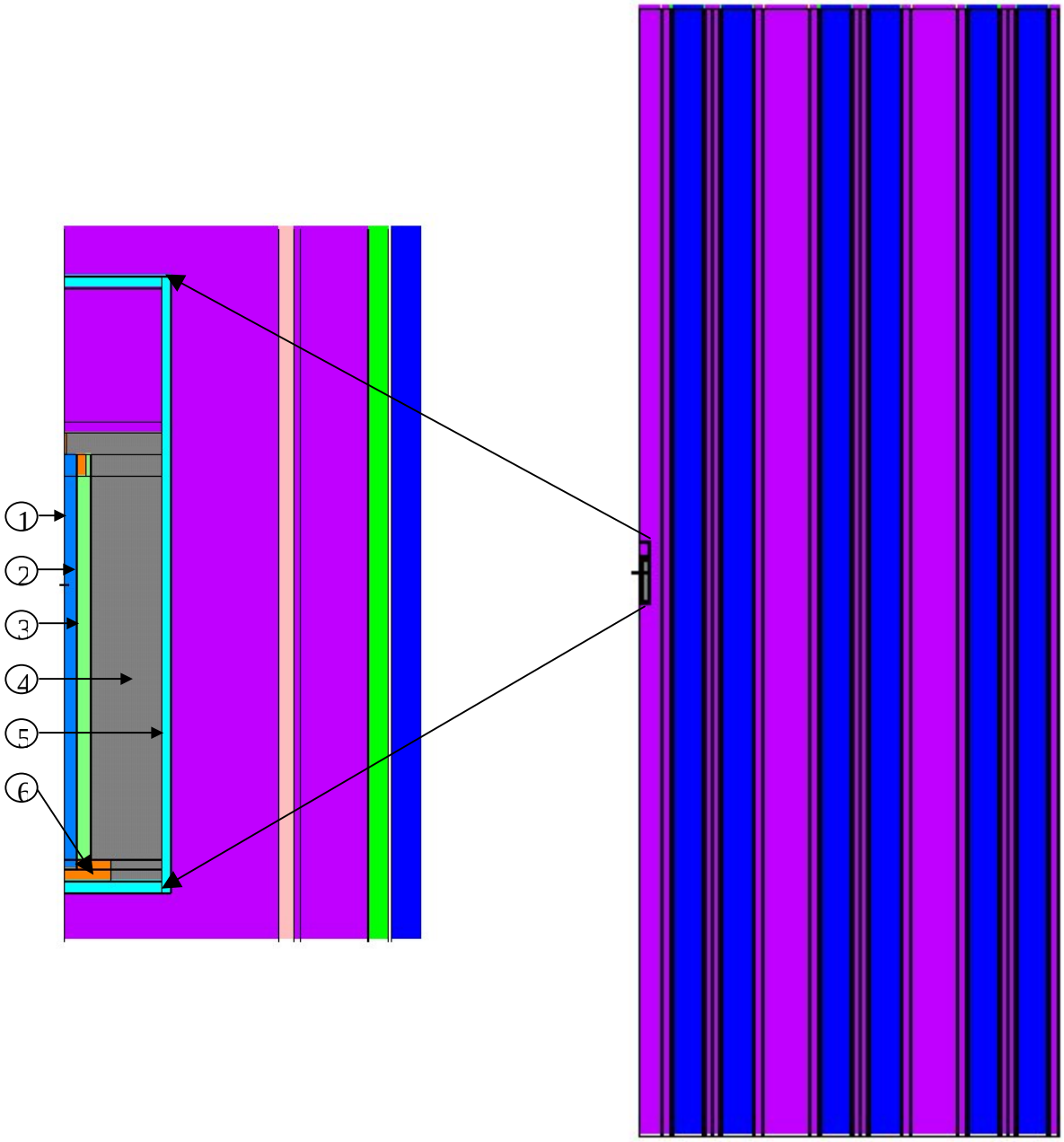

Figure A2b: Axial configuration of the quarter 17x17 IRIS assembly shown with a close-up of the instrumentation tube and the cylindrical sensor.

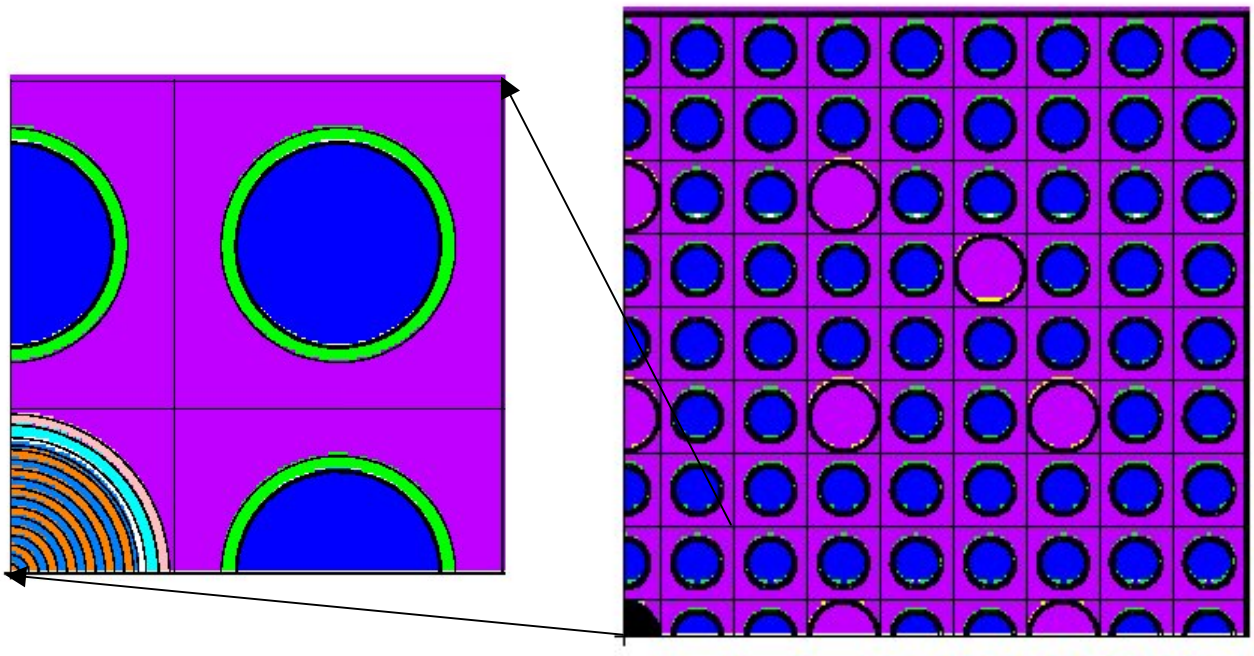

Figure A3a: Radial configuration of the quarter 17x17 IRIS assembly shown with close-up of the instrumentation tube and the planar sensor.

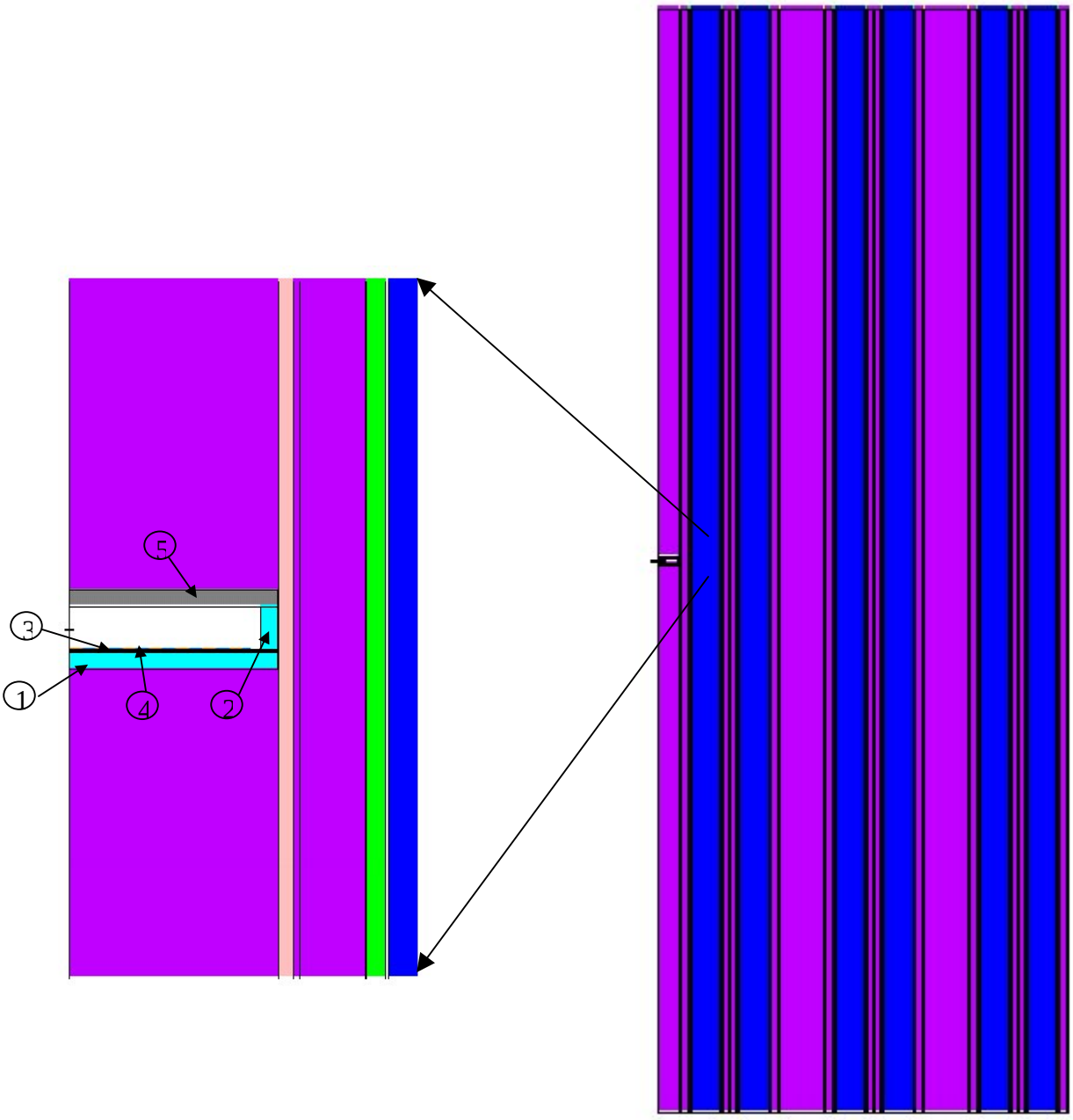

Figure A3b: Axial configuration of the quarter 17x17 IRIS assembly shown with a close-up of the instrumentation tube and the planar sensor.

Materials and Cross Sections

Table A1 summarizes the materials used in the Monte Carlo models.

Table A1: Materials and cross-sections used in MCNP simulations

Material Physical Density (g/cc)	Material Constituents		
	Isotope	Cross-section identifier	Atomic fraction
UO2 + KAlSi3O8 Core ρ=6.88589	U235 U238 O NatK Al NatSi	92235.60c 92238.60c 8016.60c 19000.60c 13027.60c 14000.60c	1.893903E-01 5.642106E-03 6.429656E-01 3.240041E-02 3.240040E-02 9.720122E-02
BeO Conductor ρ = 2.570451E-01	Be O	4009.60c 8016.60c	5.000000E-01 5.000000E-01
Thermal Insulation (Al2O3 Powder) ρ = 1.564	Al O	13027.60c 8016.60c	4.0000E-01 6.0000E-01
Platinum ρ = 21.45	Pt	78000.35c	1.000000E+00
SS-304 Outer Can \ ρ = 7.92	Fe26 NatCr NatNi Mn55	26000.50c 24000.50c 28000.50c 25055.60c	6.882319E-01 2.020870E-01 8.950725E-02 2.017391E-02
Alumina Washer + Seal Glass ρ = 2.97	Al O NatK NatSi	13027.60c 8016.60c 19000.60c 14000.60c	2.7703393E-01 6.0585550E-01 2.927763E-02 8.783289E-02
Alumina Al2O3 ρ = 1.56433 g/cc	Al O	13027.60c 8016.60c	4.00000E-01 6.00000E-01
Sapphire (Al2O3) ρ = 2.97	Al O	13027.60c 8016.60c	4.0000E-01 6.0000E-01

Tallies

Neutron flux is tallied over two energy bins, namely thermal and fast groups, with 0.625 eV being the thermal cutoff energy. Furthermore, pin power is tallied by multiplying the flux tallies by the total fission cross-section and fission Q (MeV/fission). Spatially, tallies are made in each fuel pin and guide/instrumentation thimble to obtain a distribution over the whole fuel assembly.

Monte Carlo Simulations

MCNP time independent criticality simulations were performed for the IRIS assembly with and without sensors. Table A2 shows the cases performed for the perturbation studies. Note that in the long cylindrical sensor case, the U-core region of the sensor is axially stretched to match the axial dimensions of the assembly. With the reflecting top and bottom boundaries, this case essentially simulated a 2-D, axially infinite sensor. In the low-enriched cases, we have used the same enrichment level in the sensor cores as the fuel rods.

Table A2: Cases performed for the perturbation studies

MCNP Model	Sensor Axial Height (cm)	Sensor Outside Radius (cm)	(UO_2+ $KAlSi_3O_8$) Enrichment
No Sensor (Base case)	-	-	-
Cylindrical Sensor	1.733	0.3	97%
Long Cylindrical Sensor	29.07799	0.3	97%
Cylindrical Sensor with Low Enriched U	1.733	0.3	4.95%
Planar Sensor	0.2286	0.6	97%
Planar Sensor with Low Enriched U	0.2286	0.6	4.95%

For each simulation, we initially performed 450 criticality cycles with 10000 neutrons/cycle. We then used the source distribution from this initial simulation to perform 900 cycles with 20000 neutrons/cycle to achieve acceptable statistical uncertainty, which is essential for identifying the perturbations due to the sensors. Each of these simulations required ~18 hr CPU time on an HP-C3600 workstation.

Assembly Multiplication Factor

Figure A4 shows the assembly multiplication factors obtained via Monte Carlo simulations. In Table A3, cases with sensor are compared to the base case without the sensor. Here $\Delta\rho$ is defined as:

$$\Delta\rho = \ln\left(\frac{k_{sensor}}{k_{nosensor}}\right)\cdot 10^5 \quad [pcm]$$

Figure A4 and Table A3 indicate that neither the cylindrical nor the planar sensor has significant impact on the assembly multiplication factor (in all cases change of reactivity is within +/-20 pcm relative to the base case with no sensor). The effect is masked by the small statistical uncertainty. This is an expected result, as the amount of fissile material in the sensor is negligible compared to the total assembly loading.

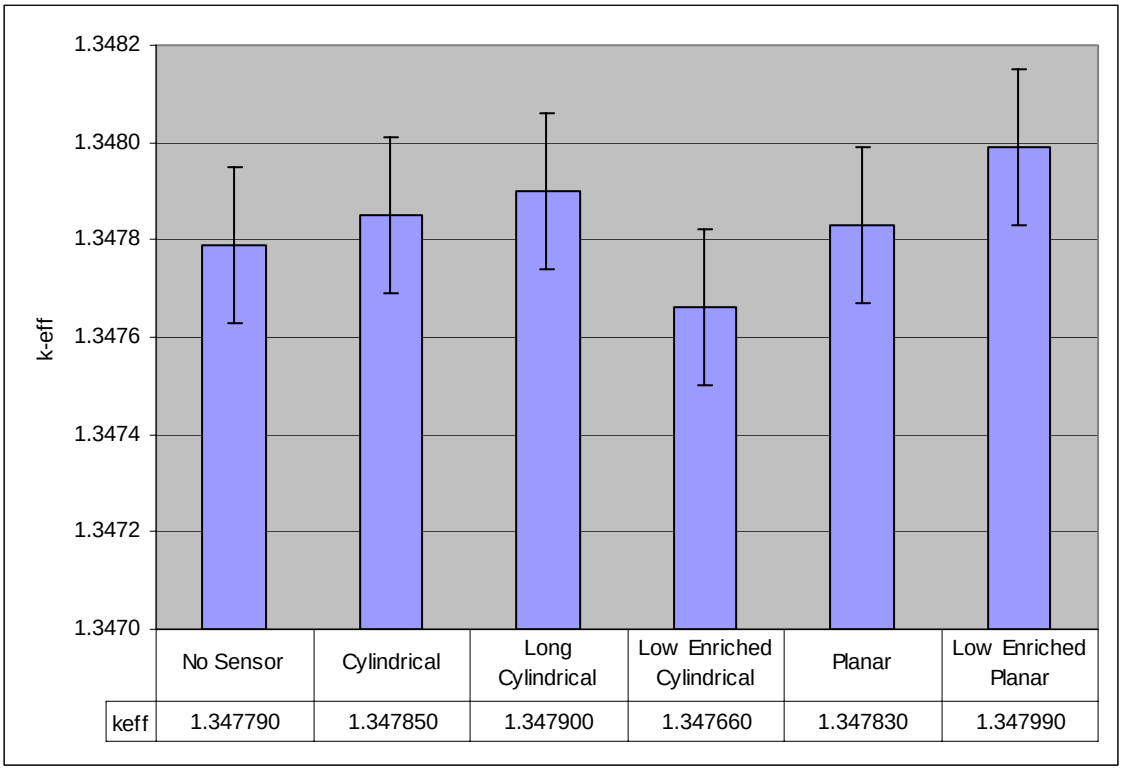

Figure A4: Assembly multiplication factors for different cases.

Table A3: Comparison of assembly multiplication factors

Case	keff	rel. error	Δρ (pcm)	rel.error (pcm)
No Sensor	1.347790	0.000160	-	-
Cylindrical	1.347850	0.000160	4.451633	22.627417
Long Cylindrical	1.347900	0.000160	8.161176	22.627417
Low Enriched Cylindrical	1.347660	0.000160	-9.645885	22.627417
Planar	1.347830	0.000160	2.967777	22.627417
Low Enriched Planar	1.347990	0.000160	14.838006	22.627417

Pin Power/Flux Distributions

Here, we identify the effect of sensors on the assembly pin power and flux distributions. The comparisons are shown on a relative basis, i.e., ratios of cases with sensors to cases without sensors. In Table A4, power and fluxes in the sensor cell are compared to average power and fluxes in the assembly (averaged over the fuel pins). This table shows how the neutronic environment in the sensor is different than in the fuel pins. Due to highly enriched uranium in the sensor core, power density is larger by more than an order of magnitude than in an average fuel pin. When the enrichment level is reduced to 4.95%, about ~11% and ~37% more power is generated in the cylindrical and planar sensors, respectively. This is mainly due to lower self-shielding and larger amount of water near the sensors, hence a higher thermal flux level relative to fuel pins. Fast flux levels in the cylindrical and low enriched cylindrical sensors are similar to no sensor case, while the long cylindrical and the planar designs are exposed to a higher fast flux level. Similar trend is observed for the total fluxes.

Table A4: Ratio of power (or fluxes) in the sensor cell to average fuel pin power (or fluxes). (Numbers in parentheses are associated relative errors)

Model	Power Ratio	Thermal Flux Ratio	Fast Flux Ratio	Total Flux Ratio
No Sensor	NA (NA)	1.37673 (0.0032)	0.96159 (0.0013)	1.01152 (0.0013)
Cylindrical	11.59396 (0.0456)	1.09045 (0.0493)	0.94408 (0.0223)	0.96170 (0.0204)
Long Cylindrical	11.83574 (0.0095)	1.08015 (0.0102)	1.00951 (0.0045)	1.01800 (0.0042)
Low Enriched Cylindrical	1.10838 (0.0460)	1.26183 (0.0476)	0.94245 (0.0222)	0.98087 (0.0202)
Planar	14.32506 (0.0223)	1.29162 (0.0231)	1.03537 (0.0126)	1.06620 (0.0113)
Low Enriched Planar	1.36671 (0.0218)	1.32340 (0.0229)	1.01289 (0.0120)	1.05027 (0.0108)

Tables A5a-b to A7a-b show relative pin power and flux distributions within quarter assembly for different sensor types and the associated relative errors. The instrumentation thimble cell holding the sensor is designated with red color, while all other water cells (guide tubes) are colored yellow. In the long cylindrical sensor case (which may be used as a bounding case), we notice that pin power in the immediate vicinity of the instrumentation thimble is affected by less than 2%, while all other pins have essentially the same power levels as in the no sensor case. For the planar sensor, pin power levels in all cells are essentially same as the no sensor case. Looking at the thermal and fast flux distributions, we observe that presence of a sensor has only a 'local' impact, i.e., only the fluxes in the cell containing the sensor are affected.

Table A5a: Ratio of pin power distribution of 'Long Cylindrical' case to 'No Sensor' case

Power Ratio								
1.00443	1.00223	1.00085	1.00032	1.00151	1.00233	1.00011	1.00360	1.00668
1.00223	0.99801	0.99552	0.99982	1.00231	1.00304	1.00323	1.00146	1.00149
1.00085	0.99552	1.00526	1.00355	1.00182	NA	1.00155	1.00308	NA
1.00032	0.99982	1.00355	NA	1.00309	1.00067	0.99833	0.99919	0.99539
1.00151	1.00231	1.00182	1.00309	1.00370	1.00000	1.00322	0.99911	0.99226
1.00233	1.00304	NA	1.00067	1.00000	NA	0.99847	0.99457	NA
1.00011	1.00323	1.00155	0.99833	1.00322	0.99847	0.99803	0.99332	0.99449
1.00360	1.00146	1.00308	0.99919	0.99911	0.99457	0.99332	0.98948	0.98092
1.00668	1.00149	NA	0.99539	0.99226	NA	0.99449	0.98092	NA

Relative Error								
0.00255	0.00226	0.00226	0.00226	0.00226	0.00226	0.00226	0.00226	0.00311
0.00226	0.00212	0.00212	0.00212	0.00212	0.00212	0.00212	0.00212	0.00297
0.00226	0.00212	0.00212	0.00198	0.00198	NA	0.00198	0.00212	NA
0.00226	0.00212	0.00198	NA	0.00198	0.00198	0.00212	0.00212	0.00290
0.00226	0.00212	0.00198	0.00198	0.00198	0.00198	0.00198	0.00212	0.00283
0.00226	0.00212	NA	0.00198	0.00198	NA	0.00198	0.00212	NA
0.00226	0.00212	0.00198	0.00212	0.00198	0.00198	0.00212	0.00212	0.00297
0.00226	0.00212	0.00212	0.00212	0.00212	0.00212	0.00212	0.00212	0.00297
0.00311	0.00297	NA	0.00290	0.00283	0.00000	0.00297	0.00297	NA

Table A5b: Ratio of pin power distribution of 'Planar' case to 'No Sensor' case

Power Ratio								
1.00294	1.00037	0.99756	0.99973	1.00015	1.00071	0.99916	1.00227	1.00265
1.00037	0.99852	0.99736	0.99876	0.99952	0.99983	1.00281	0.99783	0.99635
0.99756	0.99736	0.99887	1.00112	0.99609	NA	1.00292	0.99918	NA
0.99973	0.99876	1.00112	NA	1.00134	1.00187	0.99962	1.00164	0.99984
1.00015	0.99952	0.99609	1.00134	1.00233	0.99938	1.00170	1.00424	0.99492
1.00071	0.99983	NA	1.00187	0.99938	NA	1.00024	0.99852	NA
0.99916	1.00281	1.00292	0.99962	1.00170	1.00024	1.00132	0.99916	0.99866
1.00227	0.99783	0.99918	1.00164	1.00424	0.99852	0.99916	1.00017	0.99947
1.00265	0.99635	NA	0.99984	0.99492	NA	0.99866	0.99947	NA

Relative Error								
0.00255	0.00226	0.00226	0.00226	0.00226	0.00226	0.00226	0.00226	0.00311
0.00226	0.00212	0.00212	0.00212	0.00212	0.00212	0.00212	0.00212	0.00297
0.00226	0.00212	0.00212	0.00198	0.00198	NA	0.00205	0.00212	NA
0.00226	0.00212	0.00198	NA	0.00198	0.00198	0.00212	0.00212	0.00290
0.00226	0.00212	0.00198	0.00198	0.00198	0.00198	0.00198	0.00212	0.00283
0.00226	0.00212	NA	0.00198	0.00198	NA	0.00198	0.00212	0.00000
0.00226	0.00212	0.00205	0.00212	0.00198	0.00198	0.00212	0.00212	0.00297
0.00226	0.00212	0.00212	0.00212	0.00212	0.00212	0.00212	0.00212	0.00297
0.00311	0.00297	NA	0.00290	0.00283	NA	0.00297	0.00297	NA

Table A6a: Ratio of thermal flux distribution of 'Cylindrical' case to 'No Sensor' case

Thermal flux Ratio								
1.00551	1.00022	0.99719	0.99700	1.00005	1.00231	1.00260	1.00872	1.00978
1.00022	0.99732	0.99597	0.99816	0.99969	1.00197	1.00180	1.00212	1.00110
0.99719	0.99597	1.00026	1.00316	0.99539	0.99954	1.00255	1.00320	1.00341
0.99700	0.99816	1.00316	1.00103	1.00162	0.99929	0.99863	1.00525	0.99845
1.00005	0.99969	0.99539	1.00162	1.00160	1.00235	1.00333	0.99904	0.99292
1.00231	1.00197	0.99954	0.99929	1.00235	0.99815	0.99972	1.00018	0.99947
1.00260	1.00180	1.00255	0.99863	1.00333	0.99972	1.00190	0.99868	1.00244
1.00872	1.00212	1.00320	1.00525	0.99904	1.00018	0.99868	0.99669	0.99571
1.00978	1.00110	1.00341	0.99845	0.99292	0.99947	1.00244	0.99571	0.79254

Relative Error								
0.00283	0.00269	0.00255	0.00255	0.00255	0.00255	0.00255	0.00269	0.00368
0.00269	0.00240	0.00240	0.00240	0.00240	0.00233	0.00240	0.00240	0.00325
0.00255	0.00240	0.00240	0.00226	0.00226	0.00198	0.00226	0.00240	0.00269
0.00255	0.00240	0.00226	0.00198	0.00226	0.00226	0.00226	0.00240	0.00325
0.00255	0.00240	0.00226	0.00226	0.00226	0.00226	0.00226	0.00240	0.00325
0.00255	0.00233	0.00198	0.00226	0.00226	0.00191	0.00226	0.00240	0.00269
0.00255	0.00240	0.00226	0.00226	0.00226	0.00226	0.00226	0.00240	0.00325
0.00269	0.00240	0.00240	0.00240	0.00240	0.00240	0.00240	0.00255	0.00339
0.00368	0.00325	0.00269	0.00325	0.00325	0.00269	0.00325	0.00339	0.04937

Table A6b: Ratio of thermal flux distribution of 'Planar' case to 'No Sensor' case

Thermal flux ratio								
1.00234	1.00063	0.99775	0.99862	0.99960	1.00143	0.99812	1.00579	1.00304
1.00063	0.99871	0.99831	0.99842	0.99801	0.99917	1.00196	0.99802	0.99793
0.99775	0.99831	0.99847	1.00156	0.99511	0.99997	1.00187	1.00053	0.99753
0.99862	0.99842	1.00156	1.00074	1.00230	1.00009	0.99747	1.00213	0.99936
0.99960	0.99801	0.99511	1.00230	1.00361	1.00054	1.00206	1.00331	0.99470
1.00143	0.99917	0.99997	1.00009	1.00054	0.99837	1.00243	0.99885	1.00101
0.99812	1.00196	1.00187	0.99747	1.00206	1.00243	1.00268	0.99951	0.99998
1.00579	0.99802	1.00053	1.00213	1.00331	0.99885	0.99951	1.00089	0.99942
1.00304	0.99793	0.99753	0.99936	0.99470	1.00101	0.99998	0.99942	0.93830

Relative Error								
0.00283	0.00269	0.00255	0.00255	0.00255	0.00255	0.00255	0.00269	0.00368
0.00269	0.00240	0.00240	0.00240	0.00240	0.00240	0.00240	0.00240	0.00325
0.00255	0.00240	0.00240	0.00226	0.00226	0.00198	0.00226	0.00240	0.00269
0.00255	0.00240	0.00226	0.00198	0.00226	0.00226	0.00226	0.00240	0.00325
0.00255	0.00240	0.00226	0.00226	0.00226	0.00226	0.00226	0.00240	0.00325
0.00255	0.00240	0.00198	0.00226	0.00226	0.00184	0.00226	0.00240	0.00269
0.00255	0.00240	0.00226	0.00226	0.00226	0.00226	0.00226	0.00240	0.00325
0.00269	0.00240	0.00240	0.00240	0.00240	0.00240	0.00240	0.00255	0.00339
0.00368	0.00325	0.00269	0.00325	0.00325	0.00269	0.00325	0.00339	0.02316

Table A7a: Ratio of fast flux distribution of 'Low Enriched Cylindrical' case to 'No Sensor' case

Fast Flux Ratio								
0.99920	1.00053	0.99823	0.99878	1.00025	0.99856	1.00104	1.00097	1.00094
1.00053	0.99876	0.99958	1.00098	1.00068	1.00011	1.00010	0.99922	0.99996
0.99823	0.99958	0.99905	0.99955	0.99787	0.99925	0.99936	1.00177	0.99892
0.99878	1.00098	0.99955	0.99952	0.99961	1.00031	1.00042	1.00066	0.99756
1.00025	1.00068	0.99787	0.99961	0.99961	1.00023	1.00094	0.99962	0.99757
0.99856	1.00011	0.99925	1.00031	1.00023	1.00000	1.00159	0.99855	0.99874
1.00104	1.00010	0.99936	1.00042	1.00094	1.00159	0.99990	0.99947	1.00064
1.00097	0.99922	1.00177	1.00066	0.99962	0.99855	0.99947	0.99984	0.99941
1.00094	0.99996	0.99892	0.99756	0.99757	0.99874	1.00064	0.99941	0.97988

Relative Error								
0.00113	0.00113	0.00099	0.00099	0.00099	0.00099	0.00099	0.00113	0.00141
0.00113	0.00099	0.00099	0.00099	0.00099	0.00099	0.00099	0.00099	0.00141
0.00099	0.00099	0.00099	0.00099	0.00099	0.00085	0.00099	0.00099	0.00113
0.00099	0.00099	0.00099	0.00071	0.00099	0.00099	0.00099	0.00099	0.00127
0.00099	0.00099	0.00099	0.00099	0.00099	0.00099	0.00099	0.00099	0.00127
0.00099	0.00099	0.00085	0.00099	0.00099	0.00085	0.00099	0.00099	0.00113
0.00099	0.00099	0.00099	0.00099	0.00099	0.00099	0.00099	0.00099	0.00141
0.00113	0.00099	0.00099	0.00099	0.00099	0.00099	0.00099	0.00099	0.00141
0.00141	0.00141	0.00113	0.00127	0.00127	0.00113	0.00141	0.00141	0.02223

Table A7b: Ratio of fast flux distribution of 'Low Enriched Planar' case to 'No Sensor' case

Fast Flux Ratio								
0.99921	0.99985	0.99971	0.99972	0.99808	0.99773	1.00102	1.00025	1.00141
0.99985	0.99885	0.99913	0.99994	0.99936	1.00008	0.99955	0.99934	0.99779
0.99971	0.99913	0.99930	0.99914	1.00017	0.99929	0.99949	1.00045	0.99778
0.99972	0.99994	0.99914	0.99917	0.99878	1.00072	0.99982	0.99916	0.99711
0.99808	0.99936	1.00017	0.99878	0.99881	0.99869	0.99941	0.99955	0.99795
0.99773	1.00008	0.99929	1.00072	0.99869	1.00032	1.00036	0.99766	0.99854
1.00102	0.99955	0.99949	0.99982	0.99941	1.00036	0.99848	0.99839	0.99930
1.00025	0.99934	1.00045	0.99916	0.99955	0.99766	0.99839	0.99953	1.00154
1.00141	0.99779	0.99778	0.99711	0.99795	0.99854	0.99930	1.00154	1.05268

Relative Error								
0.00113	0.00113	0.00099	0.00099	0.00099	0.00099	0.00099	0.00113	0.00141
0.00113	0.00099	0.00099	0.00099	0.00099	0.00099	0.00099	0.00099	0.00141
0.00099	0.00099	0.00099	0.00099	0.00099	0.00085	0.00099	0.00099	0.00113
0.00099	0.00099	0.00099	0.00071	0.00099	0.00099	0.00099	0.00099	0.00127
0.00099	0.00099	0.00099	0.00099	0.00099	0.00099	0.00099	0.00099	0.00127
0.00099	0.00099	0.00085	0.00099	0.00099	0.00085	0.00099	0.00099	0.00113
0.00099	0.00099	0.00099	0.00099	0.00099	0.00099	0.00099	0.00099	0.00141
0.00113	0.00099	0.00099	0.00099	0.00099	0.00099	0.00099	0.00099	0.00141
0.00141	0.00141	0.00113	0.00127	0.00127	0.00113	0.00141	0.00141	0.01205

Summary and Conclusion

We performed Monte Carlo calculations to identify effects of in-core power monitors (sensors) on the core neutronic environment. As a representative Generation IV reactor environment, we modeled an IRIS fuel assembly and placed the sensors in the instrumentation thimble for perturbation studies. Numerical test cases included cylindrical and planar sensor designs containing high- (97%) and low- (4.5%) enriched U and with small and large axial sizes (cylindrical design only). For these different cases, we computed the assembly multiplication factor, pin power distributions and thermal and fast fluxes. We observed that presence of the sensors did not perturb the assembly multiplication factor and the impact on the power and flux levels was mainly local. However, in the case of using highly enriched uranium sensor design, the power density increase in the sensors was considerable, i.e., more than an order of magnitude larger than the fuel pins. This high power density will affect the performance of the sensors, as they will burn faster than the fuel pins and will require frequent replacements. Therefore, a study of the sensor depletion may be warranted. Moreover, with such a high power density, the thermal performance and integrity of the sensors may become an issue. In summary, the effect of the sensors on the core neutronic environment is acceptable, but the performance of the sensors themselves needs to be further evaluated.

References

[1] J. F. Briesmeister, Ed., "MCNP - A General Monte Carlo N-Particle Transport Code, Version 4C," LA-13709-M (April 2000).